



Technische Universität München

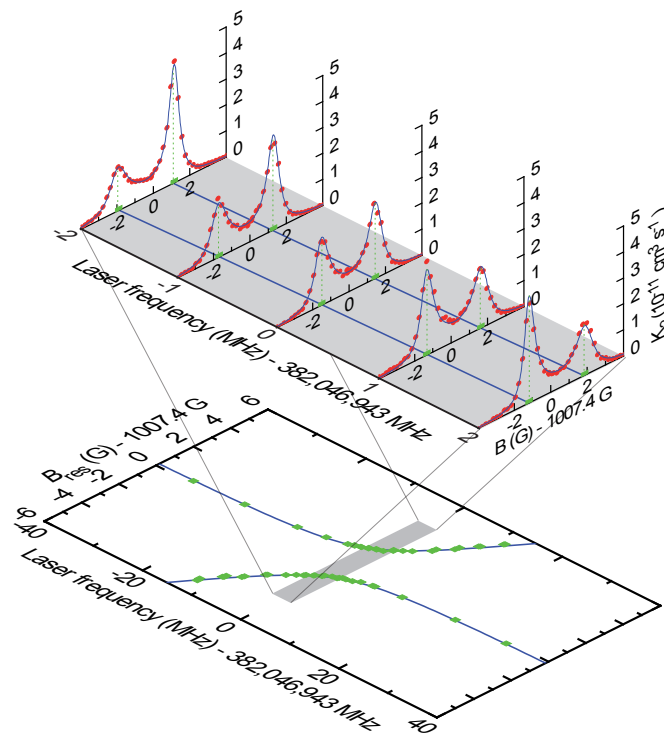


Physik Department



Optical Control of a Magnetic Feshbach Resonance

Dominik M. Bauer



Dissertation

Max-Planck-Institut für Quantenoptik, Garching
and
Physik Department, Technische Universität München

August 2009

Cover illustration: Optical control of a magnetic Feshbach resonance. Upper panel: Autler-Townes splitting of a magnetic Feshbach resonance caused by applying a laser that drives a bound-to-bound transition between the bound state of a Feshbach molecule and an electronically excited bound state. The splitting occurs in the two-body loss coefficient K_2 as a function of the magnetic field B (red circles). Five data sets are shown for different laser detunings in steps of 1 MHz. The magnetic field values B_{res} at which K_2 has its maxima are indicated (green squares). The blue lines are fits of a theoretical model to the experimental data. Lower panel: B_{res} as a function of the laser detuning. The plot shows an avoided level crossing between the two bound states. Details about this measurement are described in Chapter 5.

Technische Universität München
Max-Planck-Institut für Quantenoptik

Optical Control of a Magnetic Feshbach Resonance

Dominik M. Bauer

Vollständiger Abdruck der von der Fakultät für Physik der Technischen Universität München zur Erlangung des akademischen Grades eines

Doktors der Naturwissenschaften (Dr. rer. nat.)

genehmigten Dissertation.

Vorsitzender : Univ.–Prof. Dr. A. J. Buras

Prüfer der Dissertation : 1. Hon.–Prof. Dr. G. Rempe

2. Univ.–Prof. Dr. R. Krücken

Die Dissertation wurde am 27.08.2009 bei der Technischen Universität München eingereicht und durch die Fakultät für Physik am 21.10.2009 angenommen.

Abstract

This thesis reports on experiments on the interaction control in ultracold quantum gases. Starting point for all experiments is a Bose-Einstein condensate of ^{87}Rb atoms. The interaction between the particles is controlled either magnetically using a magnetic Feshbach resonance or optically using a combination of a magnetic Feshbach resonance with a laser induced bound-to-bound transition.

The first part of this thesis discusses experiments, in which the interaction control is used to associate diatomic Feshbach molecules from ultracold atom pairs. One experiment demonstrates the association of molecules inside a three-dimensional optical lattice by ramping the magnetic field adiabatically across a magnetic Feshbach resonance. The system ends up in a state with exactly one molecule at each lattice site. Another experiment induces coherent atom-molecule oscillations in an optical lattice by applying a sudden jump of the magnetic field to a magnetic Feshbach resonance. A third experiment realizes a dissipative analog of the Tonks-Girardeau gas, where bosons behave much like fermions. Here, the bosonic Feshbach molecules are confined in one-dimensional tubes using an optical lattice. Inelastic collisions between the molecules cause strong dissipation that inhibits losses and induces correlations in the molecular gas.

The central part of this thesis explores a novel scheme for controlling the scattering properties of an ultracold atomic gas with laser light. We show theoretically and experimentally that light near-resonant with a molecular bound-to-bound transition can be used to shift the magnetic field at which a magnetic Feshbach resonance occurs. This makes it possible to tune the interaction strength with laser light and at the same time induce considerably less loss than an optical Feshbach resonance would do. To find an appropriate bound-to-bound transition for this scheme, we perform excited-state spectroscopy. When applying laser light resonant with one such bound-to-bound transition we observe an Autler-Townes splitting of the magnetic Feshbach resonance. We find good agreement between the theoretical model and experimental data. Our scheme can be used for a variety of future applications. For example, light patterns created by holographic masks could serve as a tool for changing the scattering length of ultracold atoms on very short time and length scales.

The last part of this thesis reports on experimental progress towards localization of matter waves in a disorder potential. The disorder potential is created using impurity particles with a random spatial distribution. This is realized by particles that are frozen at randomly distributed sites of a deep optical lattice. A second species experiences a much shallower lattice potential, so that the particles are mobile. These particles probe the random distribution of the frozen particles due to the on-site interaction. Theory predicts that the matter waves should localize in this system, but a clear experimental signature of this effect was not found.

Zusammenfassung

Die vorliegende Arbeit berichtet von Experimenten, in denen die Wechselwirkung in ultrakalten Quantengasen kontrolliert wird. Ausgangspunkt hierfür bildet ein Bose-Einstein Kondensat aus ^{87}Rb Atomen. Die Wechselwirkung zwischen den Teilchen wird entweder magnetisch mit Hilfe einer magnetischen Feshbach Resonanz oder optisch mit Hilfe einer Kombination aus magnetischer Feshbach Resonanz und Laser getriebenem Molekül-Molekül-Übergang kontrolliert.

Der erste Teil dieser Arbeit beschreibt Experimente, in denen die Kontrolle über die Wechselwirkung benutzt wird, um zwei-atomige Feshbach-Moleküle aus ultrakalten Atompaaren zu assoziieren. Ein Experiment demonstriert die Assoziation von Molekülen in einem optischen Gitter durch adiabatisches Rampen des Magnetfelds durch eine magnetische Feshbach Resonanz. Das System nimmt dabei einen Zustand mit exakt einem Molekül pro Gitterplatz ein. In einem weiteren Experiment induzieren wir kohärente Atom-Molekül Oszillationen in einem optischen Gitter durch plötzliches Springen des Magnetfelds auf eine magnetische Feshbach Resonanz. Ein drittes Experiment realisiert ein dissipatives Analogon zum Tonks-Girardeau Gas, in welchem sich Bosonen sehr ähnlich zu Fermionen verhalten. Hierbei sind die bosonischen Feshbach-Moleküle entlang eindimensionaler Röhren eines optischen Gitters gesperrt. Inelastische Kollisionen zwischen den Molekülen verursachen starke Dissipation, welche Teilchenverluste unterdrückt und Korrelationen im molekularen Gas erzeugt.

Der zentrale Bestandteil dieser Arbeit stellt die Untersuchung eines neuartigen Schemas zur Kontrolle der Wechselwirkung in einem ultrakalten atomaren Gas mit Laserlicht dar. Wir zeigen mit Hilfe eines theoretischen Modells als auch anhand experimenteller Daten, dass zu einem Molekül-Molekül-Übergang nahresonantes Licht verwendet werden kann, um die Magnetfeldstärke zu verändern, an welchem eine magnetische Feshbach Resonanz auftritt. Dies ermöglicht es, die Wechselwirkungsstärke mit Laserlicht bei wesentlich geringeren Teilchenverlusten durchzustimmen als bei optischen Feshbach Resonanzen. Um einen geeigneten Molekül-Molekül-Übergang zu finden, führen wir Spektroskopie von angeregten Zuständen durch. Durch Anwenden von Laserlicht, welches nahresonant zu einem solchen Molekül-Molekül-Übergang ist, beobachten wir eine Autler-Townes Aufspaltung der magnetischen Feshbach Resonanz. Dabei stimmen das theoretische Modell gut mit den experimentellen Daten überein. Unser Schema kann für eine Vielzahl zukünftiger Experimente eingesetzt werden. Zum Beispiel könnte ein Lichtmuster aus einer holographischen Maske dazu dienen, um die Wechselwirkungseigenschaften von ultrakalten Atomen auf sehr kurzen Zeit- und Längenskalen zu variieren.

Der letzte Teil dieser Arbeit stellt Experimente mit Zielsetzung zur Lokalisierung von Materiewellen in einem Unordnungspotenzial vor. Das Unordnungspotenzial setzt sich aus Verunreinigungen in einer räumlichen Zufallsverteilung zusammen. Diese Verteilung wird durch Teilchen erzeugt, welche auf zufällig verteilten Plätzen eines optischen Gitters festgefroren sind. Eine zweite Spezies nimmt ein wesentlich flacheres Gitterpotential wahr, so dass sich deren Teilchen mobil bewegen. Letztere sondieren durch Wechselwirkung mit den eingefrorenen Teilchen das Zufallspotential. Theoretische Modelle sagen Lokalisierung von Materiewellen der mobilen Teilchen in einem solchen System voraus. Experimentell konnte allerdings kein eindeutiger Hinweis auf diesen Effekt gefunden werden.

List of Publications

Control of a magnetic Feshbach resonance with laser light.

D. M. Bauer, M. Lettner, C. Vo, G. Rempe, and S. Dürr.
Nature Physics **5**, 339–342 (2009).

Combination of a magnetic Feshbach resonance and an optical bound-to-bound transition.

D. M. Bauer, M. Lettner, C. Vo, G. Rempe, and S. Dürr.
Phys. Rev. A **79**, 062713 (2009).
Selected for *Virtual Journal of Atomic Quantum Fluids*, **1**, Issue 1 (2009).

Lieb-Liniger model of a dissipation-induced Tonks-Girardeau gas.

S. Dürr, J.J. García-Ripoll, N. Syassen, D. M. Bauer, M. Lettner, J.I. Cirac, and G. Rempe.
Phys. Rev. A **79**, 023614 (2009).

Dissipation-induced hard-core boson gas in an optical lattice.

J.J. García-Ripoll, S. Dürr, N. Syassen, D. M. Bauer, M. Lettner, G. Rempe, and J.I. Cirac.
New J. Phys. **11**, 013053 (2009).

A dissipative Tonks-Girardeau gas of molecules.

S. Dürr, N. Syassen, D. M. Bauer, M. Lettner, T. Volz, D. Dietze, J.J. García-Ripoll, J.I. Cirac, and G. Rempe.
Proceedings of the XXIth International Conference on Atomic Physics (ICAP 2008), edited by R. Cote, P. L. Gould, M. Rozman, and W. W. Smith,
World Scientific, 307–314 (World Scientific, Singapore, 2009).

Strong dissipation inhibits losses and induces correlations in cold molecular gases.

N. Syassen, D. M. Bauer, M. Lettner, T. Volz, D. Dietze, J.-J. García-Ripoll, J.I. Cirac, G. Rempe, and S. Dürr.
Science **320**, 1329–1331 (2008).

Atom-molecule Rabi oscillations in a Mott insulator.

N. Syassen, D. M. Bauer, M. Lettner, D. Dietze, T. Volz, S. Dürr, and G. Rempe.
Phys. Rev. Lett. **99**, 033201 (2007).

A Mott-like state of molecules.

S. Dürr, T. Volz, N. Syassen, D. M. Bauer, E. Hansis, and G. Rempe.
Proceedings of the XXth International Conference on Atomic Physics (ICAP 2006), edited by C. Roos, H. Häffner, and R. Blatt,
AIP Conf. Proc. No. 869, 278–283 (AIP, New York, 2006).

Preparation of a quantum state with one molecule at each site of an optical lattice.

T. Volz, N. Syassen, D. M. Bauer, E. Hansis, S. Dürr, and G. Rempe.
Nature Phys. **2**, 692–695 (2006).

Contents

Abstract/Zusammenfassung	v
List of Publications	vii
Table of Contents	ix
1. Introduction	1
1.1. Ultracold Quantum Gases	1
1.2. Magnetic and Optical Feshbach Resonances	1
1.3. Ultracold Molecules	3
1.4. Optical Lattices	4
1.5. Localization in Disorder Potentials	4
1.6. This Thesis	5
2. Theoretical Background	7
2.1. Feshbach Resonances and Association of Molecules	7
2.1.1. Collisions between Ultracold Particles	7
2.1.2. Magnetic Feshbach Resonances	7
2.1.3. Optical Feshbach Resonances	9
2.1.4. Molecule Association using a Magnetic Feshbach Resonance	10
2.2. Bosons in an Optical Lattice	11
2.2.1. Bose-Hubbard Model	11
2.2.2. Superfluid-to-Mott-Insulator Phase Transition	12
2.2.3. Inhomogeneous Lattice Potential	13
3. Experimental Setup	15
3.1. Creation of a Bose-Einstein Condensate	15
3.2. Magnetic Field for Feshbach Resonances	17
3.2.1. Temporal Stability	18
3.2.2. Spatial Homogeneity	18
3.3. Optical Dipole Trap	20
3.4. Optical Lattice	23
3.4.1. Periodic Lattice Potentials	23
3.4.2. Experimental Setup	25
3.4.3. Lattice Alignment	26
3.4.4. Imaging	27
4. Ultracold Feshbach Molecules	29

4.1. Preparation of a Quantum State with one Molecule at each Site of an Optical Lattice	29
4.2. Coherent Atom-Molecule Oscillations	32
4.3. Strong Dissipation Induces Correlations in a Cold Molecular Gas	35
5. Optical Control of a Magnetic Feshbach Resonance	39
5.1. General Concept	39
5.2. Combination of a Magnetic Feshbach Resonance and an Optical Bound-to-bound Transition	40
5.2.1. Mean-Field Model	41
5.2.2. Scattering Length	42
5.2.3. Large Detuning	44
5.2.4. Autler-Townes Model	45
5.3. Laser Spectroscopy	47
5.4. Autler-Townes Splitting of a Magnetic Feshbach Resonance	51
5.4.1. Observation of an Autler-Townes Doublet	51
5.4.2. Laser Frequency and Laser Power Dependence	53
5.5. Shifting a Magnetic Feshbach Resonance with Laser Light	54
6. Experimental Progress towards Localization of Matter Waves in a Disorder Potential	61
6.1. A Mobile and a Frozen Species in an Optical Lattice	61
6.1.1. General Concept	61
6.1.2. A Two Species Bose-Hubbard Model	63
6.1.3. An ac-Stark Shift that Depends on the Zeeman State	65
6.1.4. Creation of a Random Spatial Distribution	68
6.2. Experimental Attempt to Localize Matter Waves in a Disorder Potential	69
6.2.1. Experimental Sequence	69
6.2.2. State Preparation	71
6.2.3. Probing the Phase Transition	73
7. Outlook	79
A. ac-Stark Shift for an Alkali Atom in a Magnetic Field	81
A.1. An Atom with Hyperfine Structure in an External Magnetic Field	81
A.2. Zeeman State Dependent ac-Stark Shift	82
Bibliography	85
Danksagung	101

1. Introduction

1.1. Ultracold Quantum Gases

Ultracold gases with temperatures close to absolute zero reveal a plethora of fascinating phenomena in the world of quantum mechanics. Much of this is a consequence of the fact that at very low temperatures the behavior of a gas deviates from Boltzmann's theory of a classical gas. This was first noticed when in 1905 W. Nernst established the third law of thermodynamics because this law implies that at very low temperatures the equations describing a classical gas must break down resulting in a degenerate behavior of the gas.

In 1925, based on S. Bose's work for photons, A. Einstein developed a theory of a degenerate gas and predicted a quantum statistical effect, that is referred to as Bose-Einstein condensation. This effect occurs in a gas of indistinguishable bosons, when the de-Broglie wavelength of the particles is comparable to the interparticle distance. Below a critical temperature, the wave functions of the particles overlap and a macroscopic number of particles occupies the ground state of the system. A macroscopic matter wave forms, a so-called Bose-Einstein condensate (BEC).

In 1995, seventy years after its theoretical prediction, the first BECs were experimentally observed in dilute gases of ^{87}Rb [And95], ^7Li [Bra95], and ^{23}Na [Dav95]. This was the starting point for an enormous progress in the field of ultracold quantum gases, which has been developing rapidly ever since. Today more than a hundred groups worldwide [Dan] perform research on quantum degenerate gases.

However, producing a BEC experimentally is still challenging. Due to the low densities of $\sim 10^{14} \text{ cm}^{-3}$ in the dilute gases, temperatures on the order of 500 nK are required. To reach such low temperatures in the laboratory, the following two step scheme is commonly used. In the first step, laser cooling and trapping techniques are used, where a momentum transfer between the atoms and a radiation field causes a dissipative optical force. This force decelerates the atoms and cools the sample to typical temperatures of $\sim 100 \mu\text{K}$. To reach quantum degeneracy, evaporative cooling is applied in a second step. This technique relies on the selective removal of particles with the highest energy, so that the remaining cloud has a lower mean energy per atom. Elastic collisions between the particles re-thermalize the sample. Typically, experiments reach BECs with around 10^6 atoms. For further details on the general principles of the creation of a BEC and the physics of ultracold quantum gases, the reader is referred to Refs. [Met99, Pet02, Pit03].

1.2. Magnetic and Optical Feshbach Resonances

Interparticle interactions determine many properties of an ultracold quantum gas such as the re-thermalization rate during the evaporative cooling, static and dynamic properties of

the BEC, and correlations between the particles. Therefore, controlling the interparticle interaction opens up a large variety of exciting experiments.

As the particles form a dilute gas, they typically interact by two-body collisions. If during a collision the atom pair state couples to a molecular bound state, then the atom pair can temporarily form a molecule. If the collision energy of the two atoms is degenerate with the energy of the molecular state, the population of the molecular state will be resonantly enhanced. In the vicinity of this resonance the scattering properties drastically change. To obtain control over the interaction properties it is thus desirable to tune the system in and out of resonance.

One option is to apply a static magnetic field to change the collisional properties by addressing a so-called magnetic Feshbach resonance. The impact of a Feshbach resonance on the scattering properties between the particles was first proposed for inelastic scattering leading to loss of particles [Stw76, Tie92]. Later, it was suggested to magnetically tune the elastic scattering properties [Tie93], too. The first experimental observation of a magnetic Feshbach resonance was reported in 1998 [Ino98]. By now, magnetic Feshbach resonances have been found in a variety of atomic species, including mixtures [Chi09]. The occurrence of a magnetic Feshbach resonance was demonstrated both by an enhancement of inelastic collisions leading to particle loss and by the desired change of the elastic part of the scattering length.

Especially the latter capability is of great interest for investigating the reduction or even disappearance of interaction induced effects in ultracold quantum gases as the scattering length is tuned to zero using a magnetic Feshbach resonance. For example, it was experimentally demonstrated that a reduction of the interaction strength leads to the observation of anisotropic dipolar effects in quantum gases [Lah07, Pol09]. In another experiment, the interaction induced dephasing of Bloch oscillations for a BEC in an optical lattice was controlled experimentally [Gus08, Fat08]. Furthermore, a magnetic Feshbach resonance was used for studying the dynamics of a controlled collapse with attractive interaction [Don01].

Alternative techniques for tuning the scattering properties were proposed, replacing the static magnetic field by a radio-frequency field [Moe96], a static electric field [Mar98], or a light field [Fed96, Boh97, Jon06]. The latter method is called an optical Feshbach resonance. Experiments demonstrated the change of the scattering wave function [Fat00] and of the elastic scattering properties [The04]. Unfortunately, optical Feshbach resonances induce rapid loss of particles due to light-induced inelastic collisions. This is the reason why this technique was not used much yet. Alkaline earth atoms offer the possibility to use optical Feshbach resonances on narrow intercombination lines, which results in smaller loss rates [Eno08]. Recently, a scheme was proposed combining the two ideas of a magnetic and a radio-field induced Feshbach resonance for independently controlling two scattering lengths in three-component atomic gases [Zha09]. The radio-frequency dressing of several magnetic Feshbach resonances was demonstrated experimentally [Kau09].

1.3. Ultracold Molecules

In 2000, the Julienne group pointed out that it should be possible to associate stable molecules from ultracold atoms using a magnetic field ramp across a magnetic Feshbach resonance to transfer population from the atomic pair state to the molecular bound state [Mie00]. This idea was adopted in 2003, when ultracold molecules were associated with this method in ${}^6\text{Li}$ [Str03, Cub03, Joc03a, Zwi03], ${}^{23}\text{Na}$ [Xu03], ${}^{40}\text{K}$ [Reg03], ${}^{87}\text{Rb}$ [Dür04a], and ${}^{133}\text{Cs}$ [Her03]. This technique represents a chemical reaction under complete experimental control. The reaction is reversible and no latent heat is released. Therefore, the associated Feshbach molecules are as cold as the atoms in the initial ultracold sample.

Feshbach molecules are typically created in highly excited rovibrational states. Hence, inelastic collisions can lead to rovibrational relaxation and the released binding energy is converted into kinetic energy of the colliding particles. Since the kinetic energy is typically much larger than the trapping potential, the colliding particles are lost. These inelastic collisions limit the lifetime of molecules associated from bosonic atoms. Measurements in bosonic systems, ${}^{23}\text{Na}$, ${}^{87}\text{Rb}$ and ${}^{133}\text{Cs}$, revealed two-body loss-rate coefficients on the order of $10^{-10} \text{ cm}^3/\text{s}$ [Muk04, Chi05, Sya06]. In fermionic systems, like ${}^6\text{Li}$ and ${}^{40}\text{K}$, the loss-rate coefficients far away from the Feshbach resonance are similar, but the loss can be suppressed by orders of magnitude for magnetic fields close to the Feshbach resonance [Cub03, Reg04a]. An explanation based on the Pauli exclusion principle for fermions was put forward [Pet04].

In 2003, the long lifetimes in the fermionic systems were exploited to produce the first molecular BECs [Joc03b, Gre03, Zwi03]. Subsequently, condensation of fermionic pairs on the Fermi-side of the Feshbach resonance was observed [Reg04b, Bar04, Zwi04]. In 2005, the superfluidity of these pairs was proven by the creation of vortices on the Fermi-side of the BEC-BCS crossover [Zwi05].

The short lifetimes of molecules associated from bosonic atoms made experiments comparatively difficult and prevented the creation of molecular BECs in these systems so far. Experiments rather concentrated on the systematic investigation of the association [Mar05, Hod05] and dissociation process [Muk04, Dür04b, Vol05] as well as on one- and two-body decay [Muk04, Tho05a, Chi05, Sya06]. Experiments on coherent molecular optics were performed [AS05], and an alternative method for the production of molecules was shown by applying a radio-frequency field near a Feshbach resonance [Tho05b].

One idea for increasing the lifetime of Feshbach molecules associated from bosons is to de-excite the molecules in a controlled way by transferring them from the highly excited rovibrational state to the internal absolute ground state. Considerable progress towards this goal was reported for a sample of homonuclear ${}^{133}\text{Cs}_2$ molecules to which a Raman transfer was applied [Dan08]. This shows that the creation of a BEC of molecules in their rovibrational ground state seems within reach.

Recently, heteronuclear Feshbach molecules were associated from a Bose-Bose mixture of ${}^{85}\text{Rb}$ and ${}^{87}\text{Rb}$ [Pap06] as well as from a Bose-Fermi mixture of ${}^{40}\text{K}$ and ${}^{87}\text{Rb}$ [Osp06]. Heteronuclear molecules possess a permanent electric dipole moment if transferred to low-lying vibrational levels. This dipole moment gives rise to a dipole-dipole interaction which

is of great interest because of its long-range character. A sample of ^{40}K - ^{87}Rb Feshbach molecules was lately transferred to the rovibrational ground state of the singlet potential using a Raman transfer [Ni08].

1.4. Optical Lattices

Another option to increase the lifetime of bosonic Feshbach molecules is the application of an optical lattice. An optical lattice is a periodic array of microtraps created by the ac-Stark shift of standing light waves. Recently, $^{87}\text{Rb}_2$ Feshbach molecules were associated in an optical lattice. By preparing a quantum state with one molecule at each lattice site, the molecules are isolated from each other and inelastic collisions are suppressed thus leading to considerably longer lifetimes [Tha06, Vol06].

But optical lattices are interesting for more than just this reason. They resemble solid-state systems in condensed matter physics with a real time parameter control and can be used as quantum simulators [Blo05, Blo08]. One vision is, that open problems of solid-state physics like high-temperature superconductivity could be addressed in future experiments using ultracold quantum gases in optical lattices.

By now, several experiments demonstrated the potential of optical lattices to offer an approach to understanding the physics of strongly correlated systems. A prominent example is the realization of a quantum phase transition from a superfluid to a Mott insulator of bosonic atoms by changing the depth of the optical lattice potential [Gre02]. In a Mott insulator the interaction dominates over the kinetic energy of the particles, so that the number of atoms on each lattice site is the same and the particles cannot move.

Strongly correlated systems were also studied in lower dimensions. In 1960, it was shown that bosons with infinitely strong elastic interactions confined to 1D are described by a many-body wave function that closely resembles the one describing identical fermions [Gir60]. This model was generalized to the case of finite repulsive interactions [Lie63]. Such a 1D gas of strongly interacting bosons is called a Tonks-Girardeau gas. The strong repulsion dominates the dynamics and the bosons are forced to behave much like fermions. In 2004, the first experimental realization of such a system was demonstrated using an optical lattice [Par04, Kin04].

1.5. Localization in Disorder Potentials

In an optical lattice, laser light is used to create a spatially periodic potential. This allows for resonant tunneling of particles between lattice sites, because all sites are identical. In contrast, a disorder potential consists of sites with randomly differing properties. Here, tunneling between sites is off-resonant and therefore suppressed. As a result, a wave packet with finite spatial extension can be prevented from dispersing. This is referred to as localization [Ste08]. Originally, localization was discussed for electron transport in condensed matter systems [And58]. However, localization can be generalized to other

physical systems, where wave properties are dominant, because localization is caused by the interference between multiple scattering paths [Tig99].

Localization has been reported experimentally for light waves [Wie97, Sch99, Stö06, Sch07, Lah08], microwaves [Dal91, Cha00], sound waves [Wea90] and for electron gases [Akk07]. However, in these reports localization of matter waves was not observed directly [Bil08]. Recently, disorder potentials were also studied in the field of ultracold quantum gases, both experimentally [Lye05, Clé05, For05, Sch05, Sch06, Fal07] and theoretically [Rot03, Dam03, San04, Kuh05, Gim05, Clé06, Lug07, SP07, Sen07]. These systems offer a high degree of parameter control: the gas can be confined to lower dimensions using optical lattices, the interatomic interaction can be controlled by the density of the ultracold atomic sample or by addressing a Feshbach resonance, and the profile of the sample can be measured by absorption imaging.

First investigations aiming at matter wave localization in the field of ultracold quantum gases used disorder potentials created by the ac-Stark shift of a laser speckle pattern [Lye05, Clé05, For05, Sch05, Sch06] or by a quasi-periodic lattice potential generated from a superposition of standing waves with incommensurate wavelengths [Fal07]. But in these pioneering experiments the observation of localization was precluded either by insufficient randomness of the disorder or by interaction induced screening of the disorder.

In 2008, after optimizing the randomness and reducing the interaction energy of the quantum gas, two groups reported the direct observation of Anderson localization. The Aspect group demonstrated the absence of diffusion of an ultracold sample of weakly interacting ^{87}Rb atoms with very low density inside a disorder potential created by a laser speckle pattern [Bil08]. The Inguscio group presented experimental proof for Anderson localization in a BEC of ^{39}K , that was made non-interacting using a Feshbach resonance. This experiment employed a disorder potential created by superimposing two standing waves with incommensurate wavelengths [Roa08].

1.6. This Thesis

In Chapter 2, this thesis begins with an introduction of the relevant theoretical background for the experiments of this thesis work. We describe the principles of magnetic and optical Feshbach resonances and introduce the Bose-Hubbard model, that describes ultracold bosons in an optical lattice.

Chapter 3 describes the setup, in which the experiments were carried out. This apparatus was built before my thesis work began but it was considerably extended during this thesis work. In particular, a three-dimensional optical lattice was implemented. The homogeneity of the strong magnetic field for addressing magnetic Feshbach resonances was optimized. The optical dipole trap was redesigned and optimized for the reproducible creation of BECs with small density. Moreover, the imaging system was improved.

Chapter 4 briefly summarizes three experiments to which I contributed during my thesis work, and which were already described in detail in previous PhD theses in our group [Vol07, Sya08a]. The first experiment realized a quantum state with exactly one molecule

at each site of a three-dimensional optical lattice [Vol06, Dür06]. We used this state as a starting point for a second experiment, in which we demonstrated the dissipative analog of a Tonks-Girardeau gas induced by inelastic scattering between bosonic Feshbach molecules confined in 1D tubes of an optical lattice [Sya08b, Dür08]. We performed analytical and numerical calculations to gain a deeper understanding of the underlying physics of this experiment [Dür09, GR09]. In a third experiment, we presented coherent oscillations between a molecular state and an atom-pair state [Sya08a].

Chapter 5 reports the central results of this thesis work. It presents our theoretical and experimental achievements concerning the optical control of a magnetic Feshbach resonance [Bau09b, Bau09a]. We show, that the combination of a magnetic Feshbach resonance and an optical bound-to-bound transition makes it possible to change the elastic part of the atomic scattering length with laser light. As the light intensity can vary on a length scale of one optical wavelength and the pattern can also be varied rapidly in time, this technique offers high flexibility. Optical Feshbach resonances also offer this possibility in principle, but our scheme induces considerably less particle loss than an optical Feshbach resonance would do. We present spectroscopic data for various eligible bound-to-bound transitions. Moreover, we demonstrate an Autler-Townes splitting of the magnetic Feshbach resonance for laser light near resonant with a bound-to-bound transition. The experimental results are in good agreement with our theoretical model.

In Chapter 6 we discuss our experimental progress towards localization of matter waves in a disorder potential. We generate a disorder potential using impurity particles in a random spatial distribution [Gav05, Par05, Mas06]. Mobile particles of a second species scatter off these impurities and experience a spatial disorder potential. We discuss a theoretical model for this system [Ros07, Hor07], which predicts that the matter wave describing mobile particles should localize. We made considerable experimental progress towards this goal, but our experiment did not produce a clear proof of localization.

This thesis ends with an Outlook in Chapter 7.

2. Theoretical Background

In this chapter we introduce the theoretical background of this thesis work. Sec. 2.1 covers the principle of Feshbach resonances with magnetic and optical tunability. This section also encompasses the application of Feshbach resonances in the association of molecules from ultracold atoms. In Sec. 2.2 we introduce the theoretical description of ultracold bosons in an optical lattice. For more theoretical details on the topics of this chapter, we refer the reader to Refs. [Tay72, Joa75, Pet02, Pit03, Chi09, Jak98].

2.1. Feshbach Resonances and Association of Molecules

2.1.1. Collisions between Ultracold Particles

In dilute gases, like a BEC, the scattering of particles can be reduced to the problem of two-body collisions, since the average interatomic separation is much larger than the typical range of the interaction potential. If the particles are ultracold, the scattering process can be fully described by one parameter, namely the s-wave scattering length a [Tay72, Sch98]. Elastic and inelastic scattering are described by the real and imaginary parts of a , respectively.

In a many-body system like a BEC, elastic collisions between the particles lead to a shift of the energy eigenvalues. This shift is commonly described in a mean-field approximation that yields the Gross-Pitaevskii equation [Pet02, Pit03]

$$\left(-\frac{\hbar^2 \nabla^2}{2m} + V_{\text{trap}}(\vec{x}) + \frac{4\pi \hbar^2 \text{Re}(a)}{m} |\psi(\vec{x}, t)|^2 \right) \psi(\vec{x}, t) = i\hbar \frac{d}{dt} \psi(\vec{x}, t). \quad (2.1)$$

Here, m is the mass of one boson, V_{trap} the trapping potential for the particles, and $\psi(\vec{x}, t)$ the condensate wave function. The non-linear term proportional to the spatial density of atoms, $n(\vec{x}) = |\psi(\vec{x})|^2$, represents the interatomic interactions. It is proportional to $\text{Re}(a)$. For $\text{Re}(a) > 0$ ($\text{Re}(a) < 0$) the mean-field interaction is effectively repulsive (attractive).

2.1.2. Magnetic Feshbach Resonances

The interatomic interactions have a substantial impact on many properties of a BEC. For many applications, it is therefore desirable to adjust the interaction strength. This is possible with a Feshbach resonance [Fes93, Chi09], that is a scattering resonance in which two channels are resonantly coupled to each other.

This coupling can result either from an appropriate term in the molecular Hamiltonian or from an externally applied light field. The first case is called magnetic Feshbach

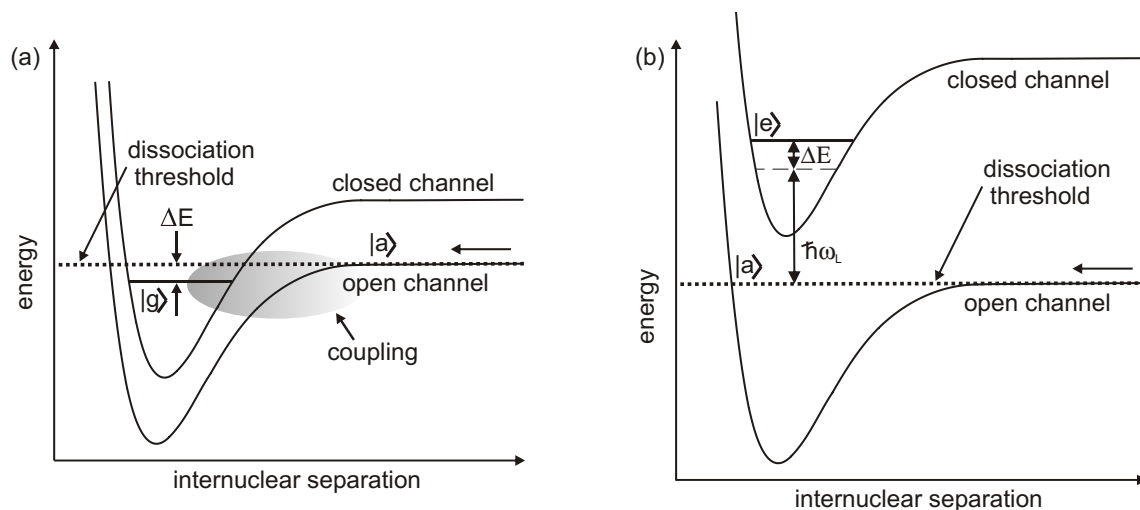


Figure 2.1.: Theory of Feshbach resonances. (a) Magnetic Feshbach resonance. Atoms entering in the open channel $|a\rangle$ can populate a bound state $|g\rangle$ in the closed channel at small internuclear distances due to an inter-channel coupling. The energy difference between the open-channel threshold and the bound state, ΔE , can be controlled by an external magnetic field. For $\Delta E \sim 0$, the population in the bound state is resonantly enhanced. (b) Optical Feshbach resonance. The closed channel is an electronically excited potential which supports a bound state $|e\rangle$. This state can be populated using a light field with angular frequency ω_L , that is detuned from the $|a\rangle$ -to- $|e\rangle$ transition by a small energy ΔE .

resonance because one uses a magnetic field to tune the system into and out of resonance. The second case is called optical Feshbach resonance or photoassociation resonance and will be discussed in Sec. 2.1.3.

Fig. 2.1(a) shows the basic mechanism underlying a magnetic Feshbach resonance. Two atoms enter the collision in the open channel with a kinetic energy, that is very close to the dissociation threshold of this channel. The closed channel represents a different molecular potential and supports a bound state $|g\rangle$ with an energy that differs by only a small amount ΔE from the dissociation threshold of the open channel. During the scattering process, the bound state can be temporarily populated if the molecular Hamiltonian provides a coupling between the two channels. Such a coupling typically arises from the Coulomb exchange interaction, the magnetic dipole-dipole interaction of the valence electrons, or the second-order spin-orbit coupling [Sto88, Mie96].

For the magnetic Feshbach resonance, ΔE can be tuned by applying a magnetic field B because the open and the closed channels have different spin configurations. In the vicinity of the Feshbach resonance, the magnetic field dependence of ΔE can be approximated as linear

$$\Delta E \simeq \Delta\mu(B - B_{\text{res}}). \quad (2.2)$$

Here, the expansion coefficient $\Delta\mu$ represents a magnetic moment and B_{res} denotes the value of B where $\Delta E = 0$. At this magnetic field, the population of the bound state is

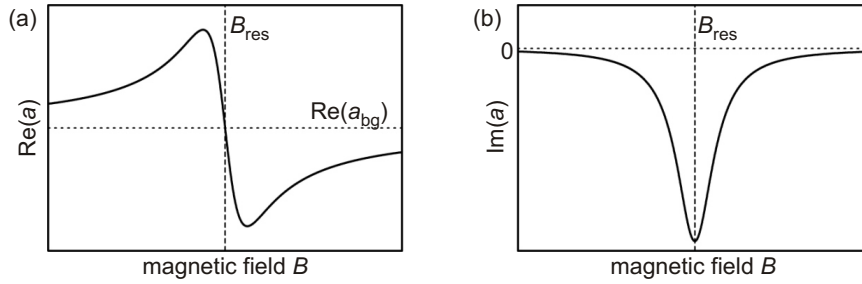


Figure 2.2.: Magnetic Feshbach resonance. (a) The real part of the scattering length $\text{Re}(a)$ shows a dispersive behavior close to the Feshbach resonance B_{res} . a_{bg} is the value of the scattering length far away from B_{res} . (b) The imaginary part of the scattering length $\text{Im}(a)$ is described by a Lorentzian centered at B_{res} .

resonantly enhanced and this is where the magnetic Feshbach resonance occurs.

The resonantly enhanced population of the bound state results in a drastic change of the scattering length a . In the vicinity of the Feshbach resonance, $a(B)$ is well approximated by a Breit-Wigner form [Moe95, Tim99, vA99a, G3r04]

$$a(B) = a_{\text{bg}} \left(1 - \frac{\Delta B}{B - B_{\text{res}} + i \frac{\hbar\Gamma}{2\Delta\mu}} \right). \quad (2.3)$$

Far away from the Feshbach resonance the scattering length a approaches its background value a_{bg} . ΔB is the width of the Feshbach resonance. Γ describes the decay rate of the population in the bound state. Typically, all parameters on the right-hand side of Eq. (2.3) are real.

$\text{Re}(a)$ has a dispersive behavior as a function of B , as shown in Fig. 2.2(a). $\text{Im}(a)$ is a Lorentzian centered at $B = B_{\text{res}}$ with a full width at half maximum (FWHM) of $\hbar\Gamma/\Delta\mu$, see Fig. 2.2(b). Inelastic two-body collisions are thus strongest on resonance. In the special case $\Gamma = 0$, we find that $\text{Im}(a)$ vanishes, and that $\text{Re}(a)$ has a pole at $B = B_{\text{res}}$.

2.1.3. Optical Feshbach Resonances

An alternative technique for tuning a is an optical Feshbach resonance [Fed96, Boh97, The04, Tha05]. The principle of an optical Feshbach resonance is shown in Fig. 2.1(b) and largely resembles that of a magnetic Feshbach resonance. The only differences are the following: The closed channel is an electronically excited potential which supports a dimer state $|e\rangle$ that is coupled to $|a\rangle$ of the incoming particles by applying a light field. Thus ΔE can be controlled with the angular frequency ω_L of the light field.

The behavior of $\text{Re}(a)$ and $\text{Im}(a)$ for an optical Feshbach resonance is analog to that of a magnetic Feshbach resonance, see Fig. 2.2, except that now, for tuning a , the laser frequency ω_L substitutes the role of the magnetic field B .

The excited state $|e\rangle$ can decay with the rate Γ . The disadvantage of optical Feshbach resonances is that typically Γ is fairly large, whereas for magnetic Feshbach resonances Γ

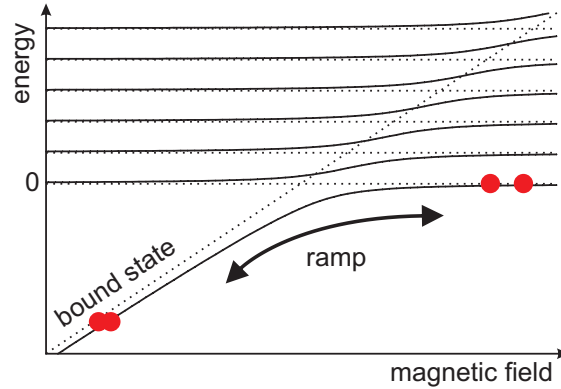


Figure 2.3.: Physical concept of molecule association and dissociation. The solid (dashed) lines represent the energy eigenstate of two atoms in a harmonic trap as a function of the magnetic field in the presence (absence) of coupling between the open and the closed channels. An adiabatic decrease in the magnetic field across the Feshbach resonance transfers population from the atomic-pair state to the bound dimer state. As this ramp is adiabatic, this chemical reaction is reversible.

can be small or even zero. Hence, optical Feshbach resonances typically lead to rapid loss of particles.

2.1.4. Molecule Association using a Magnetic Feshbach Resonance

Besides offering experimental control over a , magnetic Feshbach resonances have proven to be an efficient tool for the association of molecules from ultracold atoms [Köh06]. Several of the publications reported in the present thesis rely on molecule association and subsequent dissociation using a magnetic Feshbach resonance. In the following, we sketch the physical concept underlying this molecule association [Chi09].

Consider two atoms in a confining trap. Here the continuum of atom-pair states above the dissociation threshold of the entrance channel is replaced by a ladder of discrete vibrational energy levels, as illustrated in Fig. 2.3. The zero of the energy scale is chosen to coincide with the energy of the motional ground state of the entrance channel. Therefore, the free atom pair state is flat as a function of the magnetic field. The slope of the molecular state is positive ($\Delta\mu > 0$). The solid (dashed) lines represent energy eigenstates in the presence (absence) of a magnetic Feshbach coupling. The coupling leads to a series of avoided crossings between the bound dimer state and the open-channel trap states. If the coupling strength is small compared to the energy spacing of the trap states and if the magnetic field is close to B_{res} , the crossing between the lowest trap state and the bound dimer states can be described as a two-level system.

In order to create molecules, an atom pair is prepared on the high-field side of the magnetic Feshbach resonance ($B \gg B_{\text{res}}$) in the lowest trap state. Now, the magnetic field is decreased adiabatically across resonance to follow the avoided crossing and transfer the unbound atom pair into a bound molecule, as indicated by the arrow in Fig. 2.3. As

this process is adiabatic, it is reversible. That means by reversing the magnetic field back to a high value far away from the resonance the molecule is dissociated back into a free atom pair. Note, that this ramping scheme for association and dissociation is also applicable in free space.

2.2. Bosons in an Optical Lattice

Optical lattices are periodic, conservative potentials created by far-detuned standing wave light fields. They are commonly used to confine atoms or molecules in geometric configurations of reduced dimensionality [Blo08] and offer the possibility to perform quantum simulations of certain Hamiltonians, for example from solid state physics. A prominent example is the Bose-Hubbard Hamiltonian, that describes the physics of a bosonic many-particle system in an optical lattice [Jak98]. A great strength of optical lattices lies in the realtime control over system parameters like the lattice depth and the inter-particle interaction strength. With this high degree of control one can force the many-body system in the lattice to undergo the quantum phase transition between a superfluid and a Mott insulator [Gre02].

In Sec. 2.2.1 we briefly review the Bose-Hubbard model. A discussion of the quantum phase transition between a superfluid and a Mott insulator is given in Sec. 2.2.2. Finally, we dedicate Sec. 2.2.3 to the inhomogeneous Mott insulator.

2.2.1. Bose-Hubbard Model

Consider the simplest three-dimensional (3D) configuration for an optical lattice, namely the simple cubic lattice. It is created by three intersecting, mutually orthogonal laser beams in standing wave configuration. For details about the experimental realization of such an optical lattice see Sec. 3.4. The 3D potential can be replaced by the following pseudo-potential [Gre03]

$$V_{3D}(\vec{r}) \simeq \sum_j \left(-V_{lat,j} \cdot \cos^2(k_{lat,j} x_j) + \frac{m}{2} \omega_j^2 x_j^2 \right). \quad (2.4)$$

Here, $V_{lat,j}$ is the lattice depth along x_j and k_{lat} the wave-vector of the lattice light. m is the mass of one particle. The last term represents an additional external harmonic confinement with angular trap frequency ω_j . This term summarizes the contributions from the finite diameters of the lattice beams and a magnetic trap or an optical dipole trap.

For a single boson in potential Eq. (2.4) one finds great similarity to the behavior of electrons in solid-state crystals: Due to the periodic nature of the lattice potential the motion of the particle is governed by the energy eigenstates of a band structure. If the energies involved in the dynamics of the system are much smaller than the band gap between the two lowest bands, only the lowest band has to be considered. In this case,

the many-body system of all bosons is described by the following bosonic field operator in second quantization

$$\hat{\Psi}_a(\vec{x}) = \sum_i w(\vec{x} - \vec{x}_i) \hat{a}_i, \quad (2.5)$$

which is expanded in the basis of tight-binding Wannier functions $w(x_i)$. \hat{a}_i annihilates an atom at the lattice site i , that is located at \vec{x}_i .

For a deep lattice, insertion of the ansatz (2.5) into Eq. (2.4) together with a mean-field interaction term of Eq. (2.1) yields the Bose-Hubbard Hamiltonian [Jak98]

$$\hat{H} = -J \sum_{\langle i,j \rangle} \hat{a}_i^\dagger \hat{a}_j + \frac{\text{Re}(U)}{2} \sum_i \hat{n}_i (\hat{n}_i - 1) + \sum_i (\epsilon_i - \mu) \hat{n}_i. \quad (2.6)$$

The first term describes tunneling of bosons between nearest neighboring sites. $\langle i, j \rangle$ denotes the sum over nearest neighboring sites. This term determines the kinetic energy of the particles. J is the tunneling amplitude between adjacent sites i and j , and can be calculated from

$$J = - \int d^3r w^*(\vec{x} - \vec{x}_i) \left(-\frac{\hbar^2}{2m} \nabla^2 + V_{lat}(\vec{x}) \right) w(\vec{x} - \vec{x}_j). \quad (2.7)$$

The second term in Eq. (2.6) describes the on-site interaction between the atoms. $\hat{n}_i = \hat{a}_i^\dagger \hat{a}_i$ is the particle number operator for the lattice site i . The interaction energy is calculated from

$$U = \frac{4\pi\hbar^2 a}{m} \int d^3r |w(\vec{x})|^4. \quad (2.8)$$

The third term in Eq. (2.6) yields an energy offset ϵ_i at site i arising from the external confinement in Eq. (2.4). μ is the chemical potential.

Note that both J and U are functions of the lattice depth V_{lat} in Eq. (2.4) as the Wannier functions adapt to the lattice potential. The lattice depth is commonly quoted in units of the recoil energy $E_{rec} = \hbar^2 k_{lat}^2 / 2m$.

2.2.2. Superfluid-to-Mott-Insulator Phase Transition

Consider the homogeneous case of Eq. (2.6), where ϵ_i is independent of i . By resetting the zero point of the energy, one can set $\epsilon_i = 0$ for all lattice sites i . Then the tunneling term and the interaction term compete with each other and the ground state of the Bose-Hubbard Hamiltonian depends on the ratio U/J . In the limit $U/J \ll 1$, the tunneling term dominates. It is favorable for the particles to be delocalized among all the lattice sites in order to lower their kinetic energy. The many-particle ground state is a superfluid state

$$|\Psi_{SF}\rangle \propto \left(\sum_{i=1}^M \hat{a}_i^\dagger \right)^N |0\rangle, \quad (2.9)$$

where N is the number of particles, M is the number of lattice sites, and $|0\rangle$ is the vacuum state. All particles occupy the same wave function and the total wave function is the product of N identical single-particle wave functions. Eq. (2.9) is not an eigenstate of the number operators \hat{n}_i . Therefore, a measurement of the particle number for each lattice site would reveal shot-noise fluctuations.

In the other limit, where $U/J \gg 1$, the interaction term dominates and the on-site interaction between particles forces the fluctuations of the atom number to be small. The particles tend to be localized at a single site. In this regime, the ground state is a Mott insulator state

$$|\Psi_{\text{MI}}\rangle \propto \prod_{i=1}^M (\hat{a}_i^\dagger)^n |0\rangle, \quad (2.10)$$

where each site is occupied by $n = N/M$ atoms¹. The well-defined particle number results in a maximum uncertainty in the condensate phase.

The superfluid and the Mott insulating regime are connected by a quantum phase transition. The phase transition is theoretically predicted to occur at $U/J \approx 35$ for a simple cubic lattice [Jak98]. This value corresponds to $V_{\text{lat}}/E_{\text{rec}} \approx 12$.

2.2.3. Inhomogeneous Lattice Potential

In Sec. 2.2.2 we considered the case, where ϵ_i is constant for all lattice sites i . However, in the experiment, there is usually a harmonic confinement in addition to the lattice potential, see the last term in Eq. (2.4). For a deep lattice ($J \rightarrow 0$), the confinement leads to a position-dependent atom distribution. In 3D, shells of Mott insulating regions with constant filling factor n form. For given U , μ , and ϵ_i , steps in the lattice filling occur at radial distances where

$$\epsilon_i n_i + U n_i (n_i - 1) = \mu n_i \quad (2.11)$$

for some integer n_i . The result is an inhomogeneous Mott insulator structure, which is shown in Fig. 2.4. Each site is occupied with particles up to the constant chemical potential μ . For increasing ϵ_i the number of atoms per site decreases.

For some experiments performed within this thesis (Sec. 4 and Sec. 6) it is favorable to maximize the Mott insulator region with filling factor $n = 2$. An atom pair on one of these doubly-occupied lattice sites can then be associated to a single molecule that is isolated from other particles. It can be shown theoretically [Han06], that the maximum fraction of $n = 2$ sites is $\sim 53\%$ forming a core surrounded by a shell of singly-occupied sites.

¹For the ground state Eq. (2.10) to exist, $n = N/M$ has to be an integer.

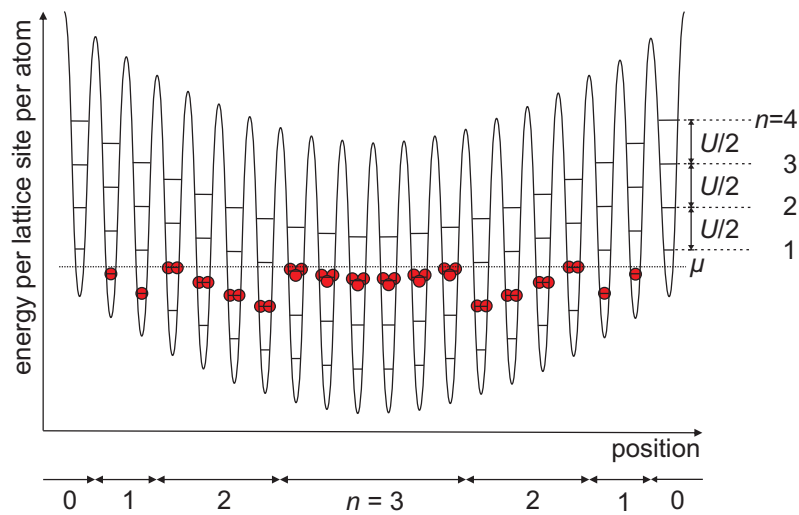


Figure 2.4.: Inhomogeneous Mott insulator for a deep lattice ($J \rightarrow 0$ and $T = 0$). The external confinement gives rise to a position dependent energy offset. Thus, the atoms fill the lattice up to the position-independent chemical potential leading to an onion-shell structure in 3D.

3. Experimental Setup

This section describes the experimental setup used in this thesis. The first components were assembled in 1995 and the apparatus has been growing steadily ever since. A thorough description of all the components presently in use could easily fill 100 pages. We refrain from such a description, especially because much of this can be found in several previous theses of our group Refs. [Sch02, Mar03, Vol05, Sya08a]. Instead, this section puts a strong emphasis on novel components and techniques that were implemented during this thesis work.

The experimental production of a BEC is a highly complex task, in which a variety of cooling techniques like Doppler cooling, polarization gradient cooling, and evaporative cooling need to be mastered. This experimental procedure has been described in great detail in previous theses of our group. In Sec. 3.1, we sketch the experimental route to BEC only briefly. A thorough treatment of the theoretical aspects of BEC can be found in textbooks, e.g. in Ref. [Pet02, Pit03]. A general description of cooling techniques like Doppler- and polarization gradient cooling is given e.g. in Ref. [Met99].

In many of our experiments we control the interaction properties of the particles using magnetic Feshbach resonances which are addressed with strong magnetic fields. The homogeneity of these fields had to be improved during this thesis work, which is described in Sec. 3.2.

The Feshbach resonances used in this thesis require the atoms to be in spin states that cannot be held in a magnetic trap. Hence, we transfer the BEC into an optical dipole trap. The basic physical concepts of dipole traps and the technical realization of such a trap can be found in Sec. 3.3.

Finally, Sec. 3.4 is devoted to a 3D optical lattice, the implementation of which was a major part of this thesis work and opened up the possibility to perform a new class of experiments with our apparatus.

3.1. Creation of a Bose-Einstein Condensate

Bose-Einstein condensation is a phenomenon that occurs if the phase-space density of indistinguishable bosons exceeds a critical value [Pet02, Pit03]

$$n\lambda_{dB}^3 \gtrsim 2.612, \quad (3.1)$$

where n is the spatial density, $\lambda_{dB} = h/\sqrt{2\pi mk_B T}$ the thermal de-Broglie wavelength, m the mass of one boson, and T the temperature. Our experiments start from a vapor of ^{87}Rb atoms at room temperature. From here, 19 orders of magnitude in phase-space

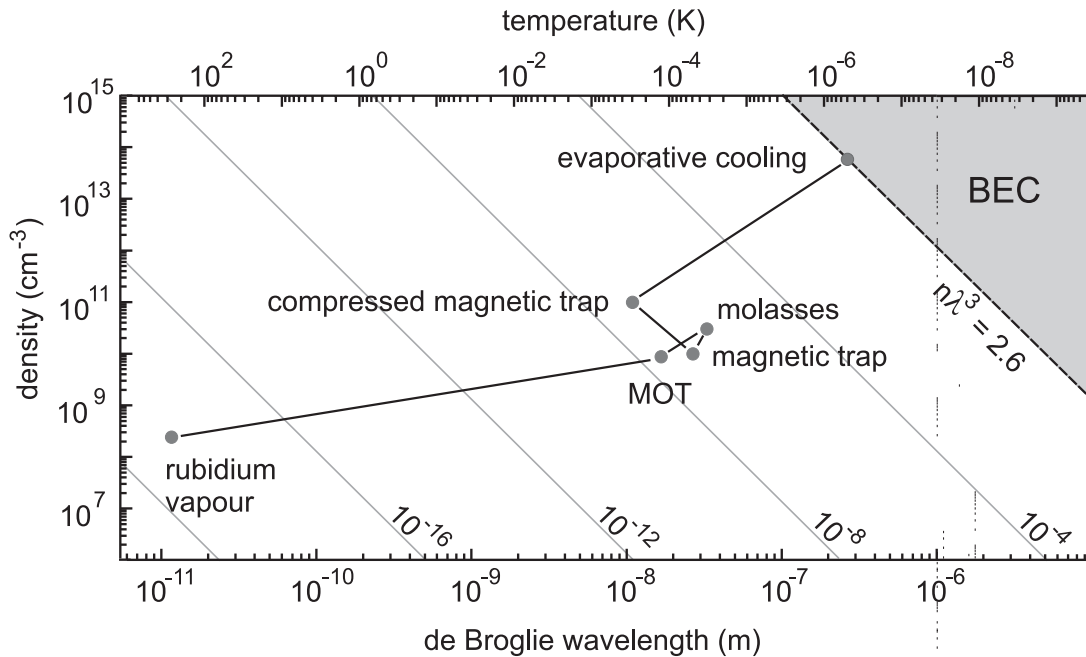


Figure 3.1.: Phase-space odyssey. To reach the BEC phase transition, the phase-space density has to be increased drastically. This is achieved by employing a combination of laser cooling techniques and evaporation cooling.

density must be bridged to reach the phase transition to BEC. This 'phase-space odyssey' is illustrated in Fig. 3.1.

The experimental procedure has been described in detail in previous theses of our group. Hence, we refer the reader to these Refs. [Sch02, Mar03, Vol05, Sya08a] and only sketch the main experimental route to BEC in brief. In order to create a BEC in our setup, we use a two stage cooling scheme. The first stage employs cooling of atoms with laser light in a magneto-optical trap (MOT). This yields a cold sample consisting of up to 10^{10} atoms at temperatures around $10 - 100\mu\text{K}$ and a phase-space density of up to 10^{-6} . For an introduction into the physics of a MOT, see e.g. Ref. [Met99]. The experimental implementation of the MOT in our apparatus is detailed in Ref. [Sch02].

In a second step, the cloud is transferred into a magnetic trap, that creates a conservative, harmonic potential. Then evaporative cooling is applied. To this end, a radio-frequency (rf) field is used to cut off the trap at a specific particle energy. This allows the hottest particles in the cloud to escape from the trap so that the mean energy per atom decreases. Elastic scattering between the remaining particles re-thermalizes the cloud, which can increase phase-space density if the loss of atoms is overcompensated by the reduction of the temperature. As the temperature decreases steadily, it will eventually drop so far below the trap depth that the evaporation rate becomes negligible. This is avoided by slowly lowering the trap depth with the rf field in such a way that a reasonable

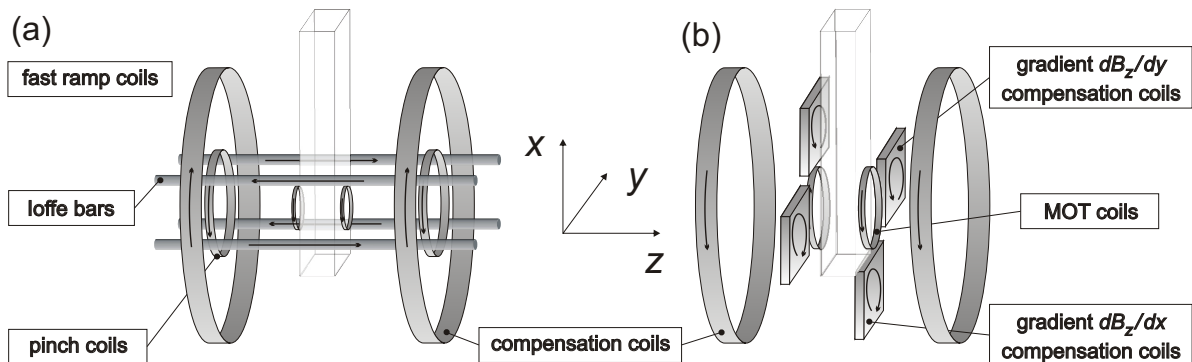


Figure 3.2.: Coil configuration in the experimental setup. (a) The Ioffe-Pritchard magnetic trap consists of the Ioffe bars, the pinch coil pair and the compensation coil pair. In combination with the fast ramp coil pair the latter is also used to create a homogeneous field to address magnetic Feshbach resonances. (b) The magnetic field inhomogeneities of the compensation coils are compensated by the fields of the two gradient compensation coil pairs and the MOT coils. Not drawn to scale.

evaporation rate is maintained as the temperature of the atomic sample is lowered continuously. At the critical temperature T_C , the ground-state population becomes noticeable and grows constantly during further evaporation cooling. The atoms in the ground state form the condensate, while the remaining atoms in excited states represent the thermal cloud.

The evaporative cooling reduces the atom number by ~ 3 orders of magnitude, which in itself would reduce the phase-space density. Nevertheless, the corresponding decrease in temperature is so large that the system crosses the phase transition to BEC. This transition is typically reached for a critical temperature T_C around 500 nK. We typically cool the gas to such low temperatures that there is no discernable thermal fraction left. The cloud contains up to $\sim 2 \times 10^6$ ^{87}Rb atoms in the hyperfine state $|F, m_F\rangle = |1, -1\rangle$. The central density is on the order of 10^{14} cm^{-3} . Fig. 3.2(a) shows the coil configuration of the magnetic trap. For further details of the experimental creation of a BEC in our setup refer to Ref. [Mar03].

3.2. Magnetic Field for Feshbach Resonances

In the experiments performed within this thesis, we use magnetic Feshbach resonances for spin states that are not magnetically trappable. Hence, it is necessary to transfer the BEC from the magnetic trap to an optical dipole trap, which will be described in Sec. 3.3. During the transfer from the magnetic trap to the dipole trap, a guiding field of ~ 1 G preserves the spin polarization of the atoms. When the atoms are confined in the dipole trap we apply a strong homogeneous magnetic field of typically 1000 G in the direction opposite to the guiding field. This field is switched on rapidly thus transferring the atom spins from state $|1, -1\rangle$ to state $|1, +1\rangle$ with almost 100% efficiency [Vol03]. Alternatively,

by deliberately creating an angle between the guiding field and the strong field, the ratio of atoms in states $|1, -1\rangle, |1, 0\rangle$ and $|1, +1\rangle$ can be adjusted.

The 1000 G field is used to address magnetic Feshbach resonances. There are two requirements on this strong magnetic field namely temporal stability and spatial homogeneity which are discussed in Sects. 3.2.1 and 3.2.2, respectively.

3.2.1. Temporal Stability

^{87}Rb has a variety of magnetic Feshbach resonances [Mar03]. Unfortunately, all of them are rather narrow. The broadest resonance is located at $B_{res} = 1007.4$ G and has a width of $\Delta B = 210$ mG [Dür04b], corresponding to a ratio of $\Delta B/B_{res} \sim 2 \times 10^{-4}$. Hence, the magnetic field for addressing the magnetic Feshbach resonances must be stabilized very accurately.

For addressing the magnetic Feshbach resonances two separate pairs of coils are used, see Fig. 3.2(a). The first pair consists of the compensation coils of the magnetic trap. They provide a strong offset field of up to 1270 G at a current of ~ 1760 A. The driving currents are stabilized with a home-built servo loop. The magnetic field noise caused by current fluctuations is below 4 mG (rms) [Dür04b] and thus meets the stringent stability requirements. The second pair of coils adds a few gauss to the strong offset field. This pair of small coils is optimized for fast ramps with ramp speeds of up to 1 G/ μs [Vol07]. Such fast magnetic field ramps are required for experiments [Vol05] that control fast dynamics of the atoms near the Feshbach resonance.

3.2.2. Spatial Homogeneity

The compensation coils are close to, but not quite perfectly in Helmholtz configuration. As a result their magnetic field is not ideally homogeneous. The Stern-Gerlach force on a particle with magnetic moment $\vec{\mu}$ in an inhomogeneous magnetic field is $\vec{F} = |\vec{\mu}| \nabla |\vec{B}(\vec{r})|$ if the direction of $\vec{\mu}$ follows adiabatically the direction of \vec{B} . If atoms in different spin states are exposed to this field, they will experience different forces, which will lead to a spatial separation of the particles.

Experiments with spin mixtures in this apparatus performed prior to the present thesis used tight confinement in deep optical dipole traps to minimize this problem [Mar03]. The experiments reported here, however, require low atomic densities and thus weak confinement. To avoid a spatial separation, the existing gradients therefore have to be compensated by additional coils. Their design is based on the following considerations. The components of the magnetic offset field are expanded in a Taylor series

$$B_i = B_i|_{r=0} + \sum_j \frac{\partial B_i}{\partial x_j} |_{r=0} \cdot x_j + \mathcal{O}(r^2), \quad i \in \{x, y, z\}, \quad (3.2)$$

where $r = 0$ is the trap center. The magnetic field created by the compensation coils is

essentially parallel to the z axis, see Fig. 3.2(b). Hence, to lowest order

$$|\vec{B}| \simeq B_z|_{r=0} + \sum_j \frac{\partial B_z}{\partial x_j}|_{r=0} \cdot x_j. \quad (3.3)$$

Thus, to minimize the Stern-Gerlach force it suffices to compensate only gradients in $B_z(\vec{r})$. For convenience in daily operation, it is desirable to design the gradient compensation coils so that they cancel the gradients without producing an offset field at $r = 0$.

Experimentally, we measured the following uncompensated magnetic field gradients at $|\vec{B}| \sim 1005$ G

$$\frac{\partial B_z}{\partial x}|_{r=0} = -2.2 \frac{\text{G}}{\text{cm}} \quad (3.4)$$

$$\frac{\partial B_z}{\partial y}|_{r=0} = -7.9 \frac{\text{G}}{\text{cm}} \quad (3.5)$$

$$\frac{\partial B_z}{\partial z}|_{r=0} = -2.1 \frac{\text{G}}{\text{cm}}. \quad (3.6)$$

The sign of the measured values is related to the directions indicated by the coordinate system in Fig. 3.2.

The gradient in Eq. (3.6) is compensated using a pair of coils in anti-Helmholtz configuration which is part of the magneto-optical trap, see Fig. 3.2(b). The geometry of this pair of coils yields $(\partial B_z/\partial z)/I \sim 4$ G/(A cm) at a current I [Mar03]. Instead of canceling the field gradient, a gradient of up to 100 G/cm can be applied deliberately to separate different species using the Stern-Gerlach effect. This is particularly useful if applied while the particles are in free flight.

The two remaining gradients given in Eqs. (3.4) and (3.5) are compensated by two additional pairs of square coils which were designed and implemented in the experimental setup during this thesis work. One pair compensates $\partial B_z/\partial x$ and the other pair compensates $\partial B_z/\partial y$. Pictures of these coils are shown in Fig. 3.3. Each coil lies in a plane parallel to the x - y plane. The center of each coil is offset from the symmetry axis of the magnetic trap, see Fig. 3.2(b). The current in one of the coils of a pair is circulating clockwise in the x - y plane, while the current in the other coil of the same pair is circulating counterclockwise. In Fig. 3.4 the magnetic field component B_z created by the gradient $\partial B_z/\partial x$ compensation coils is depicted in a contour plot. The figure shows that the line of constant B_z at the position of the atom cloud is not parallel to the z axis. Hence, the pair of coils produces an undesired gradient $\partial B_z/\partial z$ on top of the desired gradient $\partial B_z/\partial x$. Lack of space forces us to choose a geometry in which the undesired gradient is larger than the desired one. Luckily the undesired gradient can be compensated with the MOT coils. Note that the pair of coils that cancel $\partial B_z/\partial x$ contributes $B_z = 0$ G at the position of the atom cloud. Similar considerations apply to the $\partial B_z/\partial y$ gradient compensation coils.

Before the gradient compensation coils were integrated into the experiment we characterized the gradients using a Förster sensor (*Foerster Magnetoscop 1.069*). The measured

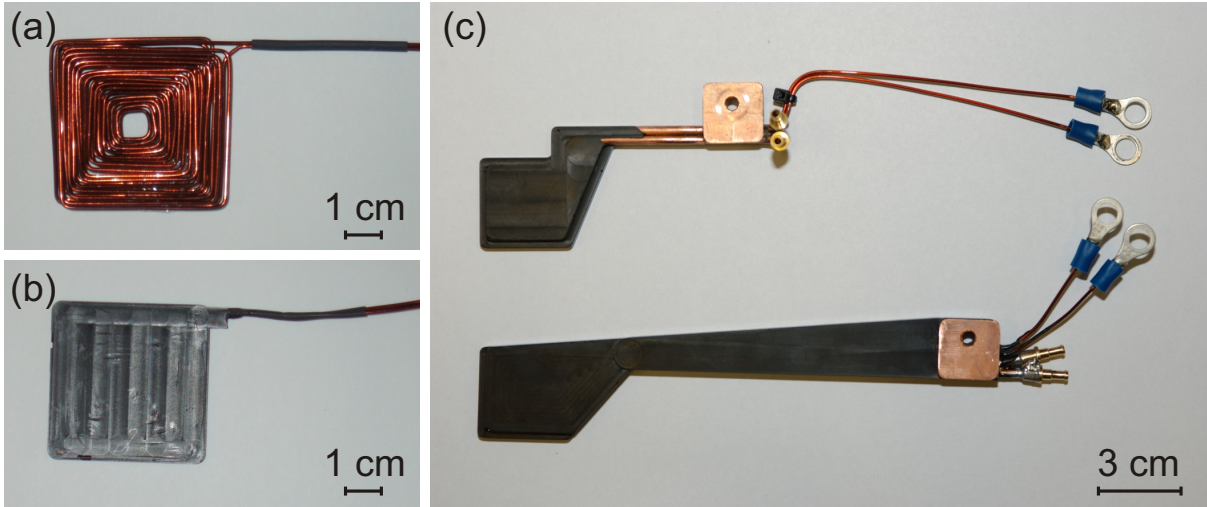


Figure 3.3.: Gradient compensation coils. (a) After winding the wire. (b) After casting the coil into a two component epoxy resin (*STYCAST 2850FT3*). (c) After adding a layer of copper tubing for water cooling. The copper tube is also cast into *STYCAST*.

gradients are

$$\partial B_z / \partial x \text{ coils: } \frac{1}{I} \cdot \frac{\partial B_z}{\partial x} \Big|_{r=0} = +48 \frac{\text{G}}{\text{A cm}}, \quad (3.7)$$

$$\frac{1}{I} \cdot \frac{\partial B_z}{\partial z} \Big|_{r=0} = -65 \frac{\text{G}}{\text{A cm}} \quad (3.8)$$

$$\partial B_z / \partial y \text{ coils: } \frac{1}{I} \cdot \frac{\partial B_z}{\partial y} \Big|_{r=0} = +7.5 \frac{\text{G}}{\text{A cm}}, \quad (3.9)$$

$$\frac{1}{I} \cdot \frac{\partial B_z}{\partial z} \Big|_{r=0} = +44 \frac{\text{G}}{\text{A cm}}, \quad (3.10)$$

and agree well with the theoretical expectation. The coils are water cooled to allow for driving currents of up to 40 A for operation times of up to a few seconds within the 15 s cycle time of the experiment. Typical currents are ~ 25 A. The servo loops for these currents have step response times of $\sim 100 \mu\text{s}$.

3.3. Optical Dipole Trap

Here, the basic principle of dipole traps is presented. For a detailed discussion see e.g. Ref. [Gri00].

An optical dipole trap is created by laser light. The oscillating electric field $\vec{E}(t)$ induces an oscillating dipole moment in the atom due to its frequency-dependent complex polarizability. This dipole moment in turn interacts with the electric field of the laser. This results in an effective energy V_{dip} of the atom, which is proportional to the laser

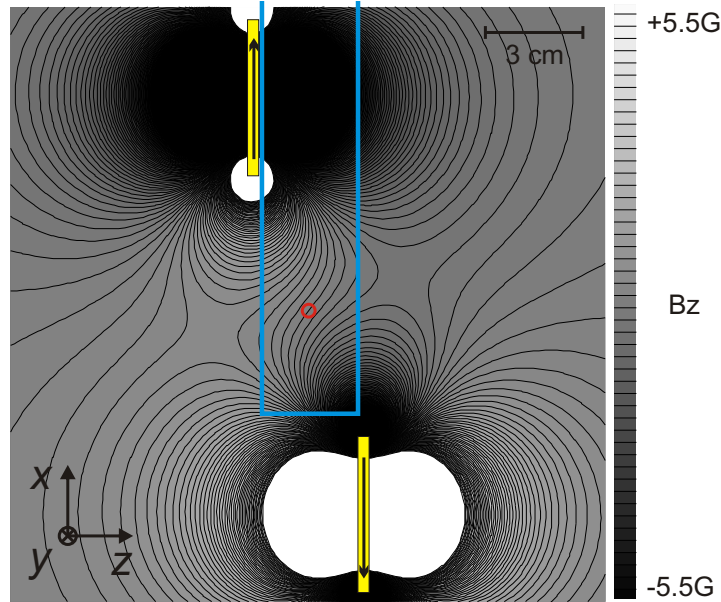


Figure 3.4.: Field created by the gradient compensation coils for $\partial B_z/\partial x$. The color coding shows the theoretically expected values of B_z at $y = 0$ and a current of 5 A. The yellow bars represent the two coils, the blue rectangle indicates the profile of the science chamber and the red circle is the position of the atom cloud.

intensity, $I \propto |\vec{E}|^2$. Therefore, one can use a spatial intensity distribution $I(\vec{r})$ of the light field to create a trapping potential landscape for the atoms. If the laser light is far-detuned from the atomic transition, it can be shown, that the dipole potential is given by [Gri00]

$$V_{dip}(\vec{r}) = \frac{3\pi c^2 \Gamma_0}{2\omega_0^3} \frac{I(\vec{r})}{\Delta}, \quad (3.11)$$

where $\Delta = \omega - \omega_0$ denotes the detuning of the angular frequency ω of the light field with respect to the atomic resonance frequency ω_0 , Γ_0 is the spontaneous emission rate, and c is the speed of light. Beside this conservative potential, the presence of the laser field results also in a spontaneous scattering of laser photons off the atom: photons are absorbed by the atom and re-emitted into the full solid angle. The scattering rate for large detuning is given by [Gri00]

$$\Gamma_{sp}(\vec{r}) = \frac{3\pi c^2 \Gamma_0^2}{2\hbar\omega_0^3} \frac{I(\vec{r})}{\Delta^2} = \frac{V_{dip}(\vec{r})}{\hbar} \frac{\Gamma_0}{\Delta}. \quad (3.12)$$

This leads to heating of the atom cloud due to the photon recoil. The sign of Δ determines the sign of $V_{dip}(\vec{r})$: in the red-detuned case ($\Delta < 0$) atoms will be attracted to regions of maximum intensity, such as the focus of a laser beam. Laser beams typically have a Gaussian transverse intensity profile [Sie86]

$$I(r, z) = \frac{2P}{\pi w^2(z)} e^{-2r^2/w^2(z)}, \quad (3.13)$$

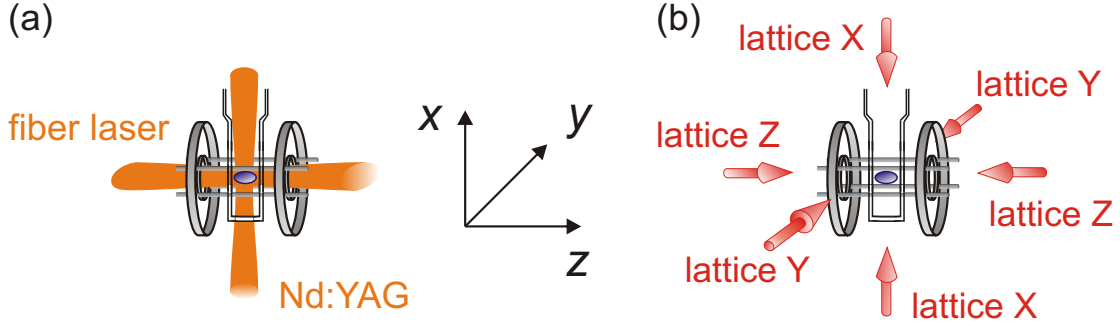


Figure 3.5.: Configuration of laser beams in the experimental setup. (a) The crossed optical dipole trap consists of two intersecting beams. The atoms are trapped in the intersection point inside the science chamber. For orientation, the magnetic trap is also shown in grey. (b) Optical lattice. Three retro-reflected laser beams, one along each coordinate axis, form a 3D optical lattice. Not drawn to scale.

where $w(z) = w_0 \sqrt{1 + (z/z_R)^2}$ is the $1/e^2$ radius of the intensity, w_0 is the waist of the beam, $z_R = \pi w_0^2 / \lambda$ the Rayleigh-length, λ the light wavelength, and P the power of the beam. For the far red-detuned case such a Gaussian beam forms a cylindrically symmetric atom trap. Close to the center, the trapping potential is approximately harmonic with the radial and axial angular trap frequencies

$$\omega_r = \sqrt{\frac{4V_0}{mw_0^2}} \quad \text{and} \quad \omega_z = \sqrt{\frac{2V_0}{mz_R^2}}, \quad (3.14)$$

respectively, where $V_0 = |V_{dip}(\vec{r} = 0)|$. Since $\frac{z_R}{w_0} = \frac{\pi w_0}{\lambda}$ is typically much larger than 1, the axial confinement is much weaker than the radial confinement. In order to have similar confinement in all spatial directions, a crossed dipole trap consisting of two intersecting laser beams can be used. Interference between the two beams can be avoided by using mutually orthogonal polarizations or by choosing different laser wavelengths. In the latter case, the interference pattern moves across the trap with a speed determined by the difference of the laser frequencies. For large enough speed the atomic motion cannot follow the rapid change of the potential and reacts merely to the time-averaged potential, in which the interference term vanishes.

The dipole trap configuration of our setup is shown in Fig. 3.5(a). One beam propagates along the symmetry axis of the magnetic trap (z -axis). It has a beam with an elliptic profile: the waist in the x -direction is $60 \mu\text{m}$ and the waist in the y -direction is $900 \mu\text{m}$. The light for this beam is provided by a single-mode fiber laser (*IPG YLR-20-LP-SF*) with an output power of up to 20 W and a wavelength of 1064 nm. In our experiments the laser power at the position of the atom cloud is typically 1 – 3 W.

The second laser beam has a circular profile with a waist of $55 \mu\text{m}$ and propagates along the vertical direction (x -axis) from the bottom of the glass cell. The light source for this beam is a single frequency Nd:YAG laser (*Innolight Mephisto 2000*) that delivers a

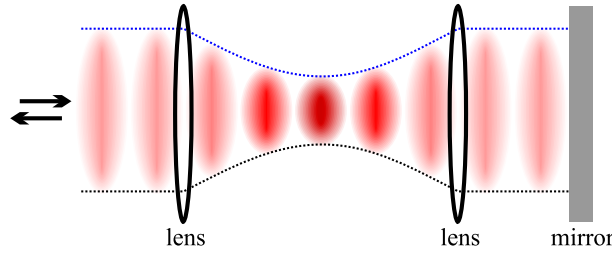


Figure 3.6.: A retro-reflected Gaussian laser beams creates a standing wave pattern.

maximum power of 2 W at a wavelength of 1064 nm. Typically, the power for this beam is around 150 mW at the atoms.

We measured the angular trap frequencies for this crossed dipole trap using parametric heating [Sav97]. Typical frequencies for the experiments performed within this thesis are $(\omega_x, \omega_y, \omega_z) \simeq 2\pi \times (74, 33, 33)$ Hz.

3.4. Optical Lattice

An optical lattice is a regular array of thousands of microtraps formed by a standing wave pattern of an optical dipole potential. Bringing a BEC into such a periodic potential makes it possible to study physical effects that are similar to those occurring in condensed matter systems. However, in contrast to solid state physics, in experiments using an optical lattice most parameters are freely adjustable in real time.

All experiments performed within this thesis use an optical lattice. This section describes the theoretical (Sec. 3.4.1) and the experimental realization (Sec. 3.4.2) of a 3D optical lattice in our apparatus. Lattice alignment and gauging is discussed in Sec. 3.4.3. Finally, in Sec. 3.4.4 we describe the implementation of a new imaging system, that is -in combination with the already existing one- useful for measuring the lattice depth and magnetic field gradients in all three spatial directions.

3.4.1. Periodic Lattice Potentials

The ability of light beams to interfere with each other offers an easy way to create a periodic light intensity pattern. If the Gaussian beam of Eq. (3.13) is retro-reflected, as illustrated in Fig. 3.6, then the intensity pattern becomes

$$I(\vec{r}) = \frac{8P}{\pi w^2(z)} e^{-2(x^2+y^2)/w^2(z)} \cdot \cos^2(kz), \quad (3.15)$$

where $k = 2\pi/\lambda$ is the absolute value of the wave vector. At $x = y = 0$, the corresponding dipole potential (3.11) becomes

$$V(z) = -V_{lat} \cos^2(kz). \quad (3.16)$$

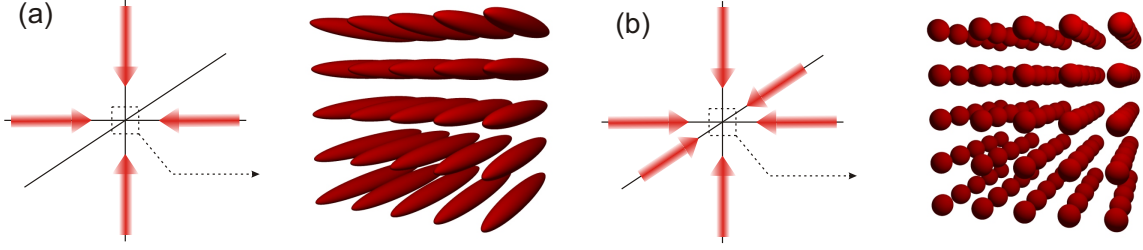


Figure 3.7.: Lattice potential configurations. (a) Two orthogonally intersecting standing waves create a 2D array of tube-shaped atom traps. (b) A simple-cubic optical-lattice potential is formed at the intersection of three mutually orthogonal standing waves.

The lattice depth V_{lat} in units of the recoil energy $E_{rec} = \hbar^2 k^2 / 2m$ is obtained from Eqs. (3.11) and (3.15)

$$\frac{V_{lat}}{E_{rec}} = -\frac{3mc^2}{\hbar^2 k^2 \omega_0^3} \frac{8P \Gamma_0}{w_0^2 \Delta}. \quad (3.17)$$

By superimposing more than one standing wave, multidimensional periodic potentials can be formed. As examples, 2D and 3D lattices are shown in Fig. 3.7. A 2D lattice potential can be used to create an array of tube-shaped 1D traps.

Three standing waves with Gaussian envelope intersecting at right angles form the lattice potential

$$\begin{aligned} V_{3D}(\vec{r}) \simeq & -V_{lat,x} \cdot e^{-\frac{2y^2+z^2}{w_{0,x}^2}} \cdot \cos^2(k_{lat,x} x) \\ & - V_{lat,y} \cdot e^{-\frac{2x^2+z^2}{w_{0,y}^2}} \cdot \cos^2(k_{lat,y} y) \\ & - V_{lat,z} \cdot e^{-\frac{2x^2+y^2}{w_{0,z}^2}} \cdot \cos^2(k_{lat,z} z). \end{aligned} \quad (3.18)$$

This is the realization of the 3D simple cubic lattice shown in Fig. 3.7(b). In our experiment we use Gaussian beams with waists $w_{0,x}$, $w_{0,y}$ and $w_{0,z}$ that are large compared to the size of the atomic sample. As a consequence, the relevant characteristics of the 3D lattice potential can be approximated by the following pseudo-potential

$$V_{3D}(\vec{r}) \simeq \sum_j \left(-V_{lat,j} \cdot \cos^2(k_{lat,j} x_j) + \frac{m}{2} \omega_{\text{eff},j}^2 x_j^2 \right), \quad (3.19)$$

where the Gaussian lattice beam shapes result in a harmonic confinement with angular trap frequencies

$$\omega_{\text{eff},x} = \sqrt{\frac{4V_{lat,x}}{m} \left(\frac{1}{w_{0,y}} + \frac{1}{w_{0,z}} \right)}, \quad \text{and } \omega_y, \omega_z \text{ by cyclic permutation.} \quad (3.20)$$

Close to its center, each individual lattice site forms an approximately harmonic potential, with an angular trapping frequency in the direction of x_j

$$\omega_{lat,j} = \sqrt{2 \frac{V_{lat,j} k_{lat,j}^2}{m}}. \quad (3.21)$$

3.4.2. Experimental Setup

It was part of this thesis to set up a 3D optical lattice configurations. It is simple cubic and operated at a laser wavelength of 830 nm. The three lattice beams intersect at right angles at the position of the atoms, see Fig. 3.5(b). Each lattice beam has a Gaussian transverse profile and is linearly polarized. The polarizations of the three beams are chosen to be mutually orthogonal to avoid interference.

The light is provided by a titanium-sapphire laser (*Coherent MBR E-110*) that is pumped by a frequency-doubled Nd:YVO₄ laser (*Coherent Verdi V-10*) at 532 nm with a power of 10 W. The output power of the Ti:Sa laser is ~ 2 W at a wavelength of 830 nm. The laser has been stabilized onto its internal reference cavity which allows free tuning of the wavelength of the lattice light. The laser has a line width of ~ 100 kHz measured on a time scale of 10 ms at a bandwidth of 50 kHz. The output of the Ti:Sa laser is split up into three beams with a power of 400-450 mW each, see Fig. 3.8. To enable separate intensity control for each beam, we use three acousto-optic modulators (AOM). Mechanical shutters block leakage light at times where the lattice is supposed to be off. The AOM driving frequencies are detuned with respect to each other by 40-200 MHz to eliminate any interference effects between the beams, that would lead to undesired checkerboard lattice structures [Gre03]. Three polarization maintaining optical fibers transfer the beams to the experiment.

Lenses with focal lengths between 600 and 800 mm focus the beams down to waists of $w_j \simeq 135 \mu\text{m}$ at the position of the atoms, resulting in Rayleigh lengths of around 70 mm. After leaving the science chamber, the beams are collimated again and retro-reflected to provide the standing wave configuration of each single lattice beam. The focussing lenses are mounted on 2D translation stages to allow for accurate and reproducible alignment perpendicular to the direction of propagation. The maximum power of each beam is ~ 200 mW at the atom cloud resulting in a lattice depth of up to $\sim 35 E_{rec}$.

For the experiments described in Sec. 6, the lattice beam propagating along z is replaced by a retro-reflected, circularly polarized laser beam at a wavelength of ~ 785 nm. This light is provided by a grating-stabilized diode laser (*Toptica DL100*). Its frequency is beat-locked to an optical frequency comb from the Hänsch group. The comb has a repetition rate of $100 \text{ MHz} \pm 3 \text{ kHz}$ and its carrier envelope offset is $20 \text{ MHz} \pm 3 \text{ kHz}$. The frequency gap between adjacent comb lines is covered by sending the light through a double-pass AOM with a driving frequency between 60 and 100 MHz. The line-width of this diode laser is ~ 100 kHz.

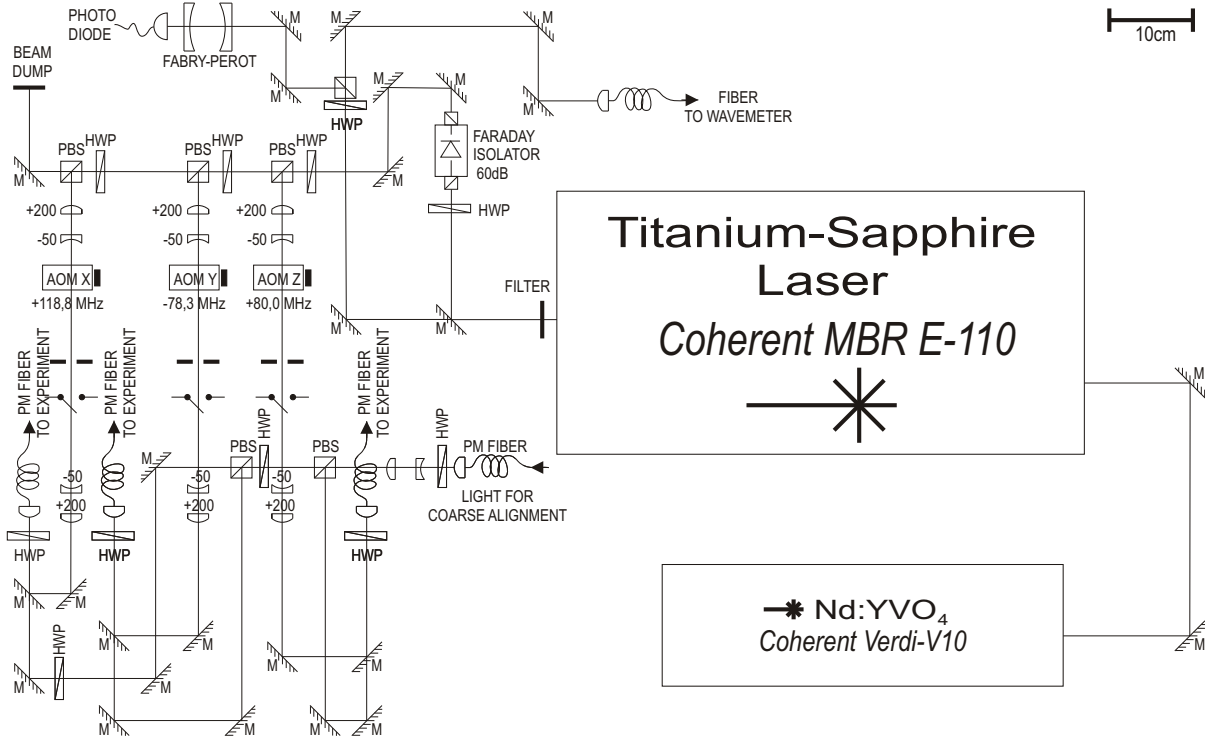


Figure 3.8.: Optical beam path for the 3D optical lattice. The laser light is provided by a titanium-sapphire laser. The output power of the laser is split up into three channels for the x -, y - and z -axis of the optical lattice. The power in each channel is controlled by acousto-optic modulators. The lattice light is transferred to the experiment by optical, polarization-maintaining (PM) fibers. For coarse alignment near resonant light can be coupled into the same fibers. (M = mirror, HWP = half-wave plate, PBS = polarizing beam cube)

3.4.3. Lattice Alignment

Coarse alignment of the lattice is achieved by overlapping the lattice light with near resonant laser light. The latter removes atoms from the dipole trap by photon recoil, which makes coarse alignment easy. Good spatial overlap between the lattice beam and the near-resonant beam is ensured by sending both beams into the same fiber, see Fig. 3.8. For fine alignment, one lattice beam at a time is used in combination with one of the beams of the optical dipole trap to form a crossed dipole trap. To this end, the retro-reflected part of the lattice beam is blocked. By optimizing the atom number and the temperature of the atomic cloud, the lattice beam can be fine adjusted. After this step, the retro-reflected beam is unblocked and coupled back into the optical fiber.

Alternatively or additionally to the former adjustment method, another alignment technique turns out to be rather efficient and easy-to-use in daily operation. This method utilizes the excitation of a sloshing mode inside the optical dipole trap as follows: one lattice beam at a time (without its retro-reflected part) is pulsed on to illuminate the BEC in the optical dipole trap with high power (~ 100 mW). The pulse duration is short

Camera	Andor DV887	ImagingSource DMX 31BF03
detector size	512px \times 512px	1024 \times 768px
pixel size	16 μm \times 16 μm (for 3 \times 3 binning)	4.65 μm \times 4.65 μm
dynamic range	14 bit	10 bit
EMCCD mode	optional	–
numerical aperture (measured)	0.170	0.006
transversal magnification (measured)	3.85(1)	3.29(1)

Table 3.1.: Comparison of the two imaging systems. All numbers are the manufacturer’s specifications if not stated otherwise.

(~ 1 ms) compared to the largest trap frequency of the dipole trap (< 80 Hz). If the focus of the lattice beam is offset from the trap center, this pulse excites a sloshing mode of the atom cloud inside the dipole trap resulting in a shift of the BEC position from the undisturbed position in time-of-flight pictures. By minimizing such shifts in all three lattice directions we usually obtain excellent overall lattice alignments within approximately one hour.

Finally, the lattice depth is characterized by employing the calibration method described in Refs. [Han06, Vol07].

3.4.4. Imaging

For detection of the BEC we use absorption imaging. To this end, a near-resonant laser beam illuminates the BEC after it is released from all trapping potentials. The atom cloud absorbs part of the light and casts a shadow in the beam. The shadow is imaged onto a CCD camera. From the spatial distribution of the light intensity in these images, the atomic density distribution and the atom number can be calculated [Mar03, Die07].

If only one imaging system were used, it would be difficult to align and calibrate the lattice beam that propagates along the imaging axis. Similar problems would occur when trying to measure the magnetic field gradients along the imaging axis. This is why a second imaging system was implemented during this thesis work. Some properties of the two imaging systems are listed in Tab. 3.1. Their setup is shown in Fig. 3.9.

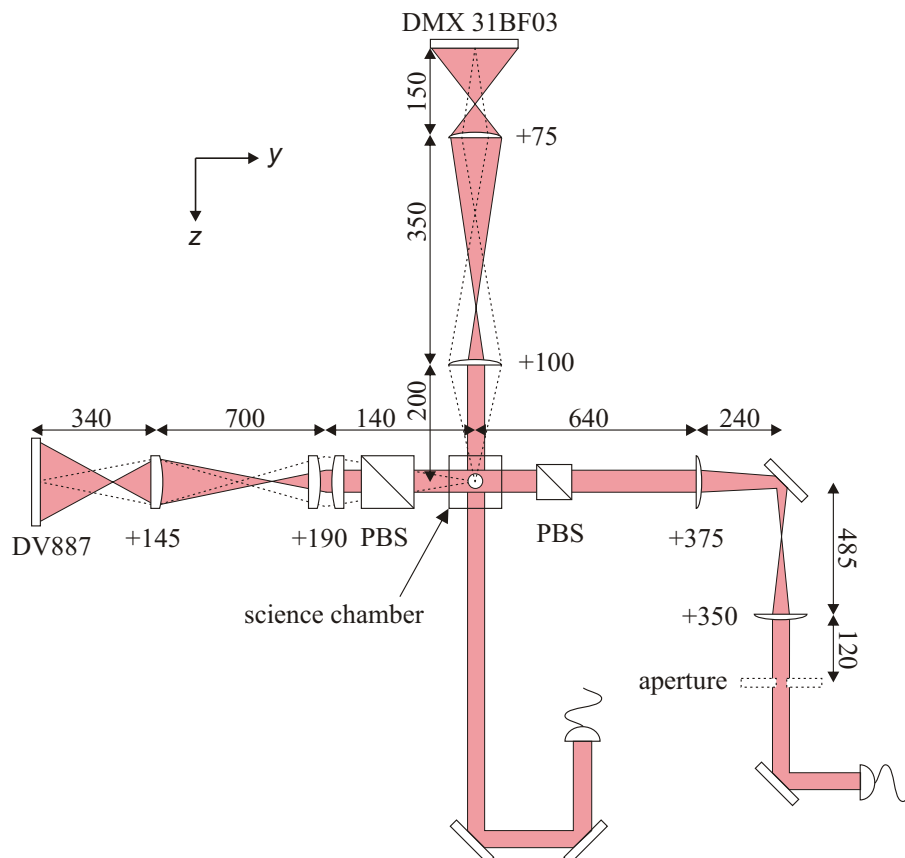


Figure 3.9.: Experimental setup of the two imaging systems. All lengths are given in mm. The atomic cloud is located in the center of the science chamber and is illuminated by near-resonant laser light (red) either along y or z . The atoms absorb photons from the beam. The resulting shadow is imaged onto CCD cameras. Not drawn to scale.

4. Ultracold Feshbach Molecules

During this thesis work, we performed a set of experiments with ultracold Feshbach molecules. This chapter is dedicated to a brief review of these experiments. For more details, we refer to our publications [Vol06, Dür06, Sya07, Sya08b, Dür08, Dür09, GR09] or to previous theses of our group [Vol07, Sya08a].

All the work in this chapter has a common theme, namely a quantum state with exactly one molecule at each site of an optical lattice. In Sec. 4.1, we show the experimental preparation of this state using an adiabatic ramp of the magnetic field across a Feshbach resonance [Vol06, Dür06]. If, however, the ramp is diabatic, a coherent superposition of the atomic and molecular state is created. In Sec. 4.2, we study this superposition for the special case of a square pulse [Sya07]. In Sec. 4.3, we lower the optical lattice depth after preparing the molecular state. This allows the molecules to move and collide along a one-dimensional geometry. These collisions are predominantly inelastic. This offers an alternative route into the strongly correlated regime because our experiment shows that strong dissipation inhibits losses and induces strong correlations [Sya08b, Dür08, Dür09, GR09].

4.1. Preparation of a Quantum State with one Molecule at each Site of an Optical Lattice

A variety of interesting proposals for quantum information processing and quantum simulations [DeM02, Góro2, Lee05, Mic06, Bar06] require as a prerequisite a quantum state of ultracold polar molecules in an optical lattice, where each lattice site is occupied by exactly one molecule. A promising strategy for the creation of such molecules is based on association of ultracold atoms using a Feshbach resonance or photoassociation and a subsequent transfer to a much lower ro-vibrational level using Raman transitions [Sag05]. If the molecule-molecule interactions are predominantly elastic and effectively repulsive, then a state with one molecule per lattice site can finally be obtained using a quantum phase transition from a superfluid to a Mott insulator by ramping up the depth of an optical lattice [Gre02]. However, many molecular species do not have such convenient interaction properties, so that alternative strategies are needed. Here, we demonstrate a technique that is independent of the molecule-molecule interaction properties. The technique relies on first forming an atomic Mott insulator and then associating molecules [Vol06].

The experiment begins with the creation of a BEC of ^{87}Rb atoms in a magnetic trap, see Sec. 3.1. Once created, the BEC is transferred into a crossed-beam optical dipole trap,

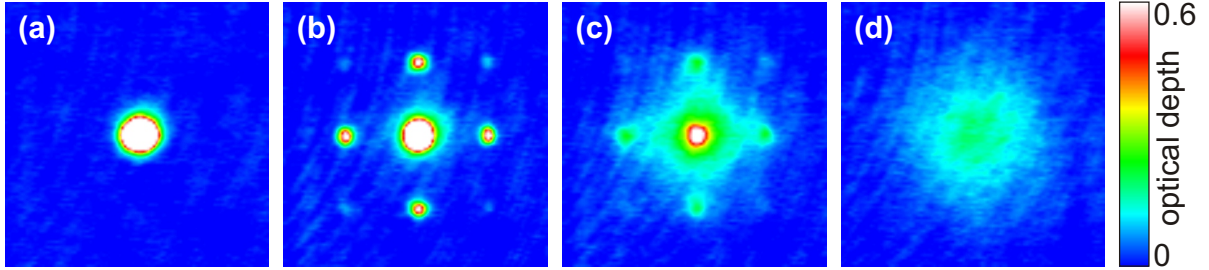


Figure 4.1.: Quantum phase transition from a superfluid to a Mott insulator [Dür06]. The lattice depth is increased to a maximum level and then suddenly switched off simultaneously with all trapping potentials of the atomic sample. After some time of flight, an absorption image is taken. Parts (a)-(d) show images corresponding to a maximum lattice depth of $V_0/E_{rec} = 0, 5, 12,$ and 22 . For small lattice depth, the system is superfluid and diffraction from the lattice light leads to an atomic interference pattern. For a deep lattice, however, the system is in the Mott phase, corresponding to a fixed atom number per lattice site. This results in a maximum uncertainty of the relative phase between sites and therefore the interference pattern is washed out.

see Sec. 3.3. Then a magnetic field of approximately 1000 G is applied, see Sec. 3.2. The atoms are transferred [Vol03] to the absolute ground state $|F = 1, m_F = 1\rangle$, which has a Feshbach resonance at 1007.4 G [Mar02] with a width of 0.2 G [Vol03, Dür04b]. Next, a simple-cubic optical lattice is created by illuminating the BEC with three retro-reflected light beams at a wavelength of $2\pi/k = 830.44$ nm, see Sec. 3.4. We create an atomic Mott insulator by slowly ramping up the depth of the optical lattice.

As an experimental signature for the quantum phase transition from a superfluid to the atomic Mott insulator, one can use time-of-flight images of the atomic sample released from the optical lattice, see Fig. 4.1. The phase transition is predicted [Jak98] to occur at $U/J \approx 35$, corresponding to a lattice depth $V_0/E_{rec} \approx 12$, where $E_{rec} = \hbar^2 k^2 / 2m$ is the recoil energy. This prediction agrees well with the experimental results [Gre02, Vol07]. We carefully checked that an atomic Mott insulator is obtained by repeating all measurements of Ref. [Gre02].

The system has an external harmonic confinement due to the finite waist of the lattice beams and due to the additional dipole trap. This makes the atomic Mott insulator inhomogeneous, see Sec. 2.2.3. By choosing appropriate parameters [Vol06], we ensure that the core of the cloud contains exactly $n = 2$ atoms per lattice site. This core contains 47(3)% out of a total population of 10^5 atoms, which is close to the theoretical limit of 53% [Han06].

After preparing the atomic Mott insulator at a magnetic field of $B = 1008.8$ G, molecules are associated as described in Sec. 2.1.4 [Dür04a]. To this end, the magnetic field is slowly (at 2 G/ms) ramped across the Feshbach resonance at 1007.4 G to a final value of $B = 1006.6$ G. At sites with $n > 1$, atom pairs are associated to molecules. If the site contained $n > 2$ atoms, then the molecule can collide with other atoms or molecules at the same lattice site. This leads to fast loss of the molecule and its collision partner

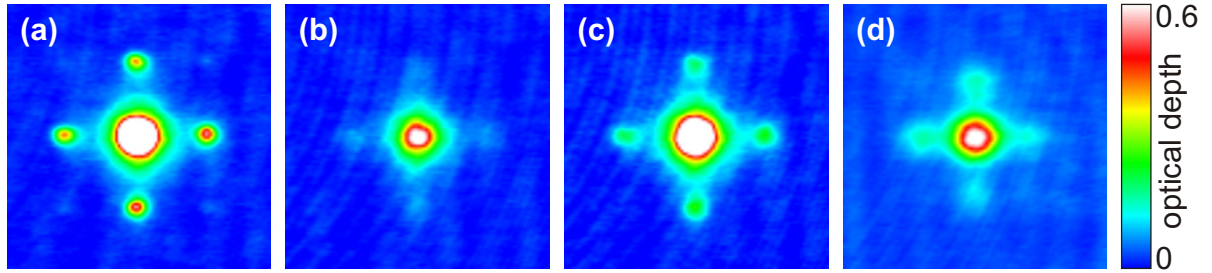


Figure 4.2.: Restoration of phase coherence when probing the quantum state with exactly one molecule per lattice site. (a) An atomic Mott insulator is melted by reducing the lattice depth slowly. The system returns to the superfluid phase and phase coherence is restored. This phase coherence is probed by quickly switching the lattice off and observing an atomic interference pattern in time of flight. (b) After association of molecules, only lattice sites occupied by $n = 1$ atoms contribute to the signal. (c) After association and dissociation of molecules, the satellite peaks are much stronger than in (b), thus proving that the molecular part of the cloud was in a molecular $n = 1$ state. (d) Pure molecular $n = 1$ state. Same as (c) but between association and dissociation, remaining atoms were removed with blast light.

from the trap. The association ramp lasts long enough to essentially empty all sites with $n > 2$ atoms. For lattice sites with $n = 2$ atoms, the association efficiency is close to unity. At a lattice depth of $V_0 = 24E_{rec}$ for atoms, the tunneling amplitude for molecules is negligible compared to the hold time between association and dissociation, so that the positions of the molecules are frozen.

In order to show that the molecular part of the sample really is in the $n = 1$ state (with exactly one molecule at each lattice site), the molecules are first dissociated back into atom pairs by slowly ramping the magnetic field back across the Feshbach resonance. This brings the system back into the atomic Mott insulator state with shells with $n = 1$ and $n = 2$. Then, the atomic Mott insulator is melted by slowly ramping down the lattice from $V_0 = 24E_{rec}$ to $V_0 = 4E_{rec}$. Finally, the lattice is quickly switched off and after some time of flight an absorption image is taken.

Such images are shown in Fig. 4.2. Part (a) shows the result if the magnetic-field ramp for association and dissociation of molecules is omitted. This matter-wave interference pattern shows that phase coherence is restored when ramping down the lattice, thus demonstrating that an atomic Mott insulator is realized at 1008.8 G. Part (b) shows the pattern obtained if molecules are associated but not dissociated, so that they remain invisible in the detection. This signal comes only from sites with $n = 1$ atoms. Part (c) shows the result obtained for the full sequence with association and dissociation of molecules. Obviously, the satellite peaks regain considerable population compared to (b), which proves that after dissociation, we recover an atomic Mott insulator. This shows that association and dissociation must have been coherent and adiabatic. Combined with the freezing of the molecules' positions and the fact that the association starts from an atomic Mott insulator with an $n = 2$ core, this implies that the molecular part of the cloud must have been in a quantum state with one molecule per lattice site.

After associating the molecules, remaining atoms can be removed from the trap using microwave radiation and a blast laser as in Refs. [Xu03, Tha06]. This produces a pure molecular sample. A sub-sequent lattice ramp-down restores phase coherence, as shown in Fig. 4.2(d).

Additional information about the system can be obtained from measurements of the excitation spectrum, which we reported in Refs. [Vol06, Dür06].

4.2. Coherent Atom-Molecule Oscillations

In the last section we discussed the preparation of a quantum state with exactly one molecule on each lattice site using an adiabatic ramp of the magnetic field. Here we report on the preparation of the same quantum state using a diabatic change of the magnetic field. This leads to coherent oscillations between the atomic and the molecular state [Sya07].

The observation of atom-molecule oscillations requires a pulse shape that is strongly diabatic. In free space, such pulses populate [Don02] the continuum of above-threshold entrance-channel states thus leading to oscillations between many levels, typically with small molecular amplitude. We avoid this by working in a deep three-dimensional optical lattice, where the entrance-channel states are discrete. For weak enough coupling, the coupling of the molecular state to only one entrance-channel state is noticeable. In addition, the lattice isolates the molecules from each other, thus suppressing loss due to inelastic collisions [Tha06]. Our experiment starts from an atomic Mott insulator [Gre02] prepared such that the central region of the cloud contains exactly two atoms at each lattice site. The quantum state reached after a half-cycle of the atom-molecule oscillation therefore contains exactly one molecule at each lattice site in this central region, as in Sec. 4.1 [Vol06, Dür06].

We use an optical lattice that is deep enough that tunneling is negligible. In contrast to the free-space case, the closed-channel molecular state $|\psi_m\rangle$ is coupled to only one discrete state, namely the motional ground state $|\psi_a\rangle$ of two entrance-channel atoms at one lattice site, see Sec. 2.1.4. The matrix element $H_{am} = \langle\psi_a|H|\psi_m\rangle$ of the Hamiltonian H is [Sya07, Die07]

$$H_{am} = \left[\frac{4\pi\hbar^2 a_{bg} \Delta\mu \Delta B}{m (\sqrt{2\pi} a_{ho})^3} \left(1 + 0.490 \frac{a_{bg}}{a_{ho}} \right) \right]^{1/2}, \quad (4.1)$$

where $a_{ho} = \sqrt{\hbar/m\omega_{ho}}$ is the harmonic oscillator length, $\omega_{ho} = k\sqrt{2V_0/m}$ as in Eq. (3.21), $2\pi/k = 830.44$ nm the wavelength of the lattice light (see Sec. 3.4.2), m the mass of an atom, V_0 the lattice depth seen by an atom [Vol06], a_{bg} the background scattering length, ΔB the width of the Feshbach resonance, and $\Delta\mu$ the difference between the magnetic moments of an entrance-channel atom pair and a closed-channel molecule. At resonance, oscillations between the two states are expected to occur with angular frequency $\Omega_{\text{res}} = 2H_{am}/\hbar$.

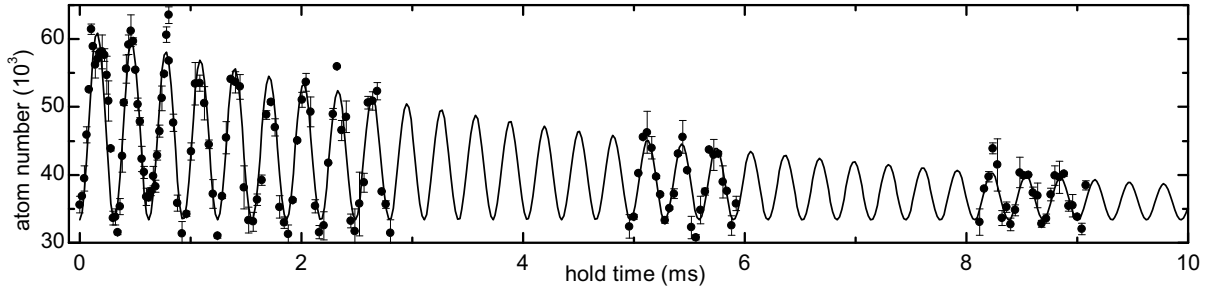


Figure 4.3.: Time-resolved coherent oscillations between the atomic and the molecular state. The experimental data (\bullet) show the number of entrance-channel atoms. The line shows a fit of $N(t) = N_1 + N_2 e^{-t/\tau} (1 - \cos(\Omega t)) / 2$ that yields $\Omega = 2\pi \times 3.221(2)$ kHz and $\tau = 5.9(4)$ ms.

In this experiment, we choose a Feshbach resonance in ^{87}Rb near 414 G with both incoming atoms in the hyperfine state $|F = 1, m_F = 0\rangle$ [Mar02]. A coupled-channels calculation [Kok] predicts $a_{bg} = 100.8$ Bohr radii and $\Delta B = 18$ mG. The Breit-Rabi formula predicts $\Delta\mu = 2\pi\hbar \times 111$ kHz/G. This is an unusually small value that helps reducing Ω_{res} as well as the sensitivity to magnetic field noise.

The experiment begins with the preparation of an atomic Mott insulator with a core containing exactly two atoms at each lattice site, as described in Sec. 4.1. Subsequently, the magnetic field is jumped to a value right at or very close to the Feshbach resonance and is hold for a variable time. Finally, magnetic field, lattice, and dipole trap are abruptly switched off and after 4 ms of free flight an absorption image is taken. The imaging light is resonant with an atomic transition so that molecules remain invisible.

The number of atoms as a function of hold time right at the Feshbach resonance B_{res} is shown in Fig. 4.3. The experimental data clearly show atom-molecule oscillations up to the 29th cycle. The data show damping in a way that the minimum atom number is essentially unchanged. This suggests that the decay is due to loss of population, as opposed to dephasing which would lead to damping towards the mean atom number. We therefore attribute the decay observed in Fig. 4.3 fully to the state $|\psi_m\rangle$. During a cycle, half of the time on average is spent in this state. Hence, the decay rate Γ of population in $|\psi_m\rangle$ can be extracted from the fit in Fig. 4.3 yielding $\Gamma = 2/\tau = 0.34(2)$ kHz.

The fraction of the population that participates in the oscillation at short time is $N_2/(N_1 + N_2) = 0.46(1)$. This value reflects the fraction of lattice sites that are initially occupied by two atoms [Vol06]. The conversion efficiency at these sites is nearly 100%. We repeated the measurements of Ref. [Vol06] in order to verify that the state produced here really is a quantum state in which the central region of the cloud contains exactly one molecule at each lattice site.

The frequency and amplitude of the oscillations depend on the magnetic-field value during the hold time. This dependence is shown in Fig. 4.4. As in any two-level system, the oscillation frequency is expected to follow a hyperbola

$$\Omega(B) = \sqrt{\Omega_{\text{res}}^2 + [(B - B_{\text{res}})\Delta\mu/\hbar]^2}, \quad (4.2)$$

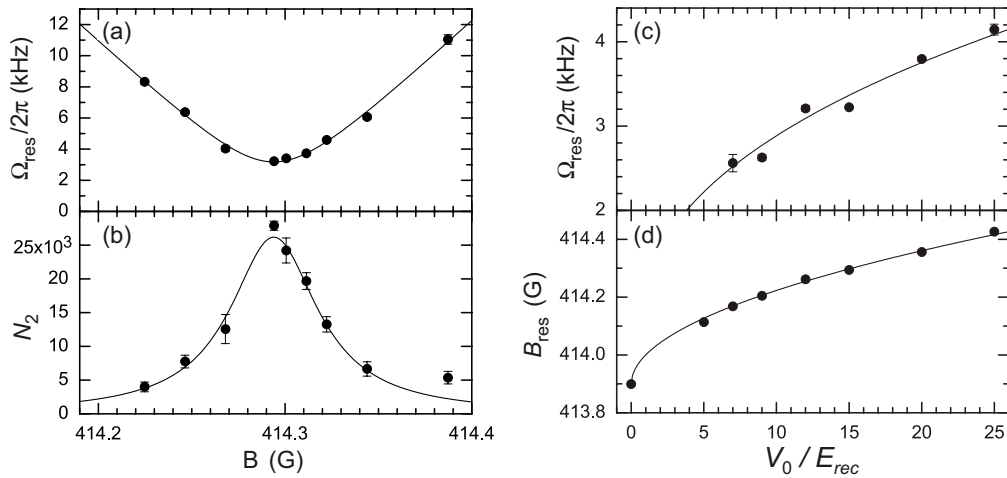


Figure 4.4.: Magnetic-field dependence of (a) the frequency and (b) the amplitude of the oscillations. The lines show fits to the experimental data (\bullet). Dependence of (c) the on-resonance frequency and (d) the Feshbach resonance position on lattice depth. The lines show fits to the data (\bullet).

where B_{res} is the resonance position which depends on the lattice depth V_0 , as discussed further below. A fit to the data is shown in Fig. 4.4(a). The best-fit values are $\Omega_{\text{res}} = 2\pi \times 3.2(1)$ kHz and $\Delta\mu = 2\pi\hbar \times 112(2)$ kHz/G, in good agreement with the result of Fig. 4.3 and the theoretical prediction, respectively.

The amplitude of the oscillation is shown in Fig. 4.4(b) as a function of magnetic field. This amplitude follows a Lorentzian $N_2(B) = N_{\text{res}}\Omega_{\text{res}}^2/\Omega^2(B)$ which is shown in Fig. 4.4(b). We use only N_{res} as a free fit parameter and copy the values of the other parameters from the fit to Fig. 4.4(a).

Ω_{res} depends on the atomic density in the entrance-channel state. In Eq. (4.1) the corresponding effective volume is $(\sqrt{2\pi}a_{ho})^3/(1 + 0.49a_{bg}/a_{ho})$. We varied the lattice depth V_0 in order to verify this density dependence. Results are shown in Fig. 4.4(c). The line shows a fit of Eq. (4.1) to the data, where the only free fit parameter is the overall amplitude. As $\Delta\mu$ and a_{bg} can typically be predicted much more accurately than ΔB , we use this fit to determine $\Delta B = 15(1)$ mG which agrees fairly well with theory.

The measurements of Ω_{res} in Fig. 4.4(c) rely on a measurement of B_{res} as a function of lattice depth V_0 . Results of this measurement are shown in Fig. 4.4(d). Based on the zero-point energy of the three-dimensional harmonic oscillator for the relative motion of the two atoms, one expects [Mor05] $B_{\text{res}} = B_0 + 3\hbar\omega_{ho}/2\Delta\mu$, where B_0 is the value at $V_0 = 0$. The background scattering length a_{bg} causes a correction [Bus98] yielding

$$B_{\text{res}} = B_0 + \frac{\hbar\omega_{ho}}{\Delta\mu} \left(\frac{3}{2} + \sqrt{\frac{2}{\pi}} \frac{a_{bg}}{a_{ho}} \right). \quad (4.3)$$

For magnetic fields between B_0 and B_{res} , the confinement thus stabilizes the molecules against dissociation that would occur in free space [Mor05]. Such confinement induced

molecules can also exist in a 3D band gap in an optical lattice because here dissociation is suppressed by a lack of final states for energies inside the band gap. We use this effect to map the band structure of the optical lattice, as reported in Ref. [Sya07].

The oscillations observed here can be used for precision measurements of atomic scattering properties that could be employed in sensitive tests for drifts of fundamental constants [Chi06]. In addition, confinement-induced molecules offer more general perspectives to manipulate the stability of molecules by structured environments. Finally, the production of a coherent atom-molecule superposition state with controllable amplitude and phase opens up new possibilities for quantum simulations.

4.3. Strong Dissipation Induces Correlations in a Cold Molecular Gas

In Sec. 4.1 and 4.2, we reported on the preparation of a quantum state with exactly one molecule on each lattice site. As mentioned, this state is interesting for a variety of applications and it is a strength of the state preparation procedure that it does not require specific molecule-molecule interaction properties. This is because the lattice is so deep that the tunneling of molecules is irrelevant on the timescale of the experiment.

An interesting aspect of the atomic Mott insulator at moderate lattice depth is that it is a strongly-correlated many-body state induced by the interparticle interaction. This raises the question what happens if the lattice depth is lowered after preparing the molecular state. Will it also evolve into an interaction-induced strongly correlated state? This very question is answered in the present section. We prepare the molecular state as in Sec. 4.1 and subsequently lower the lattice depth of one lattice beam to allow the molecules to tunnel along this direction. We find that an interaction-induced strongly-correlated state is obtained despite the fact that the molecule-molecule interactions are predominantly inelastic [Sya08b].

The molecules studied here are bosons and bosons confined to one dimension are known to form a strongly-correlated state, called Tonks-Girardeau gas [Ton36, Gir60], if they have a strong repulsive interaction. This state, in which bosons are forced to behave much like fermions was observed with atoms in optical lattices [Par04, Kin04]. All this work dealt with conservative interactions. Here we demonstrate an interesting generalization, namely that inelastic collisions produce a dissipative analogue of the Tonks-Girardeau gas [Sya08b]. Inelastic collisions between the molecules create strong correlations that suppress the molecule loss rate. We dramatically increase this suppression by adding a lattice along the 1D direction. This work offers perspectives to create other, and possibly new, strongly correlated states using dissipation [Sac99, Wen04].

It may seem surprising that inelastic interactions can be used to reach the strong correlation regime because inelastic collisions are generally associated with particle losses. This behavior can be understood by using an analogy in classical optics, where light absorption is expressed by an imaginary part of the electric susceptibility χ , which gives rise to a complex refractive index $n = \sqrt{1 + \chi}$. If an electromagnetic wave impinges

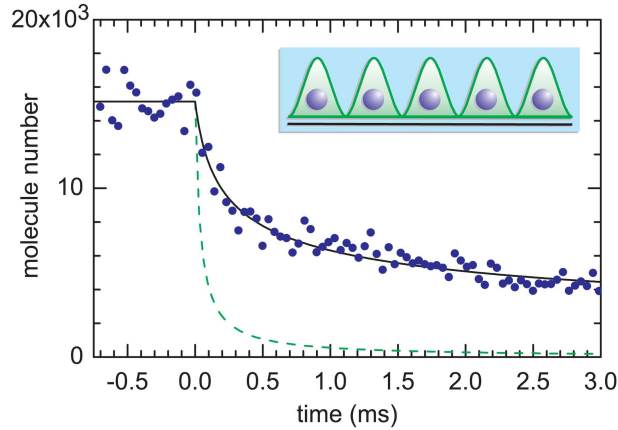


Figure 4.5.: Time-resolved loss of the number of molecules in 1D tubes. If the system were uncorrelated the loss would be expected to follow the dashed line, which is way off the experimental data (\bullet). A fit to the data (solid line) reveals that the probability to find two particles at the same position is reduced by a factor of ~ 10 compared to an uncorrelated system, thus showing that the system is strongly correlated [Sya08b].

perpendicularly on a surface between two media with complex refractive indices n_1 and n_2 , then a fraction $|(n_1 - n_2)/(n_1 + n_2)|^2$ of the intensity will be reflected. In the limit $|n_2| \rightarrow \infty$, the light is perfectly reflected off the surface, irrespective of whether n_2 is real or complex. In our case, bosons interacting with large imaginary [Ver94, Boh97, Dür09] scattering length almost perfectly reflect off each other for an analogous reason, thereby giving rise to the same constraints in the particles' wave function as the ones corresponding to elastic collisions, and thus to the same physical phenomena. In our experiment, the correlations manifest themselves in a strong suppression of the rates at which particles are lost due to inelastic collisions.

Our experiment starts from the pure molecular state, as described in Sec. 4.1. After state preparation, the lattice depth along one direction V_{\parallel} is linearly ramped down to a final value. After this ramp, we have an array of tubes of 1D molecular gases (see also Sec. 3.4.1) and the system is allowed to evolve for a variable hold time at the final value of V_{\parallel} . During this hold time, molecules collide inelastically, leading to loss. After the hold time, all molecules are dissociated into atom pairs using the Feshbach resonance. The dissociation terminates the loss. Finally, the magnetic field and the lattice light are switched off simultaneously, and the number of atoms is determined from a time-of-flight absorption image.

Loss of particles due to inelastic two-body collisions occurs only if the particles come close together. The rate at which the loss occurs thus depends on the pair correlation function $g^{(2)}$ according to [Sya08b]

$$\frac{dn}{dt} = -K_2 n^2 g^{(2)}, \quad (4.4)$$

where n is the 1D density of particles and K_2 is a rate coefficient, which can be determined

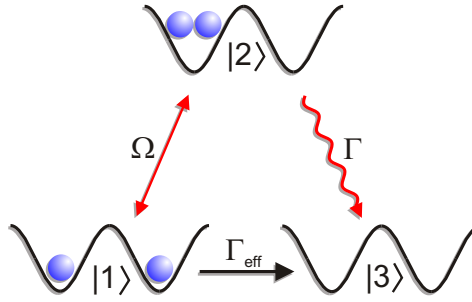


Figure 4.6.: Understanding the loss in terms of the quantum Zeno effect. The initial state $|1\rangle$ contains exactly one particle at each site of a double-well potential. Tunneling with amplitude Ω coherently couples this state to state $|2\rangle$, where both particles occupy the same site. In this configuration, the particles can collide inelastically, resulting in loss of both particles, thus transferring the system into state $|3\rangle$. The rate coefficient for this incoherent loss is Γ . In the limit $\Omega \ll \Gamma$, loss from the initial state occurs at an effective rate $\Gamma_{\text{eff}} = \Omega^2/\Gamma$ [CT92]. If Γ is large, then Γ_{eff} becomes small. Fast dissipation thus freezes the system in its initial state, which can be interpreted as a manifestation of the continuous quantum Zeno effect [Mis77].

from independent measurements. A measurement of the loss rate can thus serve as a probe whether the strongly correlated regime is reached.

Figure 4.5 shows experimental data (\bullet) for the decay of the molecule number as a function of the hold time. No noticeable loss is observed during the lattice ramp down, which begins at $t = -0.5$ ms and ends at $t = 0$. The subsequent loss differs significantly from the expectation for an uncorrelated system (dashed line), which is calculated from the independently determined parameters of the system, including a measurement of the 3D loss rate coefficient in Ref. [Sya06]. The solid line shows a fit to the data that reveals a value of $g^{(2)} = 0.11 \pm 0.01$, see Ref. [Sya08b] for details. The fact that $g^{(2)}$ differs from 1 by a large factor shows that the system is strongly correlated, thus realizing a dissipative Tonks-Girardeau gas.

An interesting variation of this experiment is obtained when considering the situation where the lattice depth V_{\parallel} along the 1D tubes is lowered to a nonzero value. Of course, this is closely related to the above experiment, but there are three aspects that make this system interesting: first, the case $V_{\parallel} \neq 0$ offers new physical insight because the reduction of the loss can be interpreted in terms of the quantum Zeno effect as illustrated in Fig. 4.6, second, time-resolved calculations of the dynamics of the loss become numerically feasible, and third, a much larger suppression of $g^{(2)}$ is obtained.

The pair-correlation function can again be determined from time-resolved measurements of the loss of molecule number. Results are shown in Fig. 4.7(a) for three different lattice depths. We extract $g^{(2)}$ from such loss curves and show them in (b) as a function of V_{\parallel}/E_r , where E_{rec} is the molecular recoil energy. The solid line shows an analytical model discussed in Refs. [Sya08b, Dür09] that represents essentially the Zeno effect illustrated in Fig. 4.6. In addition, we performed time-resolved numerical calculations that make much fewer approximations than the analytical model [GR09]. The numerical results are also

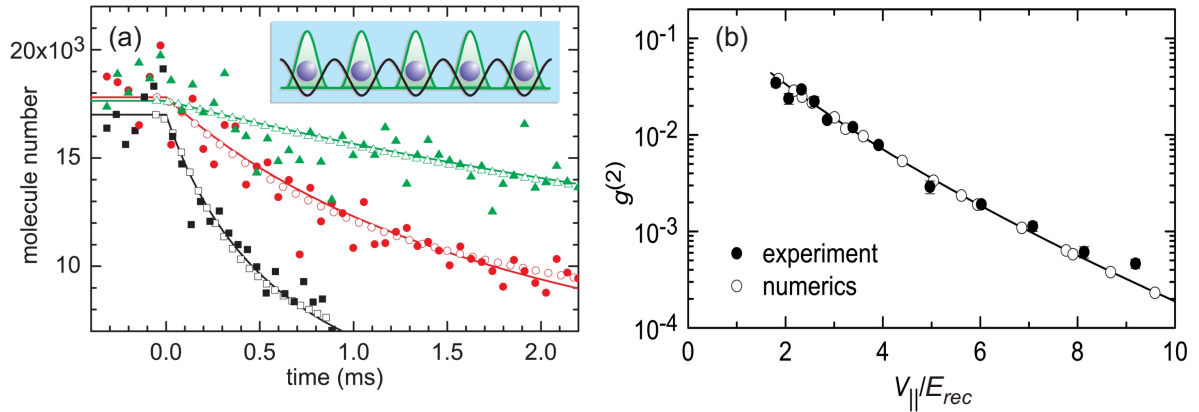


Figure 4.7.: Loss at different lattice depths $V_{||}$. (a) Solid lines show fits to the experimental data (solid symbols) that reveal the pair correlation function $g^{(2)}$. Open symbols show results of our numerical calculations [GR09]. Black squares, red circles, and green triangles correspond to $V_{||}/E_{rec}$ values of 1.8, 3.9, and 6.0, respectively. (b) $g^{(2)}$ as a function of the lattice depth applied along the one dimension. Experimental data (\bullet), numerical results (\circ) [GR09], and analytical model (solid line) [Sya08b] agree well with each other.

shown in Fig. 4.7 and agree well with the analytical model and the experimental data. The lowest value of $g^{(2)}$ measured here is $\sim 1/2000$.

The experimental results presented here show that strong inelastic collisions can inhibit particle losses and drive a system into a strongly-correlated regime. Strong interactions are responsible for many interesting quantum phenomena in many-body systems: high- T_C superconductivity [And87], excitations with fractional statistic [Wil82], topological quantum computation [Kit03], and a plethora of exotic behaviors in magnetic systems [Aue94]. The mechanism introduced here could also give rise to other strongly-correlated states, such as a Laughlin state [Sto99] or one with anyonic excitation [Wil82]. The present work opens up the possibility of observing exotic quantum many-body phenomena in systems that suffer from strong inelastic collisions. Furthermore, the rate coefficients for those collisions may be artificially increased using photoassociation or Feshbach resonances, thus further reducing the actual loss rate in the strongly-correlated regime.

5. Optical Control of a Magnetic Feshbach Resonance

In this chapter we explore a novel scheme for controlling the scattering length with laser light [Bau09b, Bau09a]. We show theoretically (Sec. 5.2) and experimentally (Sec. 5.5), that light near-resonant with a molecular bound-to-bound transition in ^{87}Rb can be used to shift the magnetic field at which a magnetic Feshbach resonance occurs. This makes it possible to tune the interaction strength with laser light and at the same time induce considerably less loss than an optical Feshbach resonance would do. To find an appropriate bound-to-bound transition, we perform excited-state spectroscopy (Sec. 5.3). Furthermore, when applying laser light resonant with such a bound-to-bound transition we observe an Autler-Townes splitting of the magnetic Feshbach resonance (Sec. 5.4).

5.1. General Concept

Many properties of ultracold gases are determined by the interparticle interaction which is characterized by the s -wave scattering length a , see Sec. 2.1. This makes it desirable to tune this parameter. A much-used method for this purpose is a magnetic Feshbach resonance [Moe95, Ino98, Chi09], see Sec. 2.1.2. An alternative method is a photoassociation resonance, which is sometimes also called optical Feshbach resonance [Fed96, Boh97, Fat00, The04, Tha05, Jon06], see Sec. 2.1.3. A major advantage of optical Feshbach resonances is that the light intensity can be varied on short length and time scales, thus offering more flexible experimental control over the scattering length. The problem with photoassociation resonances is that the light induces inelastic collisions between atoms which lead to rapid loss of atoms. The experiments in Refs. [The04, Tha05] both demonstrated a change of $\text{Re}(a)/a_{\text{bg}} - 1 \sim \pm 1$ in ^{87}Rb , where a_{bg} is the background value of a by applying an optical Feshbach resonance. For these parameters, both experiments incurred losses characterized by a two-body rate coefficient K_2 with an estimated value of $\sim 10^{-10} \text{ cm}^3/\text{s}$. Typical densities on the order of 10^{14} cm^{-3} result in lifetimes on the order of $100 \mu\text{s}$, which is too short for many applications. This is why photoassociation resonances have only rarely been used experimentally to tune the scattering length. Alkaline earth atoms offer the possibility to use photoassociation on narrow intercombination lines which results in smaller loss rates [Eno08]. But this is not feasible in the large number of experiments with alkali atoms.

Our method makes an optical manipulation of the scattering length possible, which offers great flexibility for future experiments because the interaction strength can be

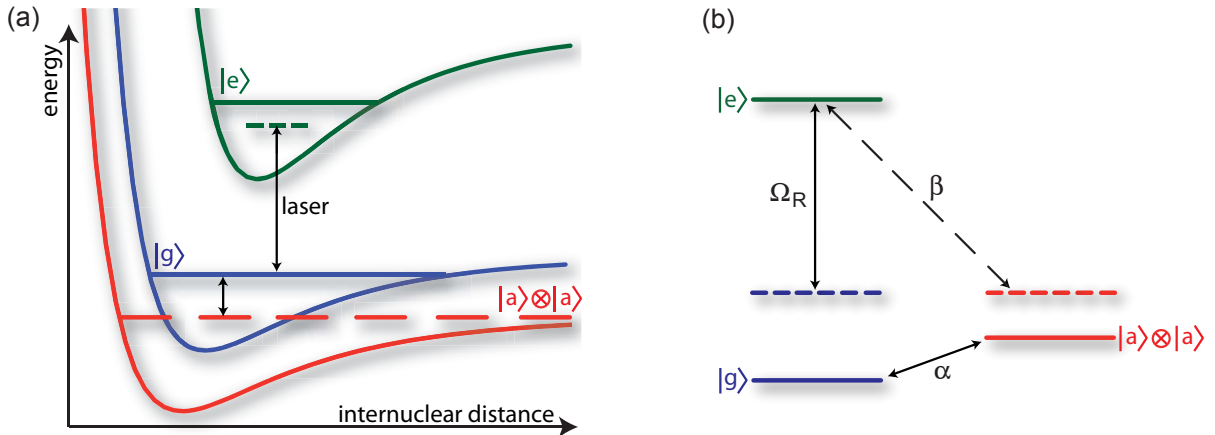


Figure 5.1.: Level scheme. (a) The Feshbach resonance couples atoms at threshold in the incoming channel $|a\rangle \otimes |a\rangle$ to a bound dimer state $|g\rangle$ in a different potential. A laser is near resonant with a bound-to-bound transition from $|g\rangle$ to an electronically excited dimer state $|e\rangle$. (b) Different couplings in our scheme. The coupling strength α induces a magnetic Feshbach resonance between $|a\rangle$ and $|g\rangle$. The laser couples $|g\rangle$ to $|e\rangle$ with Rabi frequency Ω_R . This causes an ac-Stark shift (not shown) of state $|g\rangle$ which leads to a shift of the magnetic field at which the Feshbach resonance occurs. Typically, the same light can also drive photoassociation from state $|a\rangle \otimes |a\rangle$ to state $|e\rangle$ with coupling strength β . The light frequency is typically somewhat detuned from both transitions.

controlled rapidly and with high spatial resolution using light intensity patterns. The advantage compared to an optical Feshbach resonance is that much less particle loss is induced. We show that our method reduces the light-induced atom-loss rate by up to two orders of magnitude.

A further application is to shift one Feshbach resonance on top of another to explore the coupling between the two. Yet another possible application can be found in ^{133}Cs . Its hyperfine state $|F = 3, m_F = 3\rangle$ has a very broad Feshbach resonance at a slightly negative magnetic field. Applications of this Feshbach resonance are hampered by rapid loss due to dipolar relaxation at negative magnetic field. Shifting this resonance to a positive magnetic field would make it accessible for experiments, such as studies of Efimov physics [Kra06].

5.2. Combination of a Magnetic Feshbach Resonance and an Optical Bound-to-bound Transition

A basic level scheme for our technique is shown in Fig. 5.1. A light field is near-resonant with a bound-to-bound transition from the dimer state $|g\rangle$ in the electronic ground state to an electronically excited dimer state $|e\rangle$. The scheme uses the existing coupling between an atom-pair state $|a\rangle \otimes |a\rangle$ and a molecular state $|g\rangle$ near a Feshbach resonance with coupling strength α , as shown in Fig. 5.1(b). By adding a light field with Rabi frequency

Ω_R that is somewhat detuned from a bound-to-bound transition between state $|g\rangle$ and an electronically excited molecular state $|e\rangle$, one can induce an ac-Stark shift of state $|g\rangle$. This results in a shift of the magnetic field B_{res} at which the Feshbach resonance occurs. If the magnetic field B is held close to the Feshbach resonance, then spatial or temporal variations of the light intensity affect the scattering length. In general, the light field can also drive a transition from state $|a\rangle \otimes |a\rangle$ to state $|e\rangle$ with coupling strength β .

This model is closely related to previous studies of the combination of a Feshbach resonance with a photoassociation resonance, see *e.g.* Refs. [vA98, Jun08, Mac08]. Unlike those references, we are mostly interested in the Feshbach resonance and the bound-to-bound transition. The photoassociation is a nuisance in our scheme, because any useful change of $\text{Re}(a)$ that it induces is inevitably accompanied by the loss rates that limited the photoassociation experiments in Refs. [The04, Tha05].

5.2.1. Mean-Field Model

Our theoretical model can be developed as follows. We assume that the population in each state is Bose condensed and can be described by a mean field ψ_a , ψ_g and ψ_e for the atomic state $|a\rangle$, the dimer state $|g\rangle$ and the electronically excited dimer state $|e\rangle$, respectively. Generalizing Ref. [Tim99], we obtain the following equations [Bau09a]

$$i \frac{d}{dt} \psi_a = \frac{E_a^{\text{int}}}{\hbar} \psi_a + \frac{U_{\text{bg}}}{\hbar} |\psi_a|^2 \psi_a + 2\alpha^* \psi_a^* \psi_g + 4\beta^* \psi_a^* \psi_e \cos(\omega_L t) \quad (5.1a)$$

$$i \frac{d}{dt} \psi_g = \alpha \psi_a^2 + \frac{E_g^{\text{int}}}{\hbar} \psi_g + \Omega_R^* \psi_e \cos(\omega_L t) \quad (5.1b)$$

$$i \frac{d}{dt} \psi_e = (2\beta \psi_a^2 + \Omega_R \psi_g) \cos(\omega_L t) + \frac{E_e^{\text{int}}}{\hbar} \psi_e. \quad (5.1c)$$

E_j^{int} is the internal energy of the state $j \in \{a, g, e\}$ and depends nonlinearly on the magnetic field B . Near the pole of the unshifted Feshbach resonance B_{pole} , it can be approximated as linear

$$E_j^{\text{int}} = -\mu_j (B - B_{\text{pole}}) + \hbar \omega_{eg} \delta_{ej}, \quad (5.2)$$

where μ_j is a magnetic dipole moment and δ_{ij} is the Kronecker symbol. At $B = B_{\text{pole}}$, the internal states $|a\rangle$ and $|g\rangle$ are degenerate whereas the internal state $|e\rangle$ has an energy offset $\hbar \omega_{eg}$.

$U_{\text{bg}} = 4\pi \hbar^2 a_{\text{bg}}/m$ describes the atomic mean-field energy between atoms and is related to the background scattering length a_{bg} and the atomic mass m .

The electric field of the laser light is of the form $E = -E_0 \cos(\omega_L t)$ with amplitude E_0 and angular frequency ω_L and causes a coupling on the bound-to-bound transition $|g\rangle \leftrightarrow |e\rangle$. The corresponding Rabi frequency is $\Omega_R = d_{eg} E_0 / \hbar$, where $d_{eg} = \langle e | d | g \rangle$ is the matrix element of the electric dipole moment.

The parameter α describes the coupling between states $|a\rangle$ and $|g\rangle$, which causes the Feshbach resonance. The parameter $\beta \propto E_0$ describes photoassociation from state $|a\rangle$ to $|e\rangle$.

We move to an interaction picture by replacing $\psi_e \rightarrow \psi_e e^{-i\omega_L t}$ and perform a rotating-wave approximation by neglecting coefficients rotating as $e^{\pm 2i\omega_L t}$. We then move to another interaction picture by replacing $\psi_j \rightarrow \psi_j \exp((2 - \delta_{aj})iE_a^{\text{int}}t/\hbar)$. Hence

$$i\frac{d}{dt}\psi_a = \frac{U_{\text{bg}}}{\hbar}|\psi_a|^2\psi_a + 2\alpha^*\psi_a^*\psi_g + 2\beta^*\psi_a^*\psi_e \quad (5.3a)$$

$$i\frac{d}{dt}\psi_g = \alpha\psi_a^2 + \Delta_g\psi_g + \frac{1}{2}\Omega_R^*\psi_e \quad (5.3b)$$

$$i\frac{d}{dt}\psi_e = \beta\psi_a^2 + \frac{1}{2}\Omega_R\psi_g + \left(\Delta_e - \frac{i}{2}\gamma_e\right)\psi_e, \quad (5.3c)$$

where we abbreviated

$$\Delta_g = \frac{1}{\hbar}\mu_{ag}(B - B_{\text{pole}}) \quad (5.4a)$$

$$\Delta_e = -\Delta_L + \frac{1}{\hbar}\mu_{ae}(B - B_{\text{pole}}) \quad (5.4b)$$

$$\Delta_L = \omega_L - \omega_{eg} \quad (5.4c)$$

with $\mu_{ag} = 2\mu_a - \mu_g$ and $\mu_{ae} = 2\mu_a - \mu_e$. In Eq. (5.3c) we included an *ad hoc* decay rate γ_e that represents spontaneous radiative decay from state $|e\rangle$ into states that are not included in the model, similar to Ref. [vA99b].

Note that the typical interatomic distance is orders of magnitude larger in the atomic gas than within a single molecule. For a typical excited state, this results in

$$|\beta\psi_a| \ll |\Omega_R|. \quad (5.5)$$

5.2.2. Scattering Length

We assume that all the population is initially prepared in state $|a\rangle$ and that the populations in states $|g\rangle$ and $|e\rangle$ will remain small at all times so that they can be eliminated adiabatically, similar to Refs. [vA99b, Mac08]. This is a good approximation, e.g., if the angular frequencies $\alpha\psi_a$ and $\beta\psi_a$ are both small compared to Ω_R and γ_e or compared to Δ_e and Δ_g . This condition is always satisfied in the low-density limit, but for a very broad Feshbach resonance it might be difficult to reach this regime experimentally.

The adiabatic elimination is achieved by formally setting $(d/dt)\psi_g = (d/dt)\psi_e = 0$. This is used to eliminate ψ_g and ψ_e from Eq. 5.3. We obtain

$$i\frac{d}{dt}\psi_a = \frac{4\pi\hbar a}{m}|\psi_a|^2\psi_a \quad (5.6)$$

with the complex-valued scattering length [Bau09b, Bau09a]

$$a = a_{\text{bg}} - \frac{m}{2\pi\hbar} \frac{|\alpha|^2(\Delta_e - i\gamma_e/2) - \text{Re}(\alpha^*\Omega_R^*\beta) + |\beta|^2\Delta_g}{(\Delta_e - i\gamma_e/2)\Delta_g - |\Omega_R/2|^2}. \quad (5.7)$$

The term $\text{Re}(\alpha^* \Omega_R^* \beta)$ represents interference between the two possible ways to go from state $|a\rangle$ to state $|e\rangle$, either directly or indirectly through state $|g\rangle$.

The real part of the scattering length is responsible for the mean-field energy [Dür09]. We assume that a_{bg} is real and obtain

$$\text{Re}(a) = a_{\text{bg}} - \frac{m}{2\pi\hbar} \frac{\left(|\alpha|^2 \Delta_e - \text{Re}(\alpha^* \Omega_R^* \beta) + |\beta|^2 \Delta_g\right) \left(\Delta_e \Delta_g - |\Omega_R/2|^2\right) + |\alpha|^2 \Delta_g (\gamma_e/2)^2}{(\Delta_g \Delta_e - |\Omega_R/2|^2)^2 + (\Delta_g \gamma_e/2)^2}. \quad (5.8)$$

The imaginary part of the scattering length gives rise to two-body loss with a rate equation

$$\frac{dn}{dt} = -K_2 n^2 g^{(2)} \quad (5.9a)$$

$$K_2 = -\frac{8\pi\hbar}{m} \text{Im}(a), \quad (5.9b)$$

where $n = |\psi_a|^2$ is the atomic density, K_2 is the two-body loss coefficient for a BEC, and $g^{(2)}$ is the pair correlation function at zero relative distance. For a BEC with N atoms $g^{(2)} = 1 - 1/N$. Insertion of Eq. (5.7) yields

$$K_2 = 2\gamma_e \frac{|\alpha \Omega_R/2|^2 - \Delta_g \text{Re}(\alpha^* \Omega_R^* \beta) + |\beta|^2 \Delta_g^2}{(\Delta_g \Delta_e - |\Omega_R/2|^2)^2 + (\Delta_g \gamma_e/2)^2}. \quad (5.10)$$

All terms in the numerator are $\propto E_0^2$, so that the relative importance of the terms is independent of laser intensity.

Figure 5.2 shows predictions for $\text{Re}(a)/a_{\text{bg}}$ and K_2 as a function of B . For large $|\Omega_R|$, one can clearly see two resonances in K_2 each of which is approximately Lorentzian. Each of these resonances is accompanied by a dispersive feature in $\text{Re}(a)/a_{\text{bg}}$.

We show now that our model reproduces known results from the literature in the special cases of a pure magnetic Feshbach resonance or a pure photoassociation resonance. For a pure magnetic Feshbach resonance ($\beta = \Omega_R = 0$), see Sec. 2.1.2, Eq. (5.7) yields the familiar result [Moe95]

$$a = a_{\text{bg}} \left(1 - \frac{\Delta B}{B - B_{\text{pole}}}\right) \quad (5.11)$$

with the width of the Feshbach resonance

$$\Delta B = \frac{2\hbar^2 |\alpha|^2}{U_{\text{bg}} \mu_{ag}}. \quad (5.12)$$

For a pure photoassociation resonance ($\alpha = \Omega_R = 0$), see Sec. 2.1.3, Eq. (5.7) yields

$$a = a_{\text{bg}} - \frac{m}{2\pi\hbar} \frac{|\beta|^2}{\Delta_e - i\gamma_e/2}, \quad (5.13)$$

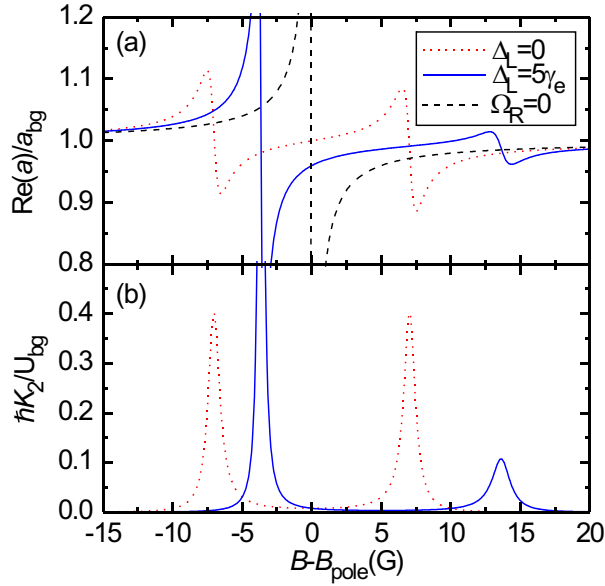


Figure 5.2.: Predictions for $\text{Re}(a)/a_{\text{bg}}$ and K_2 as a function of B from Eqs. (5.8) and (5.10). For all curves, we choose $\hbar\gamma_e/\mu_{ae} = 2$ G, $\beta = 0$, and $\Delta B = 0.2$ G; with ΔB defined in Eq. (5.12). The dotted lines (red) are for resonant laser light $\Delta_L = 0$ and $\hbar|\Omega_R|^2/\gamma_e\mu_{ag} = 100$ G. They show two resonances that are symmetrically split around B_{pole} . These resonances represent an Autler-Townes doublet. The solid lines (blue) are for large laser detuning $\Delta_L/\gamma_e = 5$ and $\hbar|\Omega_R|^2/\gamma_e\mu_{ag} = 100$ G. They also show two resonances, but their heights, widths, and distances from B_{pole} are quite different. The dashed line (black) is a reference without any light $\Omega_R = 0$.

which is a Breit-Wigner form [Bre36] as a function of Δ_L or B . The real and imaginary parts are

$$\text{Re}(a) = a_{\text{bg}} - \frac{m}{2\pi\hbar} \Delta_e \frac{|\beta|^2}{\Delta_e^2 + (\gamma_e/2)^2} \quad (5.14a)$$

$$K_2 = 2\gamma_e \frac{|\beta|^2}{\Delta_e^2 + (\gamma_e/2)^2}, \quad (5.14b)$$

which is identical to Eq. (10) in Ref. [Boh97] in the limit $\Gamma_{\text{stim}} \ll \Gamma_{\text{spon}}$.

5.2.3. Large Detuning

A good part of our experiments is performed in the limit of large laser detuning where $|\Delta_L| \gg |\mu_{ae}(B - B_{\text{pole}})/\hbar|$ and $|\Delta_L| \gg \gamma_e$ and with $\beta = 0$. From Eq. (5.7) we obtain a Breit-Wigner form

$$a = a_{\text{bg}} \left(1 - \frac{\Delta B}{B - B_{\text{res}} - iW/2} \right) \quad (5.15)$$

with ΔB from Eq. (5.12). The real and imaginary parts are a dispersive line shape and a Lorentzian, respectively,

$$\text{Re}(a) = a_{\text{bg}} \left(1 - \frac{\Delta B(B - B_{\text{res}})}{(B - B_{\text{res}})^2 + W^2/4} \right) \quad (5.16a)$$

$$K_2 = \frac{K_2^{\text{max}}}{1 + 4(B - B_{\text{res}})^2/W^2}. \quad (5.16b)$$

The resonance position B_{res} , the maximum loss rate coefficient K_2^{max} , and the full width at half maximum W of the Lorentzian are given by

$$K_2^{\text{max}} = \frac{\hbar}{\mu_{ag}} \frac{8|\alpha|^2}{W} \quad (5.17a)$$

$$W = \frac{\hbar}{\mu_{ag}} \frac{|\Omega_R|^2}{4\Delta_L^2} \gamma_e \quad (5.17b)$$

$$B_{\text{res}} = B_{\text{pole}} - \frac{\hbar}{\mu_{ag}} \frac{|\Omega_R|^2}{4\Delta_L}. \quad (5.17c)$$

The far-detuned bound-to-bound coupling yields the well-known ac-Stark shift of state $|g\rangle$ and this shifts B_{res} .

In general, it is possible that several excited states contribute noticeably to a . Our model is easily adapted to this situation by introducing a separate version of Eq. (5.3c) for each excited state and by including sums over the excited states in Eqs. (5.3a) and (5.3b). In the limit of large laser detuning and with $\beta = 0$ for each excited state, Eqs. (5.15)–(5.17a) remain unchanged and a sum over the excited states appears on the right hand side of Eqs. (5.17b) and (5.17c).

5.2.4. Autler-Townes Model

More insight into the physics of the problem can be gained from an Autler-Townes model [Aut55, CT92]. In addition, analytic expressions for the position, height and width of the resonances in $K_2(B)$ can be derived.

This approach is based on the assumption that the dominant frequencies in the problem are Ω_R and/or $(\Delta_g - \Delta_e)$. In this case, one can first diagonalize the driven two-level system spanned by $|g\rangle$ and $|e\rangle$ and subsequently treat the coupling to state $|a\rangle \otimes |a\rangle$ as a weak probe.

For the first step, we diagonalize the two-level system spanned by $|g\rangle$ and $|e\rangle$, setting $\alpha = \beta = \gamma_e = 0$. We assume without loss of generality that the relative phase between states $|g\rangle$ and $|e\rangle$ is chosen such that Ω_R is real. This yields energy eigenvalues and

eigenvectors

$$E_{\pm} = \frac{\hbar}{2}(\Delta_e + \Delta_g \pm \Omega_{\text{eff}}) \quad (5.18a)$$

$$|+\rangle = \cos \frac{\vartheta}{2}|e\rangle + \sin \frac{\vartheta}{2}|g\rangle \quad (5.18b)$$

$$|-\rangle = -\sin \frac{\vartheta}{2}|e\rangle + \cos \frac{\vartheta}{2}|g\rangle, \quad (5.18c)$$

where the effective Rabi angular frequency Ω_{eff} and the mixing angle ϑ are real-valued and must satisfy the implicit equations

$$\Omega_{\text{eff}} \cos \vartheta = \Delta_e - \Delta_g \quad (5.19a)$$

$$\Omega_{\text{eff}} \sin \vartheta = \Omega_R. \quad (5.19b)$$

This determines a unique value of ϑ modulo 2π and it yields

$$\Omega_{\text{eff}} = \sqrt{\Omega_R^2 + (\Delta_e - \Delta_g)^2}. \quad (5.20)$$

For the second step, we rewrite the mean-field model (5.3) in the new basis and obtain with $\beta = 0$

$$i \frac{d}{dt} \psi_a = \frac{U_{\text{bg}}}{\hbar} |\psi_a|^2 \psi_a + 2\psi_a^* (C_+^* \psi_+ + C_-^* \psi_-) \quad (5.21a)$$

$$i \frac{d}{dt} \psi_+ = C_+ \psi_a^2 + \left(\frac{E_+}{\hbar} - \frac{i}{2} \gamma_+ \right) \psi_+ - \frac{i}{2} \gamma_{\text{mix}} \psi_- \quad (5.21b)$$

$$i \frac{d}{dt} \psi_- = C_- \psi_a^2 - \frac{i}{2} \gamma_{\text{mix}} \psi_+ + \left(\frac{E_-}{\hbar} - \frac{i}{2} \gamma_- \right) \psi_- \quad (5.21c)$$

with $C_+ = \alpha \sin \frac{\vartheta}{2}$, $C_- = \alpha \cos \frac{\vartheta}{2}$, $\gamma_+ = \gamma_e \cos^2 \frac{\vartheta}{2}$, $\gamma_- = \gamma_e \sin^2 \frac{\vartheta}{2}$, and $\gamma_{\text{mix}} = -\gamma_e \sin \frac{\vartheta}{2} \cos \frac{\vartheta}{2}$. So far we only rotated the basis and the model is still exact. We now approximate the loss as being diagonal in the states $|+\rangle$ and $|-\rangle$ by setting $\gamma_{\text{mix}} = 0$. Adiabatic elimination of the populations in states $|+\rangle$ and $|-\rangle$ then yields

$$a = a_{\text{bg}} + a_+ + a_-, \quad (5.22)$$

where the states $|+\rangle$ and $|-\rangle$ each contribute a Breit-Wigner form as a function of E_{\pm}

$$a_{\pm} = -\frac{m}{2\pi\hbar} \frac{|C_{\pm}|^2}{E_{\pm}/\hbar - i\gamma_{\pm}/2}. \quad (5.23)$$

Thus, the states $|+\rangle$ and $|-\rangle$ each cause a single resonance and their contributions to a are simply added. This corresponds to the intuitive understanding of an Autler-Townes doublet [CT92].

The above approximation $\gamma_{\text{mix}} = 0$ is self-consistent if the system is close to one resonance and the resonances are well separated ($\gamma_e \ll \Omega_{\text{eff}}$), because in this case the states $|\pm\rangle$

have very different populations, so that a possible coherence between these populations has little effect and γ_{mix} is negligible.

If the resonances are narrow and well separated, then $K_2(B)$ becomes a Lorentzian and the maxima of $K_2(B)$ will then occur at the magnetic fields [Bau09a]

$$B_{\text{res}} = B_{\text{pole}} + \frac{\hbar}{2\mu_{ae}} \left(\Delta_L \pm \sqrt{\Delta_L^2 + \frac{\mu_{ae}}{\mu_{ag}} \Omega_R^2} \right). \quad (5.24)$$

The values of K_2 at these maxima are [Bau09a]

$$K_2^{\text{max}} = \frac{8|\alpha|^2}{\gamma_e} \frac{\mu_{ae}}{\mu_{ag}} \left(1 - \frac{2\Delta_L}{\Delta_L \pm \sqrt{\Delta_L^2 + \frac{\mu_{ae}}{\mu_{ag}} \Omega_R^2}} \right). \quad (5.25)$$

The full width at half maximum of the Lorentzian $K_2(B)$ is given by [Bau09a]

$$W = \frac{\hbar\gamma_e}{2\mu_{ae}} \left(1 \pm \frac{\Delta_L}{\sqrt{\Delta_L^2 + \frac{\mu_{ae}}{\mu_{ag}} \Omega_R^2}} \right). \quad (5.26)$$

We will compare these results with experimental data in Sec. 5.4.

5.3. Laser Spectroscopy

The scheme described in Sec. 5.2 requires an appropriate excited molecular state $|e\rangle$. A state is particularly well suited, if it offers a strong coupling for the bound-to-bound transition and weak or even negligible coupling for the photoassociation transition. To find such a state $|e\rangle$ we perform laser spectroscopy.

The starting point for all experiments in this chapter is an essentially pure BEC of ^{87}Rb atoms in the hyperfine state $|F, m_F\rangle = |1, 1\rangle$ close to the Feshbach resonance at 1007 G, except for the spectrum in Fig. 5.3(a), where we used a BEC of atoms in the states $|F, m_F\rangle = |1, -1\rangle$ at $B \simeq 1$ G. We use a Feshbach resonance that is characterized by the parameters [Mar02, Dür04b, Dür04a, Vol03] $B_{\text{pole}} = 1007.4$ G, $\Delta B = 0.21$ G, $\mu_a/2\pi\hbar = 1.02$ MHz/G, $\mu_{ag}/2\pi\hbar = 3.8$ MHz/G, and $a_{\text{bg}} = 100.5a_0$, where a_0 is the Bohr radius. With these parameters Eq. (5.12) yields $|\alpha|/2\pi = 1.8$ mHz cm $^{3/2}$. The peak density of the BEC is typically $n = |\psi_a|^2 \sim 2 \times 10^{14}$ cm $^{-3}$. The quantity $|\sqrt{8}\alpha\psi_a| = 2\pi \times 0.07$ MHz can be regarded as a Rabi angular frequency. For typical parameters of our experiment, this value is small compared to γ_e and $|\Omega_R|$, so that the adiabatic elimination performed in Sec. 5.2.2 is justified. The atoms are held in a crossed-beam optical dipole trap with both beams operated at 1064 nm and with trap frequencies of $(\omega_x, \omega_y, \omega_z)/2\pi = (74, 33, 33)$ Hz, see Sec. 3.3. The magnetic field B points along the z axis and is held several Gauss away from the Feshbach resonance.

For the excited-state spectroscopy, we use two techniques which complement each other. The first technique is ordinary photoassociation spectroscopy. For this, we simply illuminate the BEC with photoassociation light. The light intensity is slowly increased within

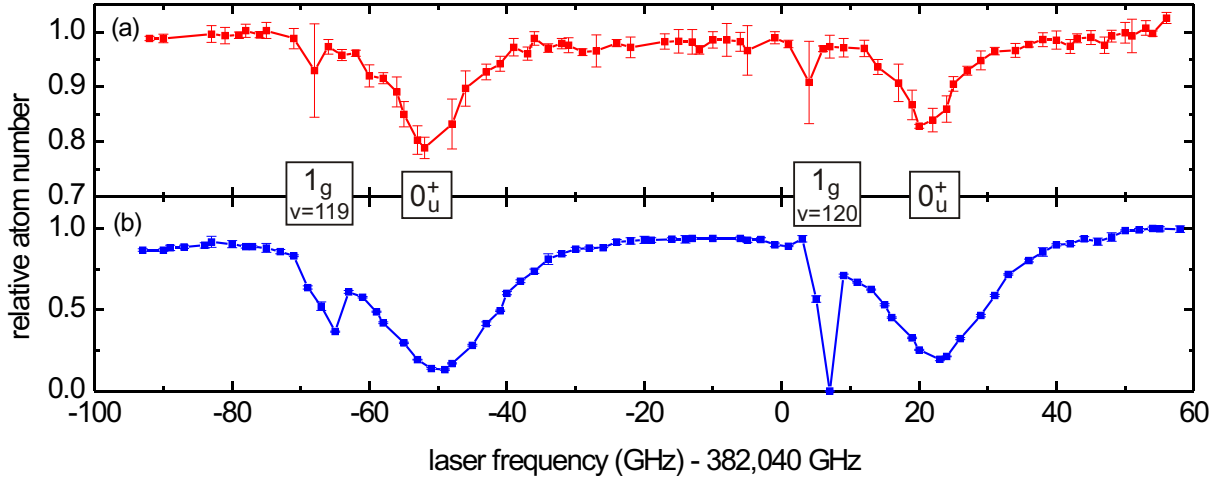


Figure 5.3.: Photoassociation spectroscopy for ^{87}Rb . The spectra are taken (a) for atoms in state $|F = 1, m_F = -1\rangle$ at $B \simeq 1$ G and (b) for atoms in state $|F = 1, m_F = +1\rangle$ at $B = 1006$ G. The two narrow resonances are related to bound states in the 1_g potential with vibrational quantum numbers $v = 119$ and $v = 120$. The two broad resonances are probably caused by bound states in the 0_u^+ potential [Jon06, Kem04, Tsa08].

80 ms to a final power of ~ 10 mW and held there for 100 ms. Next, the photoassociation light, B , and the dipole trap are switched off simultaneously. Finally, the remaining atom number is extracted from a time-of-flight image.

The photoassociation light is implemented as a traveling-wave laser beam with a waist ($1/e^2$ radius of intensity) of $w = 0.17$ mm and a wavelength of ~ 784.7 nm. In order to address as many excited states as possible in the spectroscopy measurements, we let the photoassociation beam propagate along the vertical x axis and choose a specific linear polarization which corresponds to $1/3$ of the intensity in each of the polarizations π , σ^+ , and σ^- . As the population is initially in the atomic state $|a\rangle$, the loss signal is typically dominated by photoassociation processes so that the technique is particularly sensitive to excited states that have a large value of the photoassociation coupling strength β .

For coarse orientation, we perform spectroscopy covering a frequency range of ~ 160 GHz with moderate frequency resolution. Fig. 5.3(a) shows data taken at a magnetic field of ~ 1 G with the atoms in state $|F = 1, m_F = -1\rangle$. Fig. 5.3(b) was recorded at a magnetic field of 1006 G with the atoms in state $|F = 1, m_F = +1\rangle$.

Three attractive potentials could in principle contribute to the photoassociation signal in the frequency range studied here, which lies ~ 2 THz below the $^2P_{3/2} + ^2S_{1/2}$ threshold. All three potentials are adiabatically connected to the $^2P_{3/2} + ^2S_{1/2}$ threshold. They are characterized by the quantum numbers 0_u^+ , 1_g , and 2_u [Kem04, Jon06]. A comparison with photoassociation data at $B \simeq 0$ G from the Heinzen group [Tsa08] shows that two of the observed resonances are related to bound states in the 1_g potential with vibrational quantum numbers $v = 119$ and $v = 120$. The same comparison suggests that the two other observed resonances are caused by bound states in the 0_u^+ potential. The potential 2_u does not seem to contribute any noticeable signal in Fig. 5.3. Each observed vibrational level

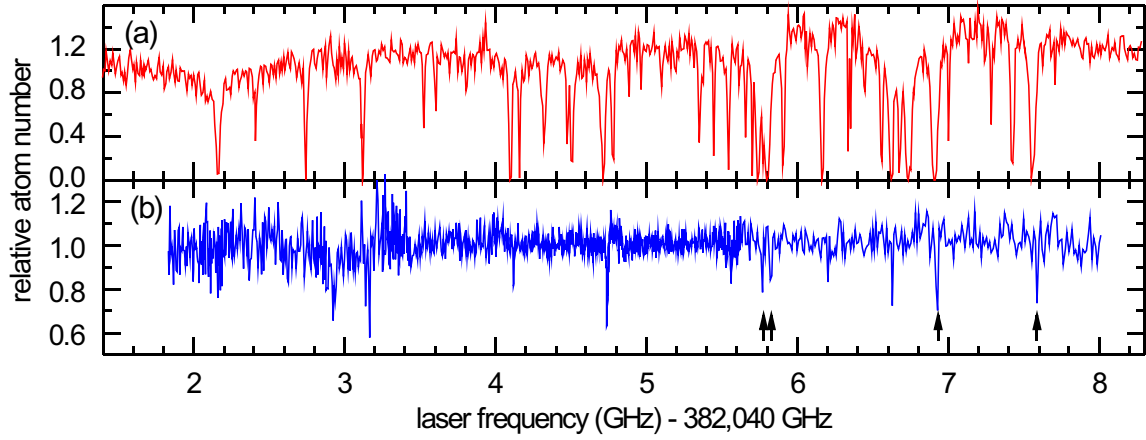


Figure 5.4.: Excited-state spectroscopy for ^{87}Rb . (a) Photoassociation spectrum taken at $B = 1000.0$ G. (b) Bound-to-bound spectrum taken at $B = 1000.0$ G. Arrows indicate the resonances characterized in Tab. 5.1.

is expected to display hyperfine splitting, which is unresolved in Fig. 5.3. The hyperfine splitting of the $^2P_{3/2} + ^2S_{1/2}$ threshold is approximately the atomic ground-state hyperfine splitting of ~ 6.8 GHz because this threshold involves one ground state atom and one excited state atom and the atomic excited-state hyperfine splitting is much smaller. This explains the observed widths of the resonance lines in Fig. 5.3 within a factor ~ 2 .

The reaction of the photoassociation lines to a magnetic field of 1006 G can be estimated as follows: This magnetic field shifts the energy of the ground state $|F = 1, m_F = +1\rangle$ by $-2\pi\hbar \times 0.88$ GHz [see Appendix, Eq. (A.6)], whereas the barycenter of each excited-state hyperfine manifold is expected to be unshifted. Hence, the barycenters of the photoassociation lines are estimated to be shifted by $\sim +1.76$ GHz with respect to the spectrum at 1 G. The Bohr magneton probably sets a reasonable upper bound for the magnetic moment of the excited state so that application of the magnetic field is expected to broaden each manifold by at most 2.8 GHz. These estimates are confirmed by the spectrum at 1006 G, as shown in Fig. 5.3(b). All loss features in 5.3(b) are pretty deep. This is likely to result in an additional broadening of the observed loss features. It remains unclear why the loss features at 1006 G are deeper than the ones at 1 G.

The resonance at $\sim 382,045$ GHz ($1_g, v = 120$) is used in all our following experiments. It is shown with much better frequency resolution in Fig. 5.4(a). This measurement resolves the hyperfine and Zeeman substructure of this vibrational level. A method for the assignment of a complete set of quantum numbers to such a hyperfine manifold at ~ 0 G was presented recently in Ref. [Ham09].

We extended the frequency scan in Fig. 5.4(a) down to 382,037.3 GHz but did not find any further loss resonances. We determined the corresponding zero-field frequencies by performing a similar measurement at $B \sim 0$. We took data between 382,034 GHz and 382,051 GHz and found photoassociation loss resonances in the range between 382,041.8

Polarization	$\omega_{eg}/2\pi$ (MHz)	$ d_{eg} /ea_0$	$\gamma_e/2\pi$ (MHz)	$\mu_{ae}/2\pi\hbar$ (MHz/G)
σ^-	382,045,759.4(3)	0.24(5)	4.4(5)	2.2(1)
σ^+	382,045,818.2(3)	0.29(5)	4.7(5)	1.7(1)
π	382,046,942.8(3)	0.28(5)	4.7(5)	2.6(1)
π	382,047,581.8(3)	0.18(5)	5.3(5)	2.7(1)

Table 5.1.: Parameters of four selected bound-to-bound resonances. e is the elementary charge, a_0 the Bohr radius. β is negligible for all these resonances.

GHz and 382,044.5 GHz.

Since our technique for shifting a Feshbach resonance with laser light relies on a bound-to-bound transition, not on photoassociation, we developed a second spectroscopy technique that is particularly sensitive to excited states with a large value of Ω_R . The basic idea is to first use the Feshbach resonance to associate molecules into state $|g\rangle$ and then illuminate them with light that resonantly drives bound-to-bound transitions. We call this the bound-to-bound light and employ the same laser beam previously used for the photoassociation spectroscopy.

In order to avoid loss of particles due to inelastic collisions between molecules, the atoms must be loaded into a deep optical lattice before associating the molecules [Tha06]. As in Sec. 4.1, we prepare a state, which contains exactly one molecule at each lattice site in the central region of the lattice. This core is surrounded by a shell of sites that contain exactly one atom each. After loading the lattice, the laser power of one of the dipole trapping beams is ramped to zero, as in Ref. [Vol06].

Next, the bound-to-bound light is turned on for 0.2 ms at a power of $\sim 0.1 \mu\text{W}$. This light has the same linear polarization as for the photoassociation spectroscopy. If a molecule in state $|g\rangle$ is excited on a bound-to-bound transition, then it is likely to undergo spontaneous radiative decay into a different internal state. After turning off the bound-to-bound light, the magnetic field is ramped back across the Feshbach resonance to dissociate the molecules that remained in state $|g\rangle$. Subsequently, the optical dipole trap at 1064 nm is turned back on, the lattice depth is slowly ramped to zero, the cloud is released, B is switched off, and the atom number is determined from a time-of-flight image. Molecules that were excited by the laser are not dissociated and thus not detected.

A bound-to-bound spectrum measured at $B = 1000.0$ G is shown in Fig. 5.4(b). Comparison with the photoassociation spectrum in part (a) shows that many of the excited states are visible with both techniques. But identifying promising candidates with large Ω_R is not easily possible from part (a). The light frequency calibration for both spectra has a precision of ~ 30 MHz and can fluctuate within a single scan. This causes deviations in the resonance positions between the photoassociation spectrum and the bound-to-bound spectrum. In addition, the states $|a\rangle$ and $|g\rangle$ are degenerate at $B = 1007.4$ G. At $B = 1000.0$ G, the internal energies of a molecule in state $|g\rangle$ and a pair of atoms in state $|a\rangle$ differ by $2\pi\hbar \times 20$ MHz [Dür04a]. In Fig. 5.4 this yields a 20-MHz shift of all bound-to-bound resonances with respect to the photoassociation resonances.

Very different values of the light intensity and the illumination time were used when recording the two spectra. This tremendous difference in the sensitivity of the two methods is a result of Eq. (5.5).

5.4. Autler-Townes Splitting of a Magnetic Feshbach Resonance

To determine all parameters of a specific bound-to-bound resonance, we study the regime of much smaller detuning of the laser light. In this regime, we observe an Autler-Townes doublet as a function of B . Fitting the model of Sec. 5.2.4 to the data of one of the bound-to-bound resonances, allows us to extract all parameters of this resonance.

5.4.1. Observation of an Autler-Townes Doublet

The experimental sequence is as follows: We start with a BEC of ^{87}Rb atoms in the hyperfine state $|F = 1, m_F = 1\rangle$ in an optical dipole trap with trap frequencies $(\omega_x, \omega_y, \omega_z)/2\pi = (74, 33, 33)$ Hz. The magnetic field B is held at a value that is a few Gauss away from the Feshbach resonance at 1007.4 G. At time $t = 0$, B is jumped to a certain value at which it is held for 2 ms. During the 2 ms hold time of B , the bound-to-bound light is applied at a power of 0.47 mW. After the 2 ms hold time of B , the bound-to-bound light, the optical dipole trap, and B are switched off simultaneously. This is followed by free flight and the atom cloud is imaged 18 ms after release from the dipole trap.

The evolution of the cloud size during this sequence can be modeled in analogy to Refs. [Cas96, Vol03] as follows. Initially, the density distribution $n(\vec{r})$ of the BEC inside the optical dipole trap is described by a Thomas-Fermi parabola

$$n(\vec{r}) = n_{\text{peak}} \left[1 - \sum_{k=1}^3 \left(\frac{r_k}{W_k} \right) \right], \quad (5.27)$$

and $n(\vec{r}) = 0$ if the above expression is negative. n_{peak} is the peak intensity. The Thomas-Fermi radii along the coordinate axes r_k are

$$W_k(0) = \frac{1}{\omega_k} \left(15 \frac{\hbar^2}{m^2} \omega_x \omega_y \omega_z a(0) N(0) \right)^{1/5}, \quad (5.28)$$

where $N(0)$ is the initial atom number in the BEC, and the initial scattering length $a(0)$ equals a_{bg} . At $t = 0$, B is changed to its final value and the bound-to-bound light is applied. The system is allowed to evolve under these conditions for 2 ms. During this hold time, $a(t)$ and $N(t)$ may be time dependent. The model is based on the assumption that the BEC profile remains a Thomas-Fermi parabola at all times. Its Thomas-Fermi radii are scaled by the dimensionless parameters

$$\lambda_k(t) = \frac{W_k(t)}{W_k(0)}. \quad (5.29)$$

The evolution of the scaling parameters $\lambda_k(t)$ can be calculated following the model in Ref. [Cas96]. Eq. (11) from Ref. [Cas96] reads

$$\ddot{\lambda}_j = \frac{1}{\lambda_x \lambda_y \lambda_z} \frac{\omega_j^2(0)}{\lambda_j} - \omega_j^2(t) \lambda_j \quad (5.30)$$

with $j \in \{1, 2, 3\}$, where $\omega_j(t)$ are the time-dependent trap angular frequencies. The first term describes the outward force caused by the mean-field energy, the second term represents the harmonic confinement. The initial condition is a BEC in equilibrium in a trap at time $t = 0$, corresponding to $\lambda_j(0) = 1$ and $\dot{\lambda}_j(0) = 0$. Following Ref. [Vol03], we include the possibility that the scattering length a and the particle number N are time dependent

$$\ddot{\lambda}_j = \frac{N(t) \operatorname{Re}[a(t)]}{N(0) \operatorname{Re}[a(0)]} \frac{1}{\lambda_x \lambda_y \lambda_z} \frac{\omega_j^2(0)}{\lambda_j} - \omega_j^2(t) \lambda_j. \quad (5.31)$$

The additional factor represents the fact that the mean-field energy is proportional to $N(t) \operatorname{Re}[a(t)]$. Here, the approximation that the cloud shape remains a Thomas-Fermi parabola is assumed to be valid even in the presence of loss.

If the loss is due to inelastic two-body collisions, then the evolution of the atomic density $n(t)$ is governed by Eq. (5.9). In a BEC $g^{(2)} \sim 1$ and spatial integration of Eq. (5.9a) for a Thomas-Fermi parabola yields

$$\dot{N} = -\frac{4}{7} K_2(t) n_{\text{peak}}(t) N(t), \quad (5.32)$$

with the time-dependent peak density

$$n_{\text{peak}}(t) = \frac{15N(t)}{8\pi W_x(t) W_y(t) W_z(t)}. \quad (5.33)$$

Hence,

$$\dot{N} = -\frac{4}{7} K_2(t) \frac{n_{\text{peak}}(0)}{N(0)} \frac{N^2(t)}{\lambda_x(t) \lambda_y(t) \lambda_z(t)}. \quad (5.34)$$

For our experimental sequence, the scattering length is given by

$$a(t) = \begin{cases} a & : 0 < t \leq 2\text{ms} \\ a_{\text{bg}} & : \text{otherwise} \end{cases}, \quad (5.35)$$

where a_{bg} is real, but a might be complex. Eqs. (5.31) and (5.34) form a set of coupled differential equations. This model is used to extract $\operatorname{Re}(a)$ and K_2 [see Eq. (5.9b)] from the measured atom number and cloud size after expansion¹.

Experimental results are shown in Fig. 5.5. We clearly observe an Autler-Townes doublet in $K_2(B)$. We fit Eq. (5.10) to all the data in this figure simultaneously. The fit agrees well with the experimental data.

¹For a given pair of measured values of $\lambda_j(t)$ and $N(t)$ there is usually more than one possible pair of values for $\operatorname{Re}(a)$ and $\operatorname{Im}(a)$. But the fact that $a(B)$ is continuous (except at the pole) is usually sufficient to single out the physical solution.

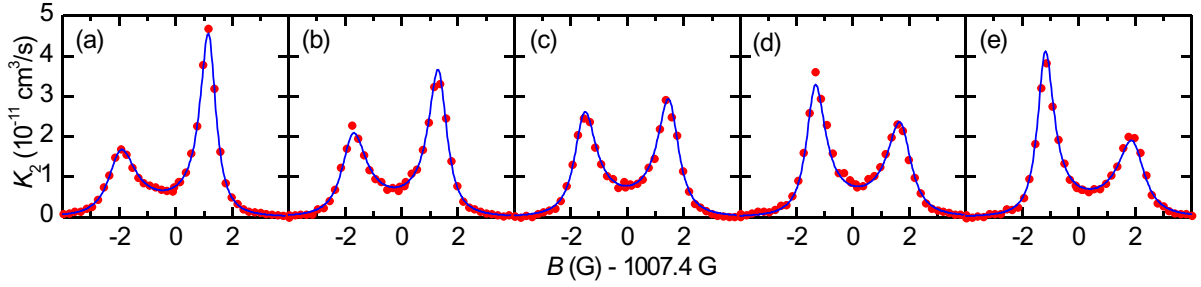


Figure 5.5.: Autler-Townes splitting of a magnetic Feshbach resonance caused by application of a laser that drives a bound-to-bound transition with a power of $P = 0.47$ mW. The loss rate coefficient K_2 is measured as a function of magnetic field B for different values of the laser frequency, that increase from (a) to (e) in steps of 1 MHz. Part (c) is recorded at 382,046,942.62 MHz very close to resonance, where the Autler-Townes doublet becomes symmetric. The lines show a simultaneous fit to all these data sets.

We apply this method to four reasonably strong bound-to-bound resonances which are fairly close to the high-frequency end of the spectrum in Fig. 5.4 (indicated by arrows). The best-fit values for the parameters of these resonances are listed in Tab. 5.1. The laser producing the bound-to-bound light was beat-locked to a frequency comb, resulting in a much better precision of the frequency calibration (see Sec. 3.4.2). The polarization of each resonance was determined from a series of measurements in which the bound-to-bound light had only one of the polarizations π , σ^+ , or σ^- . The latter two polarizations were implemented with the bound-to-bound beam propagating along the z axis. Each resonance in Tab. 5.1 responded to only one of these polarizations.

5.4.2. Laser Frequency and Laser Power Dependence

We can also determine the position of the two loss resonances associated with the Autler-Townes doublet systematically as a function of laser frequency and laser power, as shown in Fig. 5.6. The data exhibit typical features of an Autler-Townes doublet, namely an avoided level crossing in (a) and a splitting approximately proportional to the square root of the laser power in (b). The data are well described both by the full model [Eq. (5.10)] and by the Autler-Townes model [Eq. (5.24)].

Finally, we compare the theoretical results for the height and the width of the Autler-Townes resonances in $K_2(B)$ from Sec. 5.2.4 with experimental results. We measured Autler-Townes doublets in $K_2(B)$, as shown in Fig. 5.5(b). We fit a Lorentzian (5.16b) to each of the two peaks in the experimental data. The best-fit values for K_2^{\max} and W are shown in Fig. 5.7. The dotted lines show the corresponding predictions (5.25) and (5.26).

For comparison, we numerically determined the peaks in $K_2(B)$ from the full model (5.10) with the parameters of Tab. 5.1. The corresponding maximum values K_2^{\max} are shown as solid lines in Fig. 5.7(a). As the full model (5.10) does not predict Lorentzian lines, a direct comparison with the width W is not straightforward. We decide to use the second derivative of $K_2(B)$ at the maximum for a comparison. The solid lines in

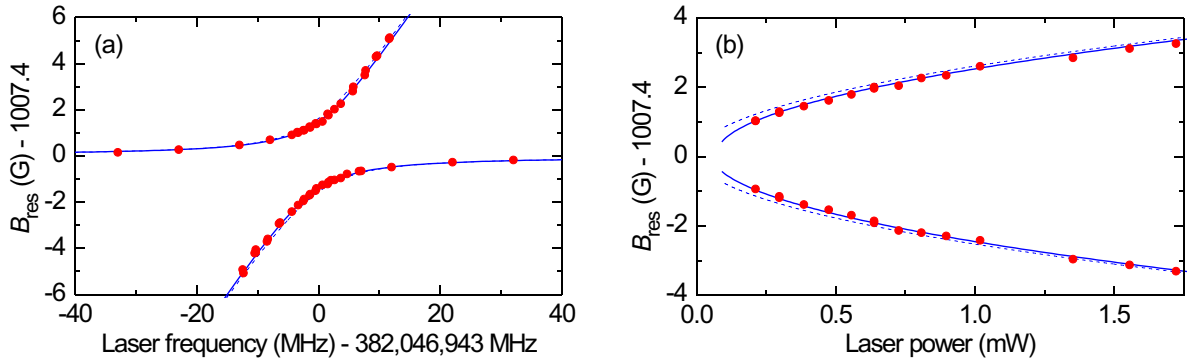


Figure 5.6.: Systematic study of the resonance positions associated with the Autler-Townes doublet. The magnetic fields at which the loss resonances occur are shown as a function of laser frequency (a) and laser power (b). Part (a) was recorded at a power of 0.47 mW and clearly shows an avoided level crossing. Part (b) was recorded at a laser frequency of 382,046,943.00 MHz. The solid [dashed] lines show the prediction of the full model Eq. (5.10) [Autler-Townes model Eq. (5.24)] with the parameter values from Tab. 5.1.

Fig. 5.7(b) therefore show the values of

$$W = \left(-\frac{1}{8K_2} \frac{d^2 K_2}{dB^2} \right)^{-1/2} \quad (5.36)$$

at the peaks calculated from the full model (5.10). If the peaks in the model were Lorentzian, this would yield the width W . The solid lines also agree well with the experimental data and with the dotted lines.

5.5. Shifting a Magnetic Feshbach Resonance with Laser Light

We now use the spectroscopic information from Sec. 5.3 and the parameters gathered in Sec. 5.4 to shift the Feshbach resonance with far-detuned light. As in most applications of ac-Stark shifts, we wish to achieve a certain value of $|\Omega_R|^2/\Delta_L$ and at the same time keep the rates for incoherent processes as low as possible. Hence, it is advantageous to increase the detuning and power of the laser in a way that keeps $|\Omega_R|^2/\Delta_L$ constant. This yields $W \rightarrow 0$ and $K_2(B) \rightarrow (4\pi\hbar|\alpha|^2/\mu_{ag})\delta(B - B_{\text{res}})$, where δ denotes the Dirac delta function (see Sec. 5.2.3). For any given value of $B \neq B_{\text{res}}$ one can thus decrease $K_2(B)$ by increasing the detuning and the laser power sufficiently far.

The experimental sequence of this section is the same as in Sec. 5.4.1 with the only difference that here the optical dipole trap is switched off at $t = 0$ ms. The experimental data in Fig. 5.8 were recorded in a regime where the detuning of the light from the bound-to-bound resonance is much larger than the natural line width of state $|e\rangle$ and much larger than the energy width of the Feshbach resonance, as discussed in Sec. 5.2.3. In this regime,

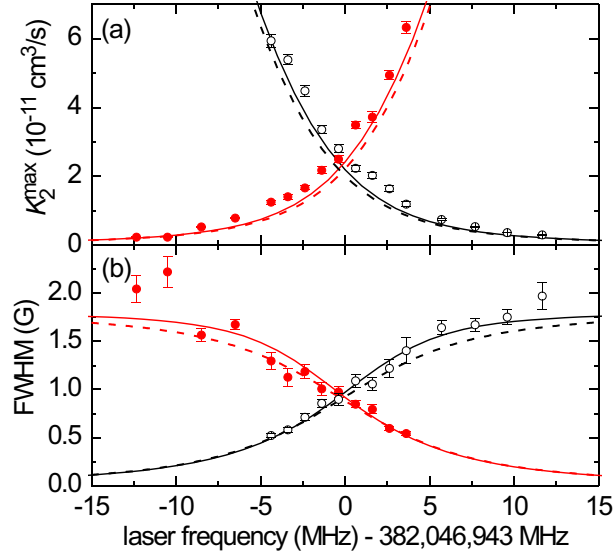


Figure 5.7.: Systematic study of the loss resonances. $K_2(B)$ was measured for certain values of the laser frequency at a fixed laser power of 0.47 mW. (a) The maximum K_2^{\max} and (b) the width W were determined from a fit to Eq. (5.16b). The experimental data for the resonances that occur at the lower (\circ) and higher (\bullet) value of B both agree well with the predictions of the full model Eq. (5.10) (solid lines) which is well approximated by Eqs. (5.25) and (5.26) of the Autler-Townes model (dashed lines).

the light causes an ac-Stark shift of state $|g\rangle$, which results in a corresponding shift of the magnetic field at which the Feshbach resonance occurs. For the data in Fig. 5.8 we choose the bound-to-bound transition resonance at 382,046,942.8 MHz, which is sensitive to π polarized light (see Tab. 5.1). Fig. 5.8(a) shows $\text{Re}(a)$ as a function of B for a laser detuning of +107 MHz and -107 MHz. The corresponding shifts which amount to $\sim \pm 0.5$ G are clearly visible. The solid lines are fits of Eq. (5.11) to the data.

Fig. 5.8(b) shows the corresponding two-body loss rate coefficient K_2 for a BEC. The solid lines are the predictions for K_2 , see Eq. (5.16b). In the absence of light, K_2 is zero. With the light on, we attribute all observed particle loss to K_2 . This overestimates K_2 on the low-field side of the resonance, where part of the loss is actually caused by inelastic three-body collisions [Smi07]. On the high-field side of the resonance, the three-body loss is less important [Vol03] and the extracted values for K_2 for blue detuning (\blacksquare) agree well with the solid line. The agreement for red detuning (\bullet) is not quite as good.

In order to compare with an optical Feshbach resonance, we consider the data points in Fig. 5.8(a) with $\text{Re}(a)/a_{\text{bg}} - 1 \sim \pm 1$. For these data points Fig. 5.8(b) shows $K_2 \sim 10^{-11} \text{ cm}^3/\text{s}$, which is an improvement by one order of magnitude compared to Refs. [The04, Tha05].

For any given value of $B \neq B_{\text{res}}$ in Fig. 5.8, the two-body losses can be reduced even further than by increasing the laser detuning and the laser power much further. When following this approach, two new issues have to be addressed.

First, the detunings are no longer small compared to the typical splitting between

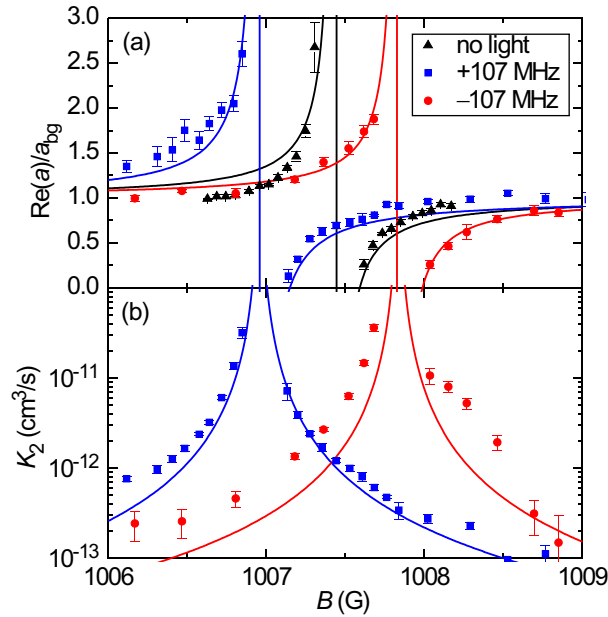


Figure 5.8.: Shifting a Feshbach resonance with laser light. (a) Real part of the scattering length as a function of magnetic field. In the absence of light (\blacktriangle), the pole in the scattering length occurs at 1007.4 G. With 4.2 mW of light applied the Feshbach resonance is shifted to a different magnetic field. The data were recorded at a detuning of the light frequency with respect to the bound-to-bound resonance of $\Delta_L/2\pi = +107$ MHz (\blacksquare) and -107 MHz (\bullet). The resonance frequency of the nearest bound-to-bound transition is 382,046,943 MHz. (b) The application of the light induces two-body loss described by the rate coefficient K_2 for a BEC. The observed loss when changing $\text{Re}(a)/a_{\text{bg}}$ by ± 1 is typically one order of magnitude lower than the loss that would be incurred when using an optical Feshbach resonance.

the various hyperfine and magnetic substates of the excited state. Achieving a large detuning with respect to all excited states thus requires knowledge of the positions of all nearby excited states, so that the excited-state spectroscopy data of Sec. 5.3 comes into play. In order to achieve a large detuning from all excited states, the light must be detuned either to the left or to the right of the complete multiplet in Fig. 5.4. The three outermost resonances at the low-frequency end of the spectrum in Fig. 5.4 have fairly strong photoassociation loss features, but show hardly any bound-to-bound features, which is unfortunate. The high-frequency end of the spectrum looks more promising. We therefore perform all the following experiments at the high-frequency end of the spectrum in Fig. 5.4. According to Tab. 5.1, the two strongest bound-to-bound resonances near this end of the spectrum both respond to π polarized light. Hence, we choose π polarization for the bound-to-bound light in all the following experiments.

Second, if the laser that drives the bound-to-bound transition is now operated at much larger power, then it creates a noticeable dipole trap. Its rapid turn-on induces large-amplitude oscillations of the cloud size which are difficult to model. We therefore explore an alternative way of measuring $\text{Re}(a)$ and K_2 . To this end, we pin the positions of the

atoms with a deep optical lattice which minimizes the effect of the additional dipole trap. In the lattice, we use excitation spectroscopy and a loss measurement to determine $\text{Re}(a)$ and K_2 , respectively.

In order to measure $\text{Re}(a)$, we first load the atoms into the lattice as described in Sec. 5.3. We then use excitation spectroscopy [Stö04] in the lattice, *i.e.*, we modulate the power of one retro-reflected lattice beam sinusoidally as a function of time around an average lattice depth of $V_0 \sim 15E_{rec}$. The modulation amplitude is $\sim 4E_{rec}$. The modulation lasts for 10 or 20 ms. During the modulation, the atoms are illuminated with the bound-to-bound light and B is held at a specific value close to the Feshbach resonance. The bound-to-bound light is on for a long enough time that sites containing two or more atoms are essentially emptied by light-induced inelastic collisions. The signal in the excitation spectrum that is sensitive to the modulation frequency thus stems from sites that were initially populated by one atom. For certain modulation frequencies, tunneling of an atom between two such sites is resonantly enhanced. This leads to a frequency-dependent loss of atoms and of atomic phase coherence. At the end of the modulation, we switch the bound-to-bound light off and simultaneously jump B back to a value several Gauss away from the Feshbach resonance. Next, the dipole trap at 1064 nm is turned back on and the lattice depth is slowly reduced to $V_0 \sim 6E_{rec}$, where the gas is superfluid, thus restoring phase coherence between neighboring lattice sites. Finally, the dipole trap, B , and the lattice are simultaneously switched off. The time-of-flight image shows satellite peaks due to the restored phase coherence, as discussed in Sec. 4.1.

The visibility [Ger05] of the satellite peaks displays a minimum at a modulation frequency where tunneling processes between two initially singly occupied sites are resonant. This minimum is located at a frequency $f = \text{Re}(U)/2\pi\hbar$ with the on-site interaction matrix-element $U = g \int d^3x |w(\mathbf{x})|^4$, where $g = 4\pi\hbar^2 a/m$ and w is a tight-binding Wannier function, see Sec. 2.2.1. The measurement of f thus yields $\text{Re}(a)$.

A sequence of such measurements for various values of B yields Fig. 5.9(a). For parameters where $\text{Re}(a)$ is reduced drastically, the system becomes superfluid and the peak in the excitation spectrum is smeared out so much that its center cannot be determined any more. Hence, this method is not applicable in this regime. For comparison, the figure also shows $\text{Re}(a)$ measured with the same method, but in the absence of bound-to-bound light. Clearly, the position B_{res} of the Feshbach resonance is shifted by ~ -0.35 G due to the presence of the light.

We now turn to the question, how large a loss-rate coefficient K_2 is associated with this shift. In order to determine K_2 , we load the atoms into the lattice and associate molecules as described in Sec. 5.3. Right after association, we dissociate the molecules. This association-dissociation sequence serves the purpose of emptying all sites that contain three or more atoms, which will become important below. The lattice depth is $V_0 \sim 20E_{rec}$ so that tunneling is negligible. We then switch on the bound-to-bound light and simultaneously jump B to a value close to the Feshbach resonance. These conditions are maintained for a variable hold time. During this hold time, the bound-to-bound light causes rapid loss of atoms in doubly occupied sites. Next, B is switched to a value several Gauss away from the Feshbach resonance and the bound-to-bound light is switched off.

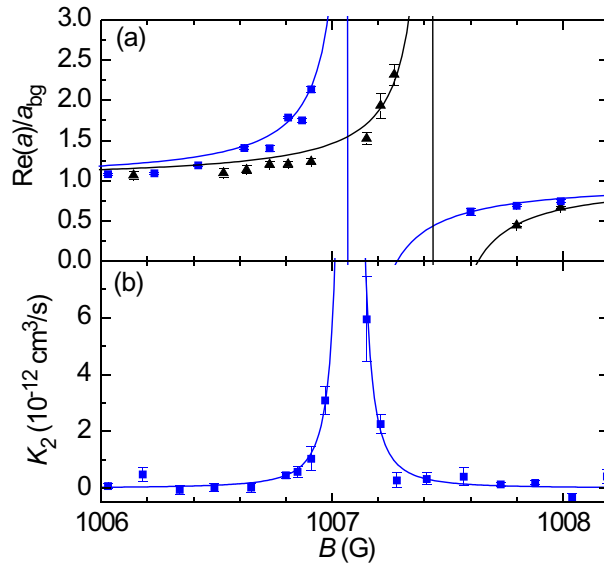


Figure 5.9.: Further reduction of the two-body losses. (a) Elastic and (b) inelastic two-body scattering properties are shown as a function of magnetic field B . Experimental data in the presence (\bullet) and absence (\blacksquare) of the light are compared. The light power is 11.2 mW and the frequency is $\omega_L/2\pi = 382,048,158$ MHz, which is 576 MHz blue detuned from the nearest bound-to-bound transition. The solid lines in (a) and (b) show fits of Eqs. (5.11) and (5.16b), respectively, to the data. The Feshbach resonance is shifted by ~ -0.35 G. At $B = 1006.91$ G, we measure $\text{Re}(a)/a_{\text{bg}} - 1 \sim 1$ and $K_2 \sim 1 \times 10^{-12}$ cm³/s which is two orders of magnitude less than for an optical Feshbach resonance [The04, Tha05].

The dipole trap light at 1064 nm is turned back on and the lattice depth is slowly lowered to zero. Finally, the cloud is released and B is switched off. The remaining number of atoms is extracted from a time-of-flight image.

To describe the two-body loss during the hold time, we use the master equation of Ref. [Sya08b]. We consider a lattice site initially occupied by exactly two atoms and we neglect tunneling between sites. The master equation then yields the density matrix $\rho = p|2\rangle\langle 2| + (1-p)|0\rangle\langle 0|$, where $p = \exp(-\Gamma t)$ is the probability that a decay at this site occurred and $|n\rangle$ denotes a Fock state with n atoms. The parameter Γ is given by [Sya08b]²

$$\Gamma = K_2 \int d^3x |w(\mathbf{x})|^4. \quad (5.37)$$

The decay of the total atom number N in the experiment is obtained by taking the sum over a large number of isolated lattice sites, yielding

$$N(t) = N_1 + N_2 \exp(-\Gamma t), \quad (5.38)$$

²Here we use a and K_2 from Eqs. (5.7) and (5.10). We derived these equations assuming that the sample is Bose condensed which is not the case in a deep optical lattice. But a and K_2 express only properties of two-body scattering processes. They are unaffected by the many-body state of the system.

where N_1 and N_2 are the initial atom numbers on singly and doubly occupied sites, respectively. It is crucial that there are no sites with three or more atoms, because they would give rise to an additional term that would decay more rapidly, thus making it more difficult to extract Γ from the measured $N(t)$.

We measured $N(t)$ at a fixed hold time $t = 2.1$ ms for various values of B and used Eqs. (5.37) and (5.38) to extract $K_2(B)$. Results are shown in Fig. 5.9(b). At $B = 1006.91$ G, we measure $\text{Re}(a)/a_{\text{bg}} - 1 \sim 1$ and $K_2 \sim 1 \times 10^{-12}$ cm³/s, which is one order of magnitude lower than in Fig. 5.8(b) and two orders of magnitude lower than the corresponding result reported for photoassociation resonances in ⁸⁷Rb [The04, Tha05].

We use the results of Sec. 5.2.3 to calculate the theoretical expectations from the sum of the two π resonances in Tab. 5.1. We thus expect $B_{\text{res}} - B_{\text{pole}} = -0.24$ G and $K_2 = 3 \times 10^{-13}$ cm³/s at $|B - B_{\text{res}}| = \Delta B$ which in the model corresponds to $\text{Re}(a)/a_{\text{bg}} - 1 = \pm 1$. Both experimentally observed values are somewhat larger than the expectation. This might be due to contributions from other bound-to-bound and photoassociation resonances that we did not include in this estimate.

We tried to reduce K_2 even further by setting the power of the bound-to-bound light to 66 mW and its frequency to 382,050,911 MHz which corresponds to a detuning of $\Delta_L/2\pi = 3.33$ GHz from the nearest bound-to-bound resonance. The expected and observed shifts were -0.35 G and ~ -0.65 G, respectively. But here we observed $K_2 \sim 3 \times 10^{-12}$ cm³/s at $|B - B_{\text{res}}| = \Delta B$, which is much worse than the expectation $K_2 = 1 \times 10^{-13}$ cm³/s. As the detuning is much larger than in Fig. 5.9, other bound-to-bound and photoassociation resonances contribute even more strongly to the signal, which might explain the increased deviation between the observed values and the estimates based on the two π resonances of Tab. 5.1.

6. Experimental Progress towards Localization of Matter Waves in a Disorder Potential

When a particle is subjected to a disorder potential, its wave function may be localized under certain circumstances. In this chapter we study the realization of a disorder potential and the physical behavior of matter waves in such a random potential.

Sec. 6.1 summarizes Refs. [Ros06a, Ros07, Hor07], in which the phase diagram for particles in the presence of a disorder potential is investigated theoretically. Characteristic signatures of relevant quantum phases are presented. In Sec. 6.2, we discuss the experimental realization of a random potential in our setup and present experimental progress towards localization of matter waves.

6.1. A Mobile and a Frozen Species in an Optical Lattice

6.1.1. General Concept

The absence of diffusion of a wave packet in a random potential is known as localization. Localization of matter waves in disordered media was originally predicted in the context of electron transport in condensed matter systems, where impurities and defects cause the randomness [And58]. However, matter wave localization can be generalized to various physical systems [Tig99]. The localization originates from the interference between multiple scattering paths. To observe localization of a wave packet inside a disorder potential due to quantum interference, certain conditions need to be met.

The first condition is that the spatial extension Δz of the wave packet must exceed the typical length scale ξ of the disorder fluctuations. Interference of the wave components between multiple scattering paths only emerges, if the wave packet samples a part of the potential that actually shows disorder and thus probes numerous local extrema of the random potential. Otherwise, the wave packet might be trapped in a single extremum of the disorder potential. The latter phenomenon is a classical form of localization, where no quantum interference occurs.

A second condition occurs in many-particle systems. Localization of a matter wave is a single-particle phenomenon. If more than one particle is subjected to a random potential, the interaction energy between the particles becomes relevant. This energy can be characterized by the chemical potential μ . An energy scale that characterizes

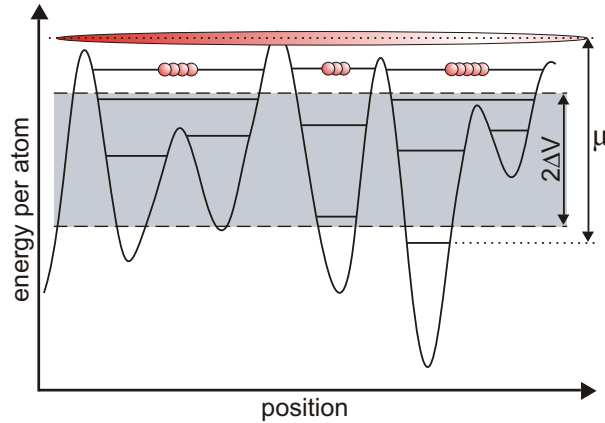


Figure 6.1.: Screening of the disorder potential. If the interaction strength between the particles is so strong that the corresponding chemical potential μ is larger than twice the standard deviation ΔV of the disorder potential, then the random potential is screened by parts of the mobile particles. The rest of the particles forms a superfluid which is delocalized over the entire sample.

the typical potential depth of the local extrema in the random potential is the standard deviation ΔV of the disorder potential. If $\mu \gtrsim 2\Delta V$, some fraction of the particles may be localized in the local minima of the disorder potential and flatten out the random potential, as shown in Fig. 6.1. The remaining fraction resides in a delocalized state that is spread out over the entire potential. Possible localization signatures are then washed out [Sca91, Sch06]. To avoid this so-called screening effect, low particle densities or a low interaction strength are necessary.

Meeting these two conditions in an experiment, is a challenging task. Ultracold atomic quantum gases are a good candidate for studying the appearance of matter wave localization experimentally [Dam03, Blo08, Lew07]. This is because they offer the possibility to implement trapping geometries in one, two, and three dimensions employing optical lattices, to control the interatomic interactions, either by density control or with Feshbach resonances, to measure atomic density profiles, and to design well controlled disorder potentials.

One way to design a disorder potential for an ultracold quantum gas is to use the ac-Stark shift created by light with a random spatial intensity distribution. A first realization of this technique was performed with the introduction of laser speckle patterns [Lye05] and quasi-periodic optical lattices [Fal07]. In initial investigations [Lye05, Clé05, For05, Sch05, Fal07, Lye07, Whi09] the observation of localization was precluded either by insufficient length scales of the disorder ($\xi > \Delta z$) or by screening effects ($\mu > 2\Delta V$). Recently, these limitations were overcome by two experiments, that directly observed Anderson localization: In the Aspect group a BEC of ^{87}Rb atoms with very low density was subjected to a laser speckle pattern [Bil08], whereas in the Inguscio group a quasi-periodic lattice created by superimposing two standing waves with incommensurate wavelengths was used as a disorder potential for a BEC of ^{39}K , in which the interaction strength was

tuned close to zero using a magnetic Feshbach resonance [Roa08].

Before the Aspect group and the Inguscio group observed localization at the end of 2008, we pursued an alternative approach, in which the disorder potential is created using impurity particles with a random spatial distribution [Gav05, Par05, Mas06]. This is realized by particles that are frozen on randomly distributed sites of a deep optical lattice. A second species experiences a much shallower lattice potential and its particles are thus mobile. The lattice essentially discretizes the spatial coordinate. The wave functions of the mobile particles are spread out over various lattice sites and thus probe the random distribution of the frozen particles due to an on-site interaction between a mobile and a frozen particle. If the distribution of frozen particles shows no correlation for neighboring sites, then the issue of a too large correlation length ξ is solved. In addition, in our setup a screening of the disorder potential is prevented by tuning the interaction between the mobile particles to zero using a magnetic Feshbach resonance.

In our system, the disorder potential is superimposed with a harmonic trap with angular frequency ω_{ho} . The oscillator length $z_0 = \sqrt{\hbar/\omega_{\text{ho}}m}$ of a mobile particle with mass m inside this harmonic trap is much larger than ξ . The mobile particles are confined by the harmonic trap and thus do not disperse in our experiments. They essentially populate the ground state of the combined trap. Nevertheless, effects related to localization are predicted to be observable in this ground state [Ros06a, Ros07].

6.1.2. A Two Species Bose-Hubbard Model

Localization in a mixture of a frozen and a mobile bosonic species inside an optical lattice has been explored theoretically in Refs. [Ros06a, Ros07, Hor07]. Here, we briefly summarize the central results of these investigations.

We consider the case of completely frozen $|\downarrow\rangle$ particles inside an optical lattice, where the number of frozen particles $n_{\downarrow,i} \in \{0, 1\}$ is random for each lattice site i . The frozen particles serve as impurities for particles of the mobile species $|\uparrow\rangle$ inside the optical lattice. The Hamiltonian of this system reads

$$\mathcal{H} = J_{\uparrow} \sum_{\langle i,j \rangle} \left(a_{\uparrow,i} a_{\uparrow,j}^{\dagger} + H.c. \right) + \frac{U_{\uparrow\uparrow}}{2} \sum_i n_{\uparrow,i} (n_{\uparrow,i} - 1) + U_{\uparrow\downarrow} \sum_i n_{\downarrow,i} n_{\uparrow,i}, \quad (6.1)$$

where J_{\uparrow} is the tunneling amplitude of the mobile atoms and $U_{\uparrow\uparrow}$ the on-site interaction strength between mobile atoms, in analogy to Eq. (2.6). $n_{\uparrow,i} = a_{\uparrow,i}^{\dagger} a_{\uparrow,i}$ is the number of mobile particles at lattice site i . $U_{\uparrow\downarrow}$ is the on-site interaction strength between one mobile and one frozen particle. The last term in Eq. (6.1) creates a random potential for the mobile particles, as sketched in Fig. 6.2. In the experiment, such a Hamiltonian can be realized with a spin state dependent ac-Stark shift in an optical lattice, as described in the Sec. 6.1.3. The on-site interaction $U_{\uparrow\uparrow}$ of the mobile species is tunable with a Feshbach resonance, see Sec. 2.1.

Signatures of the ground state of the Hamiltonian in Eq. (6.1) for a 1D system were studied theoretically using quantum Monte Carlo simulations [Ros06a, Ros07]. Fig. 6.3

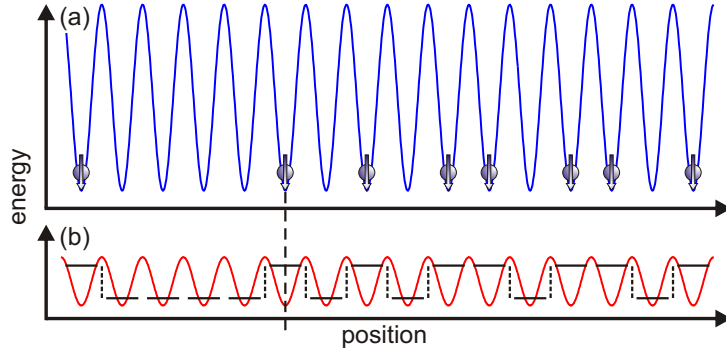


Figure 6.2.: Creation of a disorder potential. (a) A deep optical lattice (blue line) prevents particles of the frozen species $|\downarrow\rangle$ from hopping from site to site. The particle number $n_{\downarrow,i}$ at site number i equals 0 or 1 and is random from site to site. The frozen particles serve as scattering impurities for a mobile species $|\uparrow\rangle$. (b) The mobile species (not shown) experiences a shallow lattice depth (red line) that discretizes the spatial coordinate to single lattice sites. An on-site interaction $U_{\uparrow\downarrow}$ between mobile $|\uparrow\rangle$ and frozen $|\downarrow\rangle$ particles maps the random spatial distribution of the frozen particles to on-site energy shifts for mobile particles and creates a disorder potential for the mobile species (black line).

shows the peak density in momentum space $n_{\uparrow}(k=0)$ and the superfluid fraction $\rho_{s,\uparrow}$ of the mobile species as functions of $U_{\uparrow\downarrow}/J_{\uparrow}$. In the studied parameter range four phases are identified: a localized phase (LOC), a superfluid (SF), a Bose glass (BG), and a Mott insulator (MI). For what follows, we are interested in the weakly interacting regime $U_{\uparrow\downarrow}/J_{\uparrow} \lesssim 8$, where only the LOC phase and the SF phase appear. In this regime, the values for $n_{\uparrow}(k=0)$ and $\rho_{s,\uparrow}$ can serve as a measure to assign the quantum phase, in which the mobile species resides for a given ratio $U_{\uparrow\downarrow}/J_{\uparrow}$. Experimentally, $n_{\uparrow}(k=0)$ is accessible by time-of-flight imaging.

We briefly describe the physical properties of the LOC and the SF phase. In the localized phase the single wave functions of the mobile particles are spatially localized by the interference of wave components between multiple scattering paths reflected off frozen impurity atoms. The spatial extension of the wave functions covers various impurity centers of the disorder potential. In time-of-flight images the experimental signature of this phase is a small atomic peak density at zero momentum $n_{\uparrow}(k=0)$, see Fig. 6.3(a) at $U_{\uparrow\downarrow}/J_{\uparrow} \lesssim 3$.

If the interaction strength $U_{\uparrow\downarrow}$ of the mobile particles is comparable to the interaction strength $U_{\uparrow\downarrow}$ between mobile and frozen particles, the disorder potential is screened by some fraction of the mobile particles and the remaining atoms reside in a delocalized, spatially extended superfluid state, as sketched in Fig. 6.1. This phase exhibits a large atomic density $n_{\uparrow}(k=0)$ around zero momentum and a significant superfluid fraction $\rho_{s,\uparrow}$, see Fig. 6.3(a) at $3 \lesssim U_{\uparrow\downarrow}/J_{\uparrow} \lesssim 8$.

The value of $U_{\uparrow\downarrow}/J_{\uparrow}$, at which the behavior of the system changes from localized to superfluid, depends on the impurity concentration $\langle n_{\downarrow,i} \rangle$, as shown in the phase diagram of Fig. 6.3(b). Note, that the simulations of Fig. 6.3 were performed for $n_{\downarrow,i} \in \{0, 1\}$. Thus,

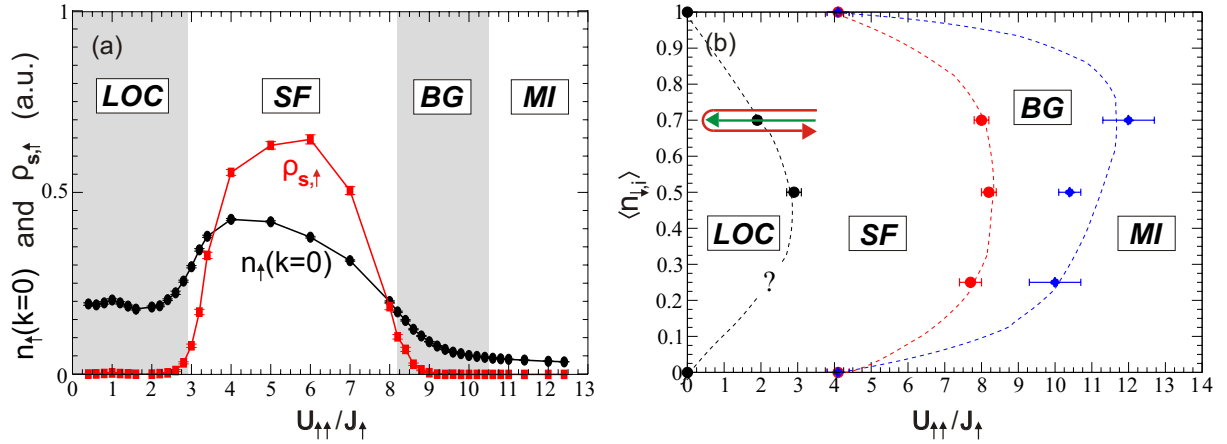


Figure 6.3.: Predictions for the ground state properties of the Hamiltonian in Eq. (6.1) for a 1D system. (a) The peak density at zero momentum $n_{\uparrow}(k=0)$ and the superfluid fraction $\rho_{s,\uparrow}$ of the mobile species are shown as a function of $U_{\uparrow\uparrow}/J_{\uparrow}$. Based on the values of $n_{\uparrow}(k=0)$, $\rho_{s,\uparrow}$, and the compressibility (not shown), different quantum phases of the mobile species can be identified (LOC: localized phase, SF: superfluid, BG: Bose glass, and MI: Mott insulator). The simulation was performed with parameters $\langle n_{\downarrow,i} \rangle = 0.5$, $\langle n_{\uparrow,i} \rangle \simeq 1$, and $U_{\uparrow\downarrow} = 5J_{\uparrow}$. (b) Phase diagram arising from a set of simulations as in (a) with different impurity concentrations $\langle n_{\downarrow,i} \rangle$ showing the ratio of $U_{\uparrow\uparrow}/J_{\uparrow}$, where the quantum phase changes its character. The dashed lines are guides to the eye. The exact position of the phase boundary between LOC and SF around '?' is difficult to determine. The red and green arrow represent experiments discussed in Figs. 6.7 and 6.8, see Sec. 6.2.3. Adapted from Ref. [Ros06a].

$\langle n_{\downarrow,i} \rangle = 1$ implies $n_{\downarrow,i} = 1$ for all i so that there is no disorder. For this reason, the phase diagram in Fig. 6.3(b) is roughly symmetric under reflection off the line $\langle n_{\downarrow,i} \rangle = 0.5$. In the more realistic scenario with $n_{\downarrow,i} \in \{0, 1, 2, \dots\}$ this artificial vanishing of the disorder is expected to disappear [Ros06b].

6.1.3. An ac-Stark Shift that Depends on the Zeeman State

The mobile and the frozen species in the scheme discussed so far could be different chemical elements, isotopes, or internal states. Our experimental implementation uses different hyperfine states in ^{87}Rb . We now describe, how a different lattice depth for these states can be realized.

In Sec. 3.3, the ac-Stark shift for a two-level atom was described, see Eq. (3.11). In a multi-level atom, however, the various electric dipole matrix elements typically differ. This makes it possible to implement an optical lattice with different depths for different Zeeman states. In the limit of large detuning, several excited states may contribute noticeable to the ac Stark shift. The ground and excited states can be characterized by angular momentum quantum numbers. For alkali atoms, the spin \vec{S} and the orbital angular momentum \vec{L} of the valence electron couple to a total electronic angular momentum $\vec{J} = \vec{L} + \vec{S}$. This coupling leads to fine structure splitting. Moreover, the coupling of \vec{J}

with the nuclear spin \vec{I} results in hyperfine splitting for different values of $\vec{F} = \vec{J} + \vec{I}$.

We assume that the detuning of the light frequency from the transition frequencies is much larger than all hyperfine splittings and that there is only one value of J for atoms in the ground state, namely $J = 1/2$. The ac-Stark shifts at $B = 0$ are known from the literature [Cho97, Mil02]

$$\Delta E = \Delta E_{1/2}^{cyc} \frac{1 - g_F m_F q}{3} + \Delta E_{3/2}^{cyc} \frac{2 + g_F m_F q}{3}, \quad (6.2)$$

where m_F is the magnetic quantum number. $g_F \sim g_J[F(F+1) + S(S+1) - I(I+1)]/[2F(F+1)]$ and g_J are the Landé factors belonging to F and J , respectively. $q = -1, 0, +1$ for σ^- , π , and σ^+ polarization, respectively. We abbreviate $\Delta E_J^{cyc} = |E d_{cyc}|^2 / (4\hbar \Delta_J)$ where E is the electric field amplitude, Δ_J is the detuning for the excited state with quantum number J' and d_{cyc} is the dipole matrix element of the cycling transition $|F = m_F = I + 1/2\rangle \leftrightarrow |F' = m'_F = I + 3/2\rangle$. For σ^+ or σ^- polarization, the energies of states with different values of m_F are split equidistantly. This property of the splitting is reminiscent of the linear Zeeman effect and therefore sometimes referred to as a fictitious magnetic field [CT72].

Our experiments are performed with a magnetic field applied. The resulting level shifts are much larger than the ac-Stark shift so that the latter can be treated as a weak perturbation. Following the calculations in Appendix A, we obtain the ac-Stark shift of an alkali ground state atom in spin state $|F, m_F\rangle$ as

$$\Delta E = \Delta E_{1/2}^{cyc} \frac{1 - \beta q}{3} + \Delta E_{3/2}^{cyc} \frac{2 + \beta q}{3}, \quad (6.3)$$

where for $|m_F| < I + 1/2$

$$\beta = \pm \cos \theta \quad \text{for states adiabatically connected to } F = I \pm \frac{1}{2} \quad (6.4a)$$

$$\cos \theta = \frac{\alpha + \chi}{\sqrt{1 + 2\alpha\chi + \chi^2}} \quad (6.4b)$$

$$\alpha = m_F / (I + 1/2) \quad (6.4c)$$

$$\chi = (g_J - g_I) \mu_B B / (\hbar \omega_{HFS}) \quad (6.4d)$$

with $0 \leq \theta \leq \pi$. In addition, $\beta = \pm 1$ for $m_F = \pm(I + 1/2)$. Here, μ_B is the Bohr magneton, $\hbar \omega_{HFS}$ the hyperfine splitting, and g_I the Landé factor of the nucleus, see Tab. A.1.

For the rest of this chapter, we only consider two specific spin states of atomic ^{87}Rb , namely

$$|\uparrow\rangle = |F = 1, m_F = 1\rangle \quad (6.5a)$$

$$|\downarrow\rangle = |F = 2, m_F = 2\rangle. \quad (6.5b)$$

In a 1D optical lattice created by a standing wave with σ^+ polarization, Eq. (6.3) results in different lattice depths¹ for atoms of spin states $|\uparrow\rangle$ and $|\downarrow\rangle$, as shown in Fig. 6.4(a)

¹Throughout this chapter, lattice depths are given in units of $E_{rec} = \hbar^2 / (2m\lambda^2) = 3.33$ kHz, which is the recoil energy for a ^{87}Rb atom absorbing a photon of wavelength $\lambda = 830$ nm.

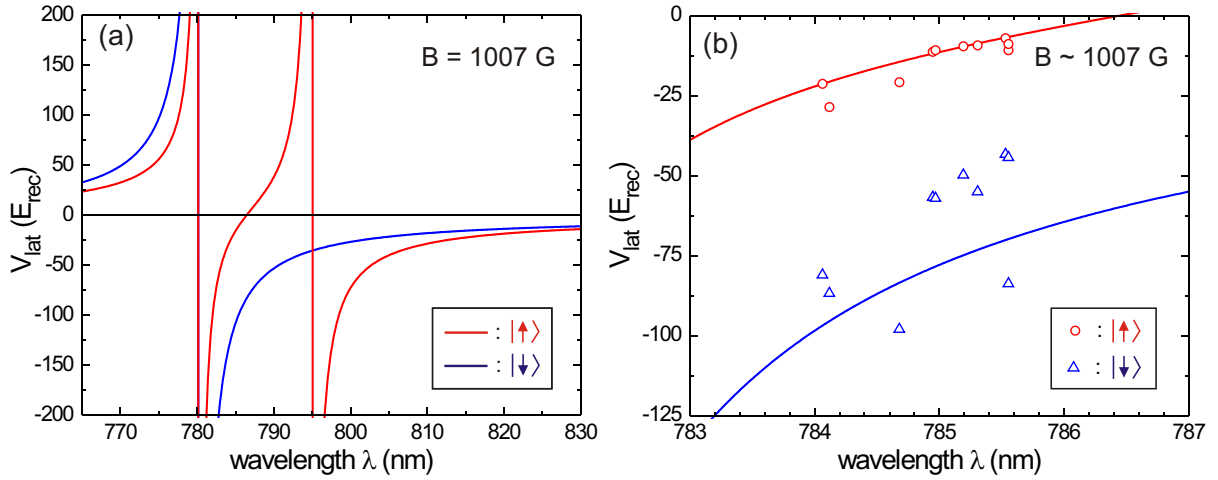


Figure 6.4.: ac-Stark shift for ^{87}Rb atoms in states $|\uparrow\rangle = |F = 1, m_F = 1\rangle$ and $|\downarrow\rangle = |F = 2, m_F = 2\rangle$ of the electronic ground state. (a) Eq. (6.3) is shown at the antinodes of a standing light wave with σ^+ polarization. The resulting lattice depth¹ V_{lat} is plotted as a function of the light wavelength for $B = 1007$ G, a traveling-wave power of 25 mW, and a beam waist of $135 \mu\text{m}$. (b) Experimental data for the ac-Stark shift as a function of the lattice wavelength at ~ 1007 G. The solid lines represent the theory from (a) with the light intensity as the only fit parameter.

at $B = 1007$ G as a function of the lattice wavelength. For the experiments of this chapter, we typically use lattice wavelengths between 784 and 786 nm. Therefore, state $|\uparrow\rangle$ represents the mobile species, whereas $|\downarrow\rangle$ represents the frozen species. To illustrate the size of the effect of the magnetic field, we consider the so-called magic wavelength where the ac-Stark shift vanishes. For state $|\uparrow\rangle$ this lies at 787.54 nm for $B = 0$ and at 786.44 nm for $B = 1007$ G.

In Fig. 6.4(b), we present experimental data of the ac-Stark shift in our setup for states $|\uparrow\rangle$ and $|\downarrow\rangle$ as a function of the lattice wavelength. The lattice depth was characterized by employing the calibration method described in Refs. [HD02, Vol07]. The solid lines represent the theoretical expectation from Eq. (6.3), where the light intensity was determined from a fit of both curves to all data points simultaneously. The value obtained from the fit agrees with an independent measurement of the light power and the waist within a factor of 1.4. Within the range from 784 to 786 nm, the lattice depth for the mobile species varies by a factor of ~ 3 , whereas the lattice depth for the frozen particles changes only moderately. The lattice wavelength thus allows for tuning J_{\uparrow} without changing the fact that the $|\downarrow\rangle$ particles are frozen.

The boundaries of the wavelength range that is useful for our experiments are set by the following considerations. First, too far away from the magic wavelength, the values of J_{\uparrow} and J_{\downarrow} become too similar, and second, too close to the magic wavelength, achieving an appreciable lattice depth V_{\uparrow} requires so large laser intensities that spontaneous scattering of photons becomes an issue, see Sec. 6.2.1.

6.1.4. Creation of a Random Spatial Distribution

To prepare a mixture of $|\uparrow\rangle$ and $|\downarrow\rangle$ atoms in our experiment, we start with a sample of $|\uparrow\rangle$ atoms and apply a microwave field to coherently transfer the atoms from state $|\uparrow\rangle$ into a superposition state $\cos\alpha|\uparrow\rangle + \sin\alpha|\downarrow\rangle$. Experimental details about the transfer are discussed in Secs. 6.2.1 and 6.2.2. Here, we describe why this results in a random spatial distribution.

As in Eq. (2.9), the many-particle state of the initial superfluid sample of N $|\uparrow\rangle$ atoms reads in second quantization

$$|\Psi\rangle = \left(\sum_i \phi_i a_{\uparrow,i}^\dagger \right)^N |0\rangle, \quad (6.6)$$

where $a_{\uparrow,i}^\dagger$ creates an $|\uparrow\rangle$ atom at lattice site i . $|0\rangle$ is the vacuum state. $\sum_i \phi_i a_{\uparrow,i}^\dagger$ thus creates an $|\uparrow\rangle$ atom delocalized over many sites with amplitudes ϕ_i that must meet $\sum_i |\phi_i|^2 = 1$. The power of N in Eq. (6.6) means that N atoms are created in the same single-particle wave function. The transfer from state $|\uparrow\rangle$ to $|\downarrow\rangle$ is fast in comparison to all relevant time scales of the Hamiltonian in Eq. (6.1). We thus represent the transfer by the substitution

$$a_{\uparrow,i}^\dagger \rightarrow \sin\alpha a_{\downarrow,i}^\dagger + \cos\alpha a_{\uparrow,i}^\dagger, \quad (6.7)$$

where $a_{\downarrow,i}^\dagger$ creates a $|\downarrow\rangle$ atom at lattice site i . We assume, that the transfer takes place in the Lamb-Dicke regime [CT92], so that it is possible to occupy almost exclusively the lowest motional state of the $|\downarrow\rangle$ atoms at site i . After the transfer, the many-particle state in Eq. (6.6) becomes

$$|\Psi\rangle = \sum_{N_\downarrow} b(N_\downarrow, \alpha) \left[\left(\sum_i \phi_i a_{\downarrow,i}^\dagger \right)^{N-N_\downarrow} \left(\sum_i \phi_i a_{\uparrow,i}^\dagger \right)^{N_\downarrow} \right] |0\rangle, \quad (6.8)$$

where we used the binomial formula and $b(N_\downarrow, \alpha) = \binom{N}{N_\downarrow} \sin^{N-N_\downarrow}\alpha \cos^{N_\downarrow}\alpha$.

As atoms in state $|\downarrow\rangle$ are frozen on single lattice sites, it will be convenient for the following calculation to describe them in a Fock state representation in first quantization. We thus rewrite Eq. (6.8) as a tensor product

$$|\Psi\rangle = \sum_{\{n_{\downarrow,i}\}} \left[c_{\{n_{\downarrow,i}\}} |\{n_{\downarrow,i}\}\rangle \otimes \left(\sum_i \phi_i a_{\uparrow,i}^\dagger \right)^{N_\downarrow} |0\rangle \right], \quad (6.9)$$

where $\{n_{\downarrow,i}\}$ represents all possible distributions of frozen atoms across the available lattice sites that are compatible with a given total particle number N . $c_{\{n_{\downarrow,i}\}}$ are the corresponding expansion coefficients, which also include $b(N_\downarrow, \alpha)$. The Hamiltonian in

Eq. (6.1) determines the time evolution of this state. Atoms in state $|\downarrow\rangle$ are prevented from tunneling. Thus, the eigenstates $|\{n_{\downarrow,i}\}\rangle$ are conserved and only pick up a time dependent phase, which can be absorbed in the time dependent evolution of the mobile species. Hence,

$$|\Psi(t)\rangle = \sum_{\{n_{\downarrow,i}\}} [c_{\{n_{\downarrow,i}\}} |\{n_{\downarrow,i}\}\rangle \otimes |\Psi_{\{n_{\downarrow,i}\}}(t)\rangle], \quad (6.10)$$

where $|\Psi_{\{n_{\downarrow,i}\}}(t)\rangle$ is the time evolved many-particle state of the mobile species, that depends on the atom number distribution $\{n_{\downarrow,i}\}$ of the frozen species. As discussed in Sec. 6.1.2, we are interested in the measurement of a physical observable \hat{A}_{\uparrow} that acts only on state $|\Psi_{\{n_{\downarrow,i}\}}(t)\rangle$. The corresponding expectation value is given by

$$\langle\Psi(t)| \hat{1}_{\downarrow} \otimes \hat{A}_{\uparrow} |\Psi(t)\rangle = \sum_{\{n_{\downarrow,i}\}} \left[|c_{\{n_{\downarrow,i}\}}|^2 \otimes \langle\Psi_{\{n_{\downarrow,i}\}}(t)| \hat{A}_{\uparrow} |\Psi_{\{n_{\downarrow,i}\}}(t)\rangle \right]. \quad (6.11)$$

Due to the summation over $\{n_{\downarrow,i}\}$, all possible spatial distributions of the frozen species are probed by measurement of \hat{A} within a single experimental shot. In general, the combinations in $\{n_{\downarrow,i}\}$ include ordered and disordered spatial distributions of the frozen atoms. For example, consider three lattices sites occupied by $N_{\downarrow} = 3$ frozen atoms. Here, the possible combinations for $\{n_{\downarrow,i}\}$ are (3,0,0), (0,3,0), (0,0,3), (2,1,0), (2,0,1), (1,2,0), (1,0,2), (0,2,1), (0,1,2), and (1,1,1). Obviously, the majority of these terms that contribute to the sum in Eq. (6.11) show disorder.

Note, that the coherence of the superposition in Eq. (6.10) might be lost due to experimental imperfections, such as magnetic field fluctuation. However, as only $|c_{\{n_{\downarrow,i}\}}|^2$ enters in Eq. (6.11) the observation of localization in our experiments does not rely on the coherent character of the superposition.

6.2. Experimental Attempt to Localize Matter Waves in a Disorder Potential

6.2.1. Experimental Sequence

Experimentally, it is possible to create a disorder potential for the mobile particles in state $|\uparrow\rangle$ by preparing a disordered distribution of the frozen $|\downarrow\rangle$ particles using the Zeeman dependent ac-Stark shift of an optical lattice. The general idea is to probe the quantum phase transition from a superfluid to a localized ground state for the mobile species by decreasing the interaction strength between the mobile particles using a magnetic Feshbach resonance.

The experimental sequence is the following: We start with a BEC of atoms in spin state $|\uparrow\rangle$ in an optical dipole trap at a magnetic field a few Gauss away from a Feshbach resonance at 1007.4 G. Details of the optical dipole trap are given in Sec. 3.3. The initial BEC is approximately spherical with a Thomas-Fermi radius of $\sim 20 \mu\text{m}$. The BEC is transferred into an optical lattice, that consists of three mutually orthogonal

standing waves, as described in Sec. 3.4.2. Along x and y we employ linearly polarized light with wavelengths $\lambda_x = \lambda_y = 830.44$ nm. During the transfer the power of the x and y beam is exponentially increased within 40 ms to final lattice depths of typically $V_x = V_y = 20(2) E_{rec}$. This corresponds to tunneling amplitudes of $J_x = J_y = \hbar/(120 \text{ ms})$ independent of the hyperfine state of an atom. Particles in both states $|\uparrow\rangle$ and $|\downarrow\rangle$ are thus confined in an array of tubes and the essential physics takes place in a 1D geometry along z . Along the z direction we apply σ^+ polarized lattice light with a wavelength of $\lambda_z \sim 785$ nm. The beam power along z is increased exponentially within 5 ms and reaches its final value simultaneously with the x and y lattice beams. The shorter ramp-up time for the z -beam is possible because of the smaller final lattice depth. The lattice depth, polarization, and wavelength of the z lattice beam are chosen such that the $|\uparrow\rangle$ atoms are allowed to easily tunnel from site to site and are thus delocalized along z . Furthermore, the parameters meet the condition $U_{\uparrow\downarrow}/J_{\uparrow} = 5$, as used in the simulations of Fig. 6.3.

After loading the cloud of $|\uparrow\rangle$ atoms into the lattice, a microwave field is applied for $50 \mu\text{s}$ to coherently transfer the atoms in state $|\uparrow\rangle$ to a superposition state $\frac{1}{\sqrt{2}}(|\uparrow\rangle + |\downarrow\rangle)$, see Sec. 6.2.2. According to Sec. 6.1.4, this results in a spatial disorder potential for the mobile species and the characteristic length scale ξ of disorder fluctuations is expected to be on the order of $\lambda_z/2$. This is much smaller than the spatial extension Δz of the wave function of the mobile atoms, which is on the order of the Thomas-Fermi radius of the initial BEC.

Note that in ^{87}Rb the singlet and the triplet scattering lengths are almost identical [vK02], which results in $a_{\uparrow\uparrow} \sim a_{\uparrow\downarrow} \sim a_{\downarrow\downarrow}$. However, $U_{\uparrow\uparrow}$, $U_{\uparrow\downarrow}$, and $U_{\downarrow\downarrow}$ differ somewhat because of the different lattice depths $V_{\uparrow,z}$ and $V_{\downarrow,z}$, see Eq. (2.8). $U_{\uparrow\uparrow}$ is large enough that the mobile particles remain superfluid due to screening, as shown in Fig. 6.1. A further step of our experiments is to reduce $U_{\uparrow\uparrow}$ close to zero using a Feshbach resonance to probe the quantum phase transition from a superfluid to a localized phase, as predicted in Sec. 6.1.2. Experimental results on this topic are presented in Sec. 6.2.3.

For detection, we first release the atoms by switching off all trapping potentials simultaneously and then take a time-of-flight image after an expansion time of 7-15 ms. Optionally, we can apply a Stern-Gerlach field during an early stage of the expansion for ~ 2 ms to separate the clouds of the two species from each other. Ideally, the time-of-flight images would directly reflect the momentum distribution before release. In practice, this relation is complicated somewhat by the mean-field energy which is converted into kinetic energy, mostly during the early expansion phase. In our experiments in this section, the magnetic field is always switched off at the moment where the cloud is released, so that the scattering length takes on its background value during the complete time of flight.

Spontaneous scattering of lattice photons can become an issue in the experiment. The dominant contribution comes from the ~ 785 nm light. Combination of Eqs. (3.12) and (6.3) yields a scattering rate of

$$\Gamma_{sp} = \frac{\Gamma_0}{\hbar} \left[\frac{\Delta E_{1/2}^{cyc}}{\Delta_{1/2}} \frac{1 - \beta q}{3} + \frac{\Delta E_{3/2}^{cyc}}{\Delta_{3/2}} \frac{2 + \beta q}{3} \right]. \quad (6.12)$$

We typically choose the experimental parameters such that we estimate an average

number of scattered photons of only ~ 0.03 per atom. The corresponding recoil heating adds two photon recoil energies per average scattering event. Given the low number of scattering events, recoil heating is negligible compared to $U_{\uparrow\downarrow} \sim 0.37 E_{rec}$. Spontaneous scattering also leads to optical pumping into other ground states. With these low numbers of scattering events, optical pumping is negligible. By deliberately leaving the lattice light on for much longer times, we were able to observe optical pumping in images with Stern-Gerlach separation. We thus confirmed Eq. (6.12) experimentally.

The requirement to keep the number of scattered photons low forces us to have the lattice light on for only a limited time. This time includes the ramp up of the ~ 785 nm lattice. As we are interested in ground state properties, this ramp should be ideally be rather long in order to guarantee adiabaticity. Our choice of parameters is a compromise between photon scattering and adiabaticity. A similar argument applies to the ramps in B which tune $U_{\uparrow\uparrow}$ and should be adiabatic as well. They also take place with the ~ 785 nm light on so that a similar compromise must be found. For these ramps, light-induced two-body loss near the Feshbach resonance is also an issue, see Sec. 6.2.3. This forces us to use even shorter ramp times for B than if we were fighting only normal photon scattering.

6.2.2. State Preparation

A crucial point of the experimental sequence described in Sec. 6.2.1 is the partial transfer of population in spin state $|\uparrow\rangle$ to state $|\downarrow\rangle$ using a microwave pulse. This transfer must meet three conditions: First, the magnetic field must be temporally stable. To this end, the magnetic field noise at ~ 1007 G is suppressed below 4 mG (rms) on a time scale of 50 ms using a home-built servo loop [Dür04b], see Sec. 3.2.1. Additionally, we trigger the microwave pulse on the ac line voltage [Näg08]. Second, spatial homogeneity of the magnetic field is necessary. Otherwise, atoms could be transferred only in a small spatial region and/or the corresponding Stern-Gerlach force could spatially separate the two species after the transfer. Two additional pairs of coils in our setup solve these problems (see Sec. 3.2.2).

We confirm the temporal stability and spatial homogeneity of the magnetic field by observing a time-resolved 2π Rabi oscillation between states $|\uparrow\rangle$ and $|\downarrow\rangle$ at a magnetic field of 1009.18 G. For this experiment, we load a sample of $|\uparrow\rangle$ atoms into the optical lattice as described in Sec. 6.2.1. Here, we use $\lambda_z = 785.22$ nm and $V_{\uparrow,z} = 2(1) E_{rec}$. A microwave pulse at a frequency of 9133.523 MHz is applied for a variable time. Subsequently, the power of all lattice beams is ramped down slowly and a time-of-flight image with Stern-Gerlach separation is taken. Fig. 6.5 shows the atom number in each species as a function of the pulse duration. The almost complete transfer from the initial state $|\uparrow\rangle$ to state $|\downarrow\rangle$ for a pulse duration of ~ 100 μ s shows that the frequency of the microwave pulse is resonant with the atomic transition and that the magnetic field is spatially homogeneous.

The third requirement is that the transfer should not create band excitations in the optical lattice because this would lead to noticeable tunneling of the frozen species. In addition, interspecies collisions could heat the mobile species. When scanning the microwave

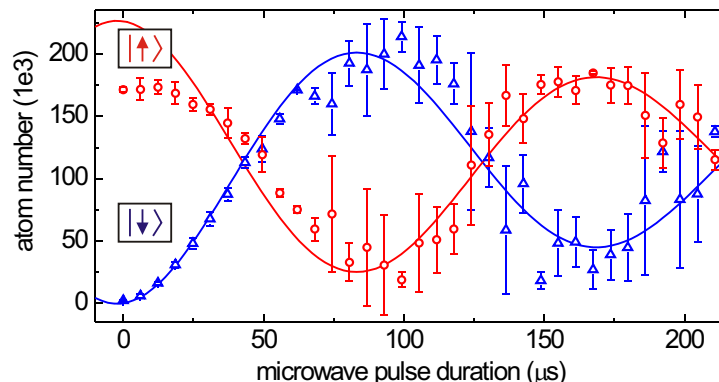


Figure 6.5.: Rabi oscillation between two hyperfine states in an optical lattice at 1009.18 G. The atom number oscillates between the spin state $|\uparrow\rangle$ (red) and $|\downarrow\rangle$ (blue) as a function of the pulse duration of the microwave field. The blue line is a fit of $A[1 - e^{-t/\tau} \cos(\omega t)]$ to Δ . The best fit parameters are used for plotting the red line which shows $A[1 + e^{-t/\tau} \cos(\omega t)]$. For a pulse duration of $\sim 100 \mu\text{s}$, 92(2)% of the initial population in state $|\uparrow\rangle$ are transferred to state $|\downarrow\rangle$. A $\pi/2$ -pulse is realized at $\sim 50 \mu\text{s}$.

frequency we can resolve the band structure², as seen in Fig. 6.6, which is recorded with the same experimental sequence as for Fig. 6.5 except that now $B = 1009.10 \text{ G}$, $\lambda_z = 786.09 \text{ nm}$, and $V_{\uparrow,z} = 5(2) E_{rec}$ corresponding to $V_{\downarrow,z} = 22(9) E_{rec}$. The microwave pulse lasts $90 \mu\text{s}$. Fig. 6.6(a) shows the number of $|\downarrow\rangle$ atoms as a function of the microwave frequency. The spectrum displays two resonances corresponding to the lowest energy band and the second excited band. The energy gap between these two bands is $45(3) \text{ kHz}$, which agrees with the theoretical expectation of $53(18) \text{ kHz}$. We think, that a population of the first excited band is suppressed due to odd parity at quasi momentum zero. The width of the resonance of the lowest band in Fig. 6.6(a) is $4.6(3) \text{ kHz}$ (rms), which sets an upper bound for the magnetic field noise of 1.9 mG (rms) for the $90 \mu\text{s}$ time scale of the microwave pulse. We note, that a measurement for the same transition inside a dipole trap at $B \sim 1.5 \text{ G}$ yields a comparable upper bound for the magnetic field noise.

Fig. 6.6(b) shows the cloud width (FWHM) of the mobile species after time-of-flight which represents the momentum spread. The width increases for microwave frequencies that transfer atoms either to the upper band edge of the lowest band or to the second excited band because surplus energy is stored in the system. We attribute this heating to elastic collisions between mobile and frozen atoms. In the following, we avoid heating and population of excited lattice bands using a microwave frequency as indicated by the dashed line in Fig. 6.6(b).

Note, that for the experimental parameters of our system the microwave wavelength is much longer than the size of the wave packet at an individual lattice site. Thus, the transfer from state $|\uparrow\rangle$ to $|\downarrow\rangle$ is deeply in the Lamb-Dicke regime, as assumed in Sec. 6.1.4.

²A similar experiment resolved the lattice band structure when creating molecules with a Raman transition instead of the microwave transition [Rom04].

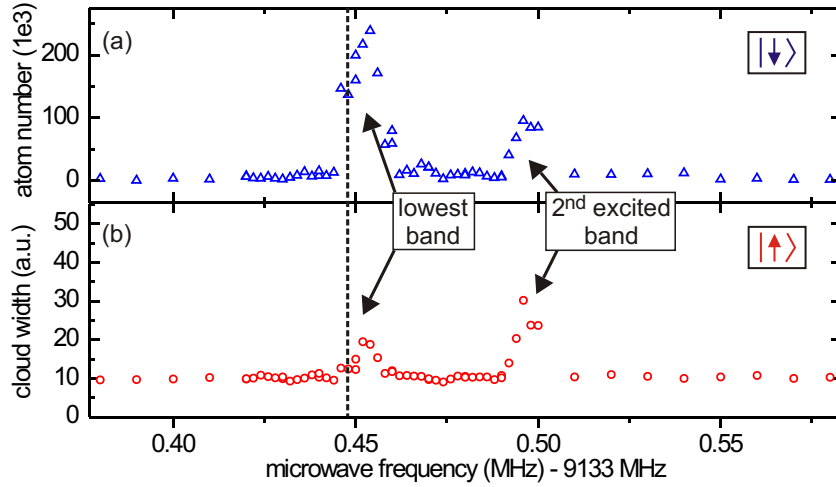


Figure 6.6.: Microwave spectroscopy of the band structure in an optical lattice at 1009.10 G. (a) Atom number in the frozen state $|\downarrow\rangle$. The lowest and the second excited energy band of the lattice potential are resolved. The first excited band is not populated due to symmetry. (b) Momentum spread of atoms in the mobile state $|\uparrow\rangle$. When atoms are transferred either to the upper band edge of the lowest band or to the second excited band, the momentum spread of the mobile species increases. This is probably due to collisions that transfer energy from the frozen to the mobile species. In the following, we choose a microwave frequency indicated by the dashed line, where the population transfer is high and the heating is small.

6.2.3. Probing the Phase Transition

The controlled transfer of atoms from spin state $|\uparrow\rangle$ to state $|\downarrow\rangle$ in the lowest band of the optical lattice allows us to perform experiments aiming for the localization of matter waves as proposed in Sec. 6.1. As a crucial step in these experiments, a reduction of the interaction strength between the mobile particles is required to probe the phase transition to a localized phase. Here, we present experimental results of this attempt.

We prepare the system as described in Sec. 6.2.1. We use $B = 1009.18$ G, $\lambda_z = 784.142$ nm, and $V_{\uparrow,z} = 5.8(5) E_{rec}$ corresponding to $V_{\downarrow,z} = 20(2) E_{rec}$. The estimated tunneling amplitudes are $J_{\uparrow,z} \sim h/(5.0$ ms) and $J_{\downarrow,z} \sim h/(105$ ms). A microwave $\pi/2$ -pulse is applied. The peak density of the initial BEC is 8.3×10^{13} cm $^{-3}$ resulting in a maximum atom number of 1.6 per spatial volume $\lambda_x \lambda_y \lambda_z / 8$. This corresponds to a maximum of $\langle n_{\downarrow,i} \rangle \sim 0.8$ after the transfer.

In the next experimental step, we employ a magnetic field ramp to address a Feshbach resonance for state $|\uparrow\rangle$ at $B_{pole} = 1007.4$ G with a width of $\Delta B = 0.2$ G [Vol03, Dür04b]. Close to the Feshbach resonance, the scattering length $a_{\uparrow\uparrow}$ and thus the interaction strength $U_{\uparrow\uparrow}$ are functions of B , see Eqs. (2.3) and (2.8). The changes in $U_{\uparrow\downarrow}$ and $U_{\downarrow\downarrow}$ are negligible. The magnetic field ramp belongs to one of the three following schemes. In the first scheme, we just hold the magnetic field for 18 ms at $B_{init} = 1009.18$ G, where $a/a_{bg} \sim 0.9$ and $U_{\uparrow\uparrow}/J_{\uparrow} \sim 5.8$. In this case, the mobile species is expected to reside in the superfluid phase due to screening. In the second scheme, we decrease the magnetic field

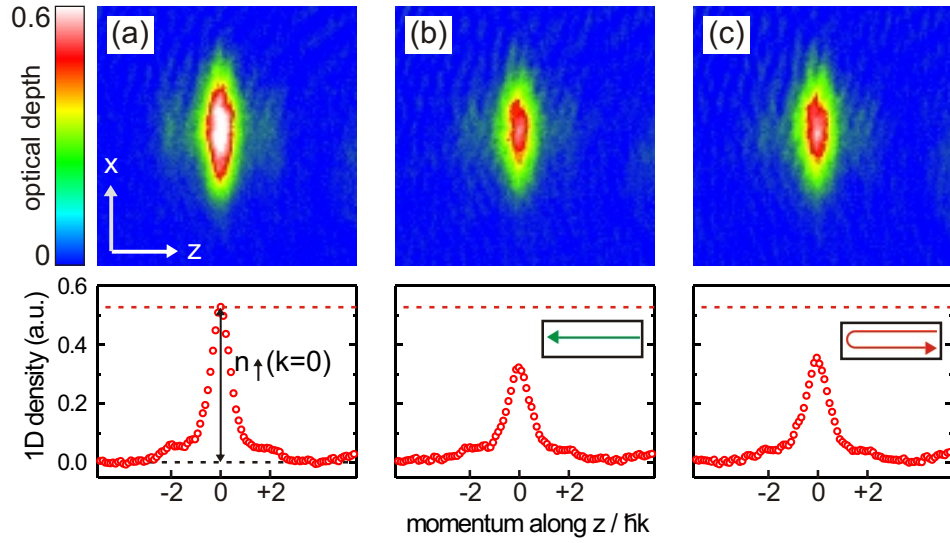


Figure 6.7.: Searching for the quantum phase transition. The upper panels show time-of-flight images where the optical depth corresponds to the 2D density distribution of the mobile species 7 ms after release from the optical lattice. The lower panels show the corresponding x -integrated 1D density profiles. In (a), $U_{\uparrow\uparrow}/J_{\uparrow}$ is held at ~ 5.8 . In (b), $U_{\uparrow\uparrow}/J_{\uparrow}$ is ramped from ~ 5.8 to ~ 1.7 within 2 ms and held there for 16 ms before releasing the cloud from the lattice. This ramp corresponds to the green arrow in Fig. 6.3. In (c), $U_{\uparrow\uparrow}/J_{\uparrow}$ is ramped as in (b) and subsequently ramped back to $U_{\uparrow\uparrow}/J_{\uparrow} \sim 5.8$ before release from the lattice corresponding to the red curved arrow in Fig. 6.3. The decrease in the peak density $n_{\uparrow}(k=0)$ from (a) to (b) is a possible signature for a phase transition from a superfluid to a localized state. However, in (c) after a round trip, the initial peak density is not restored and thus a clear proof for localization is missing.

linearly within 2 ms to a value B_{hold} and hold it subsequently for a time of $t_{\text{hold}} = 16$ ms. For $B_{\text{hold}} - B_{\text{pole}} \sim \Delta B$, $a/a_{bg} \sim 0$ and $U_{\uparrow\uparrow}/J_{\uparrow} \sim 0$. Here, the mobile particles are expected to be localized. This ramp is indicated by the green arrow in the phase diagram of Fig. 6.3(b). As a third ramping scheme, we employ a timing sequence, where the magnetic field is ramped as in the latter scheme but subsequently ramped back linearly to its initial value B_{init} within 2 ms. For this ramp the system is expected to undergo a round-trip in the phase diagram from a superfluid to a localized phase and then back to a superfluid, as indicated by the red curved arrow in Fig. 6.3(b).

After the magnetic field ramp, all trapping potentials are switched off simultaneously and a time-of-flight image with Stern-Gerlach separation is taken. The peak density $n_{\uparrow}(k=0)$ in time-of-flight images serves as an indication for the corresponding quantum phase of the mobile species after each ramping scheme.

Typical time-of-flight images are shown in Fig. 6.7 along with the corresponding x -integrated 1D density profiles. The images were taken after an expansion time of 7 ms. In (a), we employ no magnetic field ramp, holding the magnetic field at B_{init} corresponding to $a/a_{bg} \sim 0.9$ and $U_{\uparrow\uparrow}/J_{\uparrow} = 5.7$. The high peak density $n_{\uparrow}(k=0)$ indicates that the

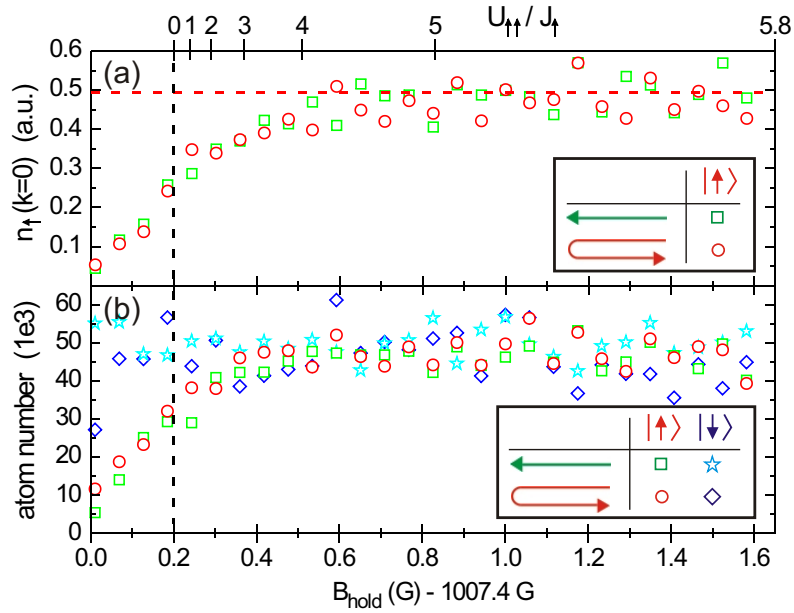


Figure 6.8.: Particle loss causes problems in our localization experiments. (a) $n_{\uparrow}(k=0)$ as a function of B_{hold} . Green squares were recorded with a magnetic field ramp as in Fig. 6.7(b). The decrease in $n_{\uparrow}(k=0)$ for a decrease in $U_{\uparrow\uparrow}/J_{\uparrow}$ is expected. Red circles were recorded with a magnetic field ramp as in Fig. 6.7(c). Ideally, these data should fall onto the red dashed line. (b) The number of frozen particles stays constant (cyan star for \leftarrow and blue diamond for \rightarrow), whereas the number of mobile particles shows a disastrous decrease (green squares for \leftarrow and red circles for \rightarrow). We suspect, that this loss results from bound-to-bound transitions.

mobile species is in the superfluid phase. In (b), the magnetic field is decreased from B_{init} to $B_{\text{hold}} = 1007.67$ G resulting in $a/a_{bg} \sim 1/4$ and $U_{\uparrow\uparrow}/J_{\uparrow} = 1.7$. The decrease of $n_{\uparrow}(k=0)$ might indicate that the mobile particles are localized. In order to exclude other effects like heating or particle loss as possible reasons for the decrease in $n_{\uparrow}(k=0)$, we perform the third ramping scheme, where B is ramped from B_{init} to B_{hold} as in (b) and subsequently re-increased to B_{init} . Results are shown in Fig. 6.7(c). A restoration of the peak density to its initial value from (a) indicated by the red dashed line, however, is not observed and a proof for localization is missing.

We aggressively explored the parameter space in our experiment changing the lattice depth along z , the total particle number, the ratio between the particle numbers in the mobile and the frozen species, and the parameters of the timing sequence. Nonetheless, a restoration of the peak density after a round trip in the phase diagram could not be observed.

We think that the dominant reason for the non-restoration of the initial peak density is most likely particle loss. In Fig. 6.8(a), $n_{\uparrow}(k=0)$ is shown as a function of B_{hold} for the same experiment as in Fig. 6.7. Green squares and red circles correspond to the ramping schemes as in Fig. 6.7(b) and (c), respectively. As in Fig. 6.7(b) and (c), the peak density is reduced when the Feshbach resonance is approached, and it is not restored

in a round-trip.

Fig. 6.8(b) displays the atom numbers of the mobile and the frozen species for the same measurements as in Fig. 6.8(a). If B approaches the Feshbach resonance, the number of frozen atoms stays constant whereas the number of mobile atoms decreases. We observed in an independent measurement that no loss occurs if the ~ 785 nm light is absent. We thus face a light-induced loss mechanism for the mobile species near the Feshbach resonance.

These characteristics of the loss suggest³ that it is due to a bound-to-bound transition driven by the ~ 785 nm light, as discussed in Chapter 5. Using Eqs. (5.16) and (5.17), we now estimate the resulting two-body loss. Based on Tab. 5.1 and Sec. 5.3, we assume $|d_{eg}|/(ea_0) = 0.3$, $\gamma_e = 2\pi \times 5$ MHz, and $\alpha/(2\pi) = 1.8$ mHz cm^{3/2}. A traveling-wave laser power of 1.8 mW as applied in Fig. 6.8 yields $\Omega_R/(2\pi) = 42$ MHz at an antinode of the standing wave. A comparison with data from the Heinzen group [Tsa08] shows that the ~ 785 nm light is detuned by $\Delta_L/(2\pi) \sim +3$ GHz and $\Delta_L/(2\pi) \sim -60$ GHz from the barycenters of the two closest vibrational levels of the 1_g molecular potential. We neglect the existence of the vibrational levels of the 0_u^+ and the 2_u molecular potentials. Furthermore, we guess that each vibrational level supports 10 hyperfine states that all contribute equally to the bound-to-bound loss. We find⁴ $K_2 \sim 1 \times 10^{-13}$ cm³/s at $B = 1007.60$ G. For a density of 8.3×10^{13} cm⁻³ and $t_{\text{hold}} = 16$ ms we thus estimate a loss of $N_{\text{loss}}/N_{\text{init}} \sim 0.2$. Given how coarsely the number and strengths of the lines were estimated, the agreement with the experimentally observed loss of $N_{\text{loss}}/N_{\text{init}} \sim 0.4$ in Fig. 6.8(b) is reasonable.

We tried to reduce the loss by trying out a variety of other light wavelengths. Unfortunately, this was unsuccessful. We discuss two examples here. First, we tried a frequency difference of +12 GHz relative to the previous data set, thus increasing the smallest detuning to a 1_g state by a factor of ~ 5 . We would expect this to reduce K_2 by a factor of ~ 25 , but we observed no noticeable change of the loss in the experiment.

In a second example, we chose $\lambda_z = 786.093$ nm, which is near the other end of the wavelength range that is useful for our experiment, see Sec. 6.1.3. The experimental sequence was otherwise identical to Fig. 6.8, except that we used a 30 ms ramp up time for the z lattice beam. Results are depicted in Fig. 6.9. For this wavelength, we expect detunings of $\Delta_L/(2\pi) \sim -42$ GHz and $\Delta_L/(2\pi) \sim +47$ GHz from the two closest vibrational levels of the 1_g molecular potential. Unfortunately, the loss in Fig. 6.9(b) is approximately as bad as in Fig. 6.8(b).

It is conceivable, at least in principle, that the 0_u^+ and 2_g potentials are responsible for the observed excess loss, but it would be a rather strange coincidence if all the wavelengths we tried out would have happened to lie close to such excited states. The physical origin of the observed loss is thus not quite clear. This problem might be circumvented by

³The loss cannot be attributed to photoassociation which is essentially independent of B for large detuning, see Eqs. (5.4b) and (5.14b).

⁴In principle, fast two-body loss might compromise the tunability of $\text{Re}(a)$, see Fig. 5.2. But according to Eq. (5.9b) the value of K_2 corresponds to $\text{Im}(a)/a_{\text{bg}} \sim -1 \times 10^{-3}$ which has little effect on the tunability of $\text{Re}(a)$.

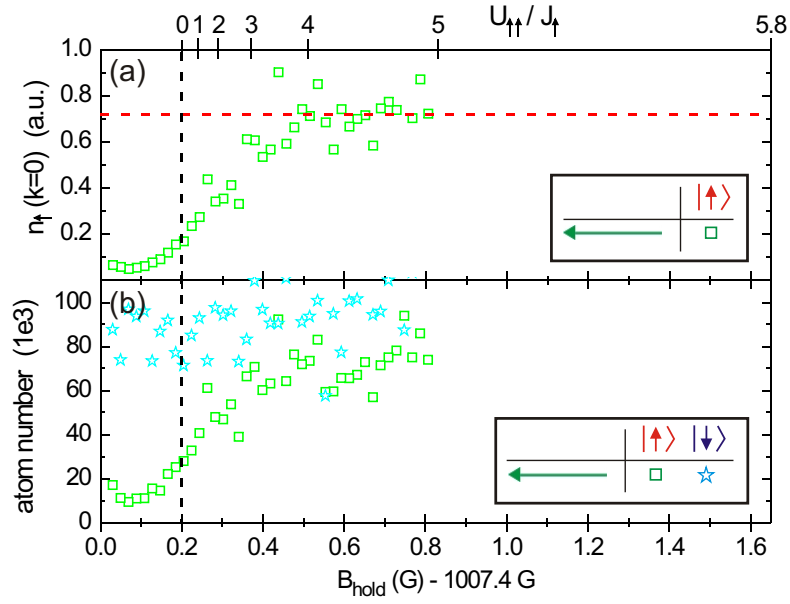


Figure 6.9.: Attempt to reduce particle loss by choosing a wavelength λ_z that is much further detuned from the closest bound-to-bound transition. (a) $n_{\uparrow}(k=0)$ as a function of B_{hold} . Same behavior as in Fig. 6.8(a). (b) Again, the number of frozen particles stays constant (cyan star for \leftarrow), whereas the number of mobile particles shows a disastrous decrease (green squares for \leftarrow).

replacing the mobile species by another chemical element, isotope, or internal species in future experiments, but this is beyond the scope of the present thesis.

7. Outlook

Interaction control of interatomic properties has a substantial impact in the field of ultracold quantum gases. The experiments described in this thesis reveal important aspects of both interacting ultracold atoms and molecules and offer valuable techniques that are relevant for further experiments.

The preparation of a quantum state with exactly one molecule at each site of an optical lattice [Vol06] might contribute to the creation of a quantum register with single polar molecules on single lattice sites. With a long-range dipole-dipole interaction between the polar molecules, such a register might bear great potential for applications in quantum simulations and quantum information processing [DeM02, Lee05, And06, Gór02, Mic06, Bar06]. Beside this, our quantum state of molecules serves as a good starting point to transfer molecules into their internal ground state by applying a sequence of Raman transitions. An absence of inelastic interactions would then allow to ramp down the optical lattice and to create a BEC of molecules in the internal ground state [Jak02].

Our experiment on coherent oscillations between atom-pairs and molecules [Sya07] demonstrates how atomic scattering properties can be inferred from a frequency measurement. Since frequencies can be measured with high precision, this technique offers prospects in high-precision measurements, e.g. in experiments searching for temporal drifts of fundamental constants [Chi06]. Additionally, the production of a coherent atom-molecule superposition state with controllable amplitude and phase opens up new possibilities for quantum simulations [Ess03].

Our observation that an increased loss coefficient can slow down the actual loss from the correlated many-body system of molecules [Sya08b] could be used to increase the lifetime of other systems that suffer from loss by drastically increasing the loss coefficient, e.g. using photoassociation or Feshbach resonances. The demonstration that dissipation can be used to reach the strongly correlated regime may pave the way for the observation of spin liquid behavior or topological effects [Sac99, Wen04].

The experimental progress towards localization of matter waves in a disorder potential created by an impurity species can serve as a starting point for future experiments, where the rich variety of new quantum phases can be explored [Fis89, Ros06b, Hor07].

Finally, the optical control of a magnetic Feshbach resonance presented in this thesis [Bau09b, Bau09a] demonstrates how the great potential of Feshbach resonances can be further exploited in future experiments. Light patterns created by holographic masks could serve as a tool for changing the scattering length of ultracold atoms on very short time and length scales. This could be used for a variety of applications, such as the investigation of the bosonic analog of Andreev reflection at a normal-superfluid interface [Zap09], the simulation of the physics of black holes [Gar00, Car08, Lah09], the controlled

creation of solitons [RV05], studies of the collapse of a BEC in an unusual regime [Don06], and the simulation of certain Hamiltonians in which the scattering length needs to be different at different sites of an optical lattice [Abd08, Den08]. Moreover, in combination with our technique to create a state with exactly two atoms per lattice site [Vol06], one could associate molecules at every second lattice site, thus producing a quantum state which resembles that of a supersolid [Isk09, Kei09]. Furthermore, if a spatially random light intensity pattern is applied, the scattering length would vary randomly with position which might give rise to new quantum phases of the atomic gas. A further example is to shift one Feshbach resonance on top of another to explore the coupling between the two. Another possible application for the manipulation of the scattering length with light exists in gases consisting of a mixture of different species or spin states. With our technique one could tune the various scattering lengths in such systems independently. Finally, with our scheme it should be possible to change the interaction energy of a whole sample of ultracold atoms inside a cavity [Bre07, Col07, Bre08] with a single photon.

A. ac-Stark Shift for an Alkali Atom in a Magnetic Field

In this Appendix, we calculate the ac-Stark shift for an alkali atom caused by a light field in the presence of a magnetic field. We assume that the ac-Stark shift is much smaller than the energy splittings within the ground state manifold due to the hyperfine interaction and/or the magnetic field. Hence, we first diagonalize the sum of the hyperfine Hamiltonian and the magnetic field Hamiltonian in Sec. A.1. As a second step, the ac-Stark shift of the light field is treated as a weak perturbation in Sec. A.2. Throughout this Appendix, we consider an alkali atom in the ground state $^2S_{1/2}$, where the ac-Stark shift results from transitions to excited states $^2P_{1/2}$ and $^2P_{3/2}$.

A.1. An Atom with Hyperfine Structure in an External Magnetic Field

In an alkali atom, the ground state is typically split into a manifold of substates characterized by the quantum numbers F and m_F , see Sec. 6.1.3. We assume that an external magnetic field is applied along the z axis, $\vec{B} = B\vec{e}_z$. As B increases, the ground state manifold undergoes a crossover from the Zeeman regime with good quantum numbers F , m_F to the Paschen Back regime with good quantum numbers m_J , m_I . We are particularly interested in the intermediate regime, where none of these quantum numbers are good.

The Hamiltonian for an atom with hyperfine structure in an external magnetic field B is [Ram56]

$$H = \frac{a}{\hbar^2} \vec{J} \cdot \vec{I} + \frac{\mu_B}{\hbar} B (g_J J_z + g_I I_z), \quad (\text{A.1})$$

where a is the hyperfine coupling constant, which is proportional to the energy splitting of the two hyperfine ground states. μ_B is the Bohr magneton. g_J and g_I are the Landé factors of the valence electron and the nucleus¹, respectively.

In the following, we calculate the eigenstates of this Hamiltonian. The magnetic field interaction is diagonal in the basis $|J, m_J, I, m_I\rangle$, whereas the hyperfine interaction is diagonal in the basis $|J, I, F, m_F\rangle$. As $m_J + m_I = m_F$, only states $|J, m_J, I, m_I\rangle$ with the same value of m_F are coupled by the hyperfine interaction. For values $m_F = \pm(I + 1/2)$, there exists only one state each. These so-called stretched states are therefore energy eigenstates at all values of B . Hence, we restrict the following considerations to the

¹For ^{87}Rb , this sign convention yields $a > 0$ and $g_I < 0$, see Tab. A.1. For other atoms, a and g_I can have either sign.

nontrivial case $|m_F| < I + 1/2$. For a given value of m_F , we choose the basis $\{|m_J = +1/2, m_I = m_F - 1/2\rangle, |m_J = -1/2, m_I = m_F + 1/2\rangle\}$ for a matrix representation.

According to Ref. [Ram56], the Hamiltonian in this subspace for a given m_F can be written as

$$\frac{H}{\hbar\omega_{HFS}} = \varphi \begin{pmatrix} 1 & 0 \\ 0 & 1 \end{pmatrix} + \frac{1}{2}(\alpha + \chi) \begin{pmatrix} 1 & 0 \\ 0 & -1 \end{pmatrix} + \frac{1}{2}\sqrt{1 - \alpha^2} \begin{pmatrix} 0 & 1 \\ 1 & 0 \end{pmatrix}, \quad (\text{A.2})$$

where we abbreviate the hyperfine splitting² $\hbar\omega_{HFS} = a(I + \frac{1}{2})$ and

$$\alpha = \frac{m_F}{I + \frac{1}{2}} \quad (\text{A.3a})$$

$$\chi = (g_J - g_I) \frac{\mu_B B}{\hbar\omega_{HFS}} \quad (\text{A.3b})$$

$$\varphi = -\frac{1}{2(2I + 1)} + g_I m_F \frac{\mu_B B}{\hbar\omega_{HFS}}. \quad (\text{A.3c})$$

In order to diagonalize the two-level Hamiltonian in Eq. (A.2), we define an angle θ with $0 \leq \theta \leq \pi$ by

$$\cos \theta = \frac{\alpha + \chi}{\sqrt{1 + 2\alpha\chi + \chi^2}}. \quad (\text{A.4})$$

One can show that the energy eigenstates are

$$|g\rangle_{F=I+\frac{1}{2}} = \begin{pmatrix} \cos \frac{\theta}{2} \\ \sin \frac{\theta}{2} \end{pmatrix} \quad \text{and} \quad |g\rangle_{F=I-\frac{1}{2}} = \begin{pmatrix} -\sin \frac{\theta}{2} \\ \cos \frac{\theta}{2} \end{pmatrix}, \quad (\text{A.5})$$

where the subscript $F = I \pm 1/2$ indicates to which hyperfine quantum number the state is adiabatically connected at $B = 0$. The energy eigenvalues are given by the Breit-Rabi formula [Bre31, Ram56]

$$E_{\pm} = \hbar\omega_{HFS} \left(\varphi \pm \frac{1}{2} \sqrt{1 + 2\alpha\chi + \chi^2} \right). \quad (\text{A.6})$$

Our experiment is performed with ⁸⁷Rb. The relevant parameters of this isotope are listed in Tab. A.1.

A.2. Zeeman State Dependent ac-Stark Shift

If an alkali atom is illuminated with far-detuned light, a ground state $|g\rangle$ will experience an ac-Stark shift [Pet02]

$$\Delta E = \sum_e \frac{1}{4\hbar\Delta_{eg}} \left| \langle e | \vec{d} \cdot \vec{E} | g \rangle \right|^2. \quad (\text{A.7})$$

²Note that ω_{HFS} can be positive or negative.

hyperfine splitting ω_{HFS}	: $2\pi \cdot 6.834\,682\,610\,904\,29$ (9) GHz	[Biz99]
electron Landé-factor g_J	: 2.002 331 12 (20)	[Ari77]
nuclear Landé-factor g_I	: $-0.000\,995\,141\,49$ (90)	[Whi68]
nuclear spin I	: $3/2$	[Ari77]
Bohr magneton μ_B/h	: $1.399\,624\,604$ (35) MHz/G	[Moh08]

Table A.1.: Parameters of the ground state of ^{87}Rb .

Here, the electric field of the light has the form $\vec{\mathcal{E}} = \vec{E} \cos(\omega t)$, \vec{d} is the electric dipole moment, and $\Delta_{eg} = \omega - \omega_{eg}$ is the detuning from the atomic resonance ω_{eg} . The sum extends over all excited states $|e\rangle$.

It is convenient to introduce the spherical tensor components of any vector \vec{v} [Edm63]

$$v_{\pm 1}^{(1)} = \frac{1}{\sqrt{2}} (\mp v_x - i v_y), \quad v_0^{(1)} = v_z. \quad (\text{A.8})$$

Hence, $\vec{d} \cdot \vec{E} = -d_{-1}^{(1)} E_{-1}^{(1)} - d_{-1}^{(1)} E_1^{(1)} + d_0^{(1)} E_0^{(1)}$. We assume that the light contains only one spherical tensor component $E_{-q}^{(1)}$ with $q = -1, 0$, or 1 . These polarizations are called σ^- , π , and σ^+ , respectively.

We assume that the light field is weak enough not to induce considerable mixing between the ground states and that the overall detuning from the excited states is much larger than all hyperfine splittings. Then $\Delta_{eg} = \Delta_{J'}$ depends only on $J' \in \{1/2, 3/2\}$. The nuclear spin depends on the internal structure of the nucleus and is not changed by the light field ($I = I'$). Hence, Eq. (A.7) can be written as

$$\Delta E = \sum_{J'} \frac{|E_{-q}^{(1)}|^2}{4\hbar\Delta_{J'}} \sum_{m'_J, m'_I} |\langle J', m'_J, I, m'_I | d_q^{(1)} | g \rangle|^2. \quad (\text{A.9})$$

Now we expand $|g\rangle$ in the $|J, m_J, I, m_I\rangle$ basis and use that there is only one value each for J and I , so that we do not have to sum over J, I . Hence,

$$\Delta E = \sum_{J'} \frac{|E_{-q}^{(1)}|^2}{4\hbar\Delta_{J'}} \sum_{m'_J, m'_I} \left| \sum_{m_J, m_I} \langle J', m'_J, I, m'_I | d_q^{(1)} | J, m_J, I, m_I \rangle \langle J, m_J, I, m_I | g \rangle \right|^2 \quad (\text{A.10})$$

As we consider only electric dipole transitions, $m'_I = m_I$. Moreover, the fact that $d_q^{(1)}$ is a spherical tensor operator implies $m'_J = m_J + q$. Hence

$$\langle J', m'_J, I, m'_I | d_q^{(1)} | J, m_J, I, m_I \rangle = \langle J', m'_J | d_q^{(1)} | J, m_J \rangle \delta_{m'_J, m_J+q} \delta_{m'_I, m_I}. \quad (\text{A.11})$$

We use the Kronecker symbols to collapse the sums over m_J, m_I in Eq. (A.10). Subsequently, we relabel the summation indices $m_J = m'_J - q$ and $m'_I = m_I$, and obtain

$$\Delta E = \sum_{J'} \frac{|E_{-q}^{(1)}|^2}{4\hbar\Delta_{J'}} \sum_{m_J, m_I} |\langle J', m_J + q | d_q^{(1)} | J, m_J \rangle \langle J, m_J, I, m_I | g \rangle|^2. \quad (\text{A.12})$$

	$m_F = -2$	$m_F = -1$	$m_F = 0$	$m_F = +1$	$m_F = +2$
$F = 2$	-1	-0.099821	+0.381819	+0.725569	+1
$F = 1$	-	+0.099821	-0.381819	-0.725569	-

Table A.2.: Values of β for the ground state manifold in ^{87}Rb at $B = 1007$ G calculated from Eqs. (A.3), (A.4), and (A.15).

The dipole matrix elements for the $L = 0 \leftrightarrow L' = 1$ transitions with $S = S' = 1/2$ in the $|J, m_J\rangle$ basis are given by [Met99, Rot59]

$$D_1\text{-line: } \langle J' = 1/2, m_J + q | d_q^{(1)} | J = 1/2, m_J \rangle = d_{cyc} (-1)^{3/2 - m_J} \sqrt{\frac{1 - 2m_J q}{3}} \quad (\text{A.13a})$$

$$D_2\text{-line: } \langle J' = 3/2, m_J + q | d_q^{(1)} | J = 1/2, m_J \rangle = d_{cyc} \sqrt{\frac{2 + 2m_J q}{3}}. \quad (\text{A.13b})$$

where d_{cyc} denotes the dipole matrix element on the cycling transition $|F = m_F = I + 1/2\rangle \leftrightarrow |F' = m'_F = I + 3/2\rangle$. Using Eqs. (A.5), (A.12), and (A.13), we obtain the ac-Stark shift

$$\Delta E = \Delta E_{1/2}^{cyc} \frac{1 - \beta q}{3} + \Delta E_{3/2}^{cyc} \frac{2 + \beta q}{3} \quad (\text{A.14})$$

with $\Delta E_{J'}^{cyc} = |E_{-q}^{(1)} d_{cyc}|^2 / (4\hbar\Delta_{J'})$ and

$$\beta = \pm \cos \theta \quad \text{for states adiabatically connected to } F = I \pm \frac{1}{2} \quad (\text{A.15})$$

for $|m_F| < I + 1/2$ and $\beta = \pm 1$ for $m_F = \pm(I + 1/2)$. For $B = 0$, Eq. (A.4) and (A.15) fields $\beta = \pm\alpha$ so that Eq. (A.14) reproduces Eq. (6.2). Our experiment is performed with ^{87}Rb at $B \sim 1007$ G. The resulting values for β at $B = 1007$ G are given in Tab. A.2.

Bibliography

- [Abd08] F. K. Abdullaev, A. Gammal, M. Salerno, and L. Tomio. Localized modes of binary mixtures of Bose-Einstein condensates in nonlinear optical lattices. *Phys. Rev. A* 77, 023615, 2008.
- [Akk07] E. Akkermans and G. Montambaux. *Mesoscopic Physics of Electrons and Photons*. Cambridge Univ. Press, 2007.
- [And58] P. W. Anderson. Absence of diffusion in certain random lattices. *Phys. Rev.* 109, 1492, 1958.
- [And87] P. W. Anderson. The resonating valence bond state in La_2CuO_4 and superconductivity. *Science* 235, 1196, 1987.
- [And95] M. H. Anderson, J. R. Ensher, M. R. Matthews, C. E. Wieman, and E. A. Cornell. Observation of Bose-Einstein condensation in a dilute atomic vapor. *Science* 269, 198, 1995.
- [And06] A. André, D. DeMille, J. M. Doyle, M. D. Lukin, S. E. Maxwell, P. Rabl, R. J. Schoelkopf, and P. Zoller. A coherent all-electrical interface between polar molecules and mesoscopic superconducting resonators. *Nature Phys.* 2, 636, 2006.
- [Ari77] E. Arimondo, M. Inguscio, and P. Violino. Experimental determinations of the hyperfine structure in alkali atoms. *Rev. Mod. Phys.* 49, 31, 1977.
- [AS05] J. R. Abo-Shaeer, D. E. Miller, J. K. Chin, K. Xu, T. Mukaiyama, and W. Ketterle. Coherent molecular optics using ultracold sodium dimers. *Phys. Rev. Lett.* 94, 040405, 2005.
- [Aue94] A. Auerbach. *Interacting Electrons and Quantum Magnetism*. Springer, Berlin, 1994.
- [Aut55] S. H. Autler and C. H. Townes. Stark effect in rapidly varying fields. *Phys. Rev.* 100, 703, 1955.
- [Bar04] M. Bartenstein, A. Altmeyer, S. Riedl, S. Jochim, C. Chin, J. Hecker-Denschlag, and R. Grimm. Crossover from a molecular Bose-Einstein condensate to a degenerate Fermi gas. *Phys. Rev. Lett.* 92, 120401, 2004.

- [Bar06] R. Barnett, D. Petrov, M. Lukin, and E. Demler. Quantum magnetism with multicomponent dipolar molecules in an optical lattice. *Phys. Rev. Lett.* 96, 190401, 2006.
- [Bau09a] D. M. Bauer, M. Lettner, C. Vo, G. Rempe, and S. Dürr. Combination of a magnetic Feshbach resonance and an optical bound-to-bound transition. *Phys. Rev. A* 79, 062713, 2009.
- [Bau09b] D. M. Bauer, M. Lettner, C. Vo, G. Rempe, and S. Dürr. Control of a magnetic Feshbach resonance with laser light. *Nature physics* 5, 339, 2009.
- [Bil08] J. Billy, V. Josse, Z. Zuo, A. Bernard, B. Hambrecht, P. Lugan, D. Clément, L. Sanchez-Palencia, P. Bouyer, and A. Aspect. Direct observation of Anderson localization of matter waves in a controlled disorder. *Nature* 453, 891, 2008.
- [Biz99] S. Bize, Y. Sortais, M. S. Santos, C. Mandache, A. Clairon, and C. Salomon. High-accuracy measurement of the ^{87}Rb ground-state hyperfine splitting in an atomic fountain. *Europhys. Lett.* 45, 558, 1999.
- [Blo05] I. Bloch. Ultracold quantum gases in optical lattices. *Nature Phys.* 1, 23, 2005.
- [Blo08] I. Bloch, J. Dalibard, and W. Zwerger. Many-body physics with ultracold gases. *Rev. Mod. Phys.* 80, 885, 2008.
- [Boh97] J. L. Bohn and P. S. Julienne. Prospects for influencing scattering lengths with far-off-resonant light. *Phys. Rev. A* 56, 1486, 1997.
- [Bra95] C. C. Bradley, C. A. Sackett, J. J. Tollett, and R. G. Hulet. Evidence of Bose-Einstein condensation in an atomic gas with attractive interactions. *Phys. Rev. Lett.* 75, 1687, 1995. Erratum *Phys. Rev. Lett.* 79, 1170, 1997.
- [Bre31] G. Breit and I. I. Rabi. Measurement of nuclear spin. *Phys. Rev.* 38, 2082, 1931.
- [Bre36] G. Breit and E. Wigner. Capture of slow neutrons. *Phys. Rev.* 49, 519, 1936.
- [Bre07] F. Brennecke, T. Donner, S. Ritter, T. Bourdel, M. Köhl, and T. Esslinger. Cavity QED with a Bose-Einstein condensate. *Nature* 450, 268, 2007.
- [Bre08] F. Brennecke, S. Ritter, T. Donner, and T. Esslinger. Cavity optomechanics with a Bose-Einstein condensate. *Science* 322, 235, 2008.
- [Bus98] T. Busch, B. G. Englert, K. Rzazewski, and M. Wilkens. Two cold atoms in a harmonic trap. *Found. Phys.* 28, 549, 1998.
- [Car08] I. Carusotto, S. Fagnocchi, A. Recati, R. Balbinot, and A. Fabbri. Numerical observation of Hawking radiation from acoustic black holes in atomic Bose-Einstein condensates. *New J. Phys.* 10, 103001, 2008.

- [Cas96] Y. Castin and R. Dum. Bose-Einstein condensates in time dependent traps. *Phys. Rev. Lett.* 77, 5315, 1996.
- [Cha00] A. A. Chabanov, M. Stoytchev, and A. Z. Genack. Statistical signatures of photon localization. *Nature* 404, 850, 2000.
- [Chi05] C. Chin, T. Kraemer, M. Mark, J. Herbig, P. Waldburger, H.-C. Nägerl, and R. Grimm. Observation of Feshbach-like resonances in collisions between ultracold molecules. *Phys. Rev. Lett.* 94, 123201, 2005.
- [Chi06] C. Chin and V. V. Flambaum. Enhanced sensitivity to fundamental constants in ultracold atomic and molecular systems near Feshbach resonances. *Phys. Rev. Lett.* 96, 230801, 2006.
- [Chi09] C. Chin, R. Grimm, P. Julienne, and E. Tiesinga. Feshbach resonances in ultracold gases. *arXiv:0812.1496v2* 2009.
- [Cho97] D. Cho. Analogous Zeeman effect from the tensor polarizability in alkali atoms. *J. Korean Phys. Soc.* 30, 373, 1997.
- [Clé05] D. Clément, A. F. Varón, M. Hugbart, J. A. Retter, P. Bouyer, L. Sanchez-Palencia, D. M. Gangardt, G. V. Shlyapnikov, and A. Aspect. Suppression of transport of an interacting elongated Bose-Einstein condensate in a random potential. *Phys. Rev. Lett.* 95, 170409, 2005.
- [Clé06] D. Clément, A. F. Varón, J. A. Retter, L. Sanchez-Palencia, A. Aspect, and P. Bouyer. Experimental study of the transport of coherent interacting matter-waves in a 1D random potential induced by laser speckle. *New J. Phys.* 8, 165, 2006.
- [Col07] Y. Colombe, T. Steinmetz, G. Dubois, F. Linke, D. Hunger, and J. Reichel. Strong atomfield coupling for Bose-Einstein condensates in an optical cavity on a chip. *Nature* 450, 272, 2007.
- [CT72] C. Cohen-Tannoudji and J. Dupont-Roc. Experimental study of Zeeman light shifts in weak magnetic fields. *Phys. Rev. A* 5, 968, 1972.
- [CT92] C. Cohen-Tannoudji, J. Dupont-Roc, and G. Grynberg. *Atom-Photon Interactions*. Wiley, New York, 1992.
- [Cub03] J. Cubizolles, T. Bourdel, S. J. J. M. F. Kokkelmans, G. V. Shlyapnikov, and C. Salomon. Production of long-lived ultracold Li₂ molecules from a Fermi gas. *Phys. Rev. Lett.* 91, 240401, 2003.
- [Dal91] R. Dalichaouch, J. P. Armstrong, S. Schultz, P. M. Platzman, and S. L. McCall. Microwave localization by two-dimensional random scattering. *Nature* 354, 53, 1991.

- [Dam03] B. Damski, J. Zakrzewski, L. Santos, P. Zoller, and M. Lewenstein. Atomic Bose and Anderson glasses in optical lattices. *Phys. Rev. Lett.* 91, 080403, 2003.
- [Dan] A. Danilova and J. H. Thywissen. Ultracold atom news. <http://ucan.physics.utoronto.ca>.
- [Dan08] J. G. Danzl, E. Haller, M. Gustavsson, M. J. Mark, R. Hart, N. Bouloufa, O. Dulieu, H. Ritsch, and H.-C. Nägerl. Quantum gas of deeply bound ground state molecules. *Science* 321, 1062, 2008.
- [Dav95] K. B. Davis, M.-O. Mewes, M. R. Andrews, N. J. van Druten, D. S. Durfee, D. M. Kurn, and W. Ketterle. Bose-Einstein condensation in a gas of sodium atoms. *Phys. Rev. Lett.* 75, 3969, 1995.
- [DeM02] D. DeMille. Quantum computation with trapped polar molecules. *Phys. Rev. Lett.* 88, 067901, 2002.
- [Den08] X.-L. Deng, D. Porras, and J. I. Cirac. Quantum phases of interacting phonons in ion traps. *Phys. Rev. A* 77, 033403, 2008.
- [Die07] D. Dietze. *Atom-Molekül Oszillationen in ^{87}Rb* . Diplomarbeit, Max-Planck-Institut für Quantenoptik, Garching, and Technische Universität München, 2007. Unpublished.
- [Don01] E. A. Donley, N. R. Claussen, S. L. Cornish, J. L. Roberts, E. A. Cornell, and C. E. Wieman. Dynamics of collapsing and exploding Bose-Einstein condensates. *Nature* 412, 295, 2001.
- [Don02] E. A. Donley, N. R. Claussen, S. T. Thompson, and C. E. Wieman. Atom-molecule coherence in a Bose-Einstein condensate. *Nature* 417, 529, 2002.
- [Don06] G. Dong, B. Hu, and W. Lu. Ground-state properties of a Bose-Einstein condensate tuned by a far-off-resonant optical field. *Phys. Rev. A* 74, 063601, 2006.
- [Dür04a] S. Dürr, T. Volz, A. Marte, and G. Rempe. Observation of molecules produced from a Bose-Einstein condensate. *Phys. Rev. Lett.* 92, 020406, 2004.
- [Dür04b] S. Dürr, T. Volz, and G. Rempe. Dissociation of ultracold molecules with Feshbach resonances. *Phys. Rev. A* 70, 031601, 2004.
- [Dür06] S. Dürr, T. Volz, N. Syassen, D. M. Bauer, E. Hansis, and G. Rempe. A Mott-like state of molecules. In C. Roos, H. Häffner, and R. Blatt, eds., *AIP Conf. Proc.*, volume 869, pages 278–283. AIP, 2006.
- [Dür08] S. Dürr, N. Syassen, D. M. Bauer, M. Lettner, T. Volz, D. Dietze, J. J. García-Ripoll, J. I. Cirac, and G. Rempe. A dissipative Tonks-Girardeau gas of molecules. In P. L. Gould, M. Rozman, and W. W. Smith, eds., *AIP Conf. Proc.*, pages 307–314. World Scientific, 2008.

- [Dür09] S. Dürr, J. J. García-Ripoll, N. Syassen, D. M. Bauer, M. Lettner, J. I. Cirac, and G. Rempe. Lieb-Liniger model of a dissipation-induced Tonks-Girardeau gas. *Phys. Rev. A* 79, 023614, 2009.
- [Edm63] A. R. Edmonds. *Angular Momentum in Quantum Mechanics*. University Press, Princeton, 1963.
- [Eno08] K. Enomoto, K. Kasa, M. Kitagawa, and Y. Takahashi. Optical Feshbach resonance using the intercombination transition. *Phys. Rev. Lett.* 101, 203201, 2008.
- [Ess03] T. Esslinger and K. Mølmer. Atoms and molecules in lattices: Bose-Einstein condensates built on a shared vacuum. *Phys. Rev. Lett.* 90, 160406, 2003.
- [Fal07] L. Fallani, J. E. Lye, V. Guarrera, C. Fort, and M. Inguscio. Ultracold atoms in a disordered crystal of light: Towards a Bose glass. *Phys. Rev. Lett.* 98, 130404, 2007.
- [Fat00] F. K. Fatemi, K. M. Jones, and P. D. Lett. Observation of optically induced Feshbach resonances in collisions of cold atoms. *Phys. Rev. Lett.* 85, 4462, 2000.
- [Fat08] M. Fattori, C. D’Errico, G. Roati, M. Zaccanti, M. Jona-Lasinio, M. Modugno, M. Inguscio, and G. Modugno. Atom interferometry with a weakly interacting Bose-Einstein condensate. *Phys. Rev. Lett.* 100, 080405, 2008.
- [Fed96] P. O. Fedichev, Y. Kagan, G. V. Shlyapnikov, and J. T. M. Walraven. Influence of nearly resonant light on the scattering length in low-temperature atomic gases. *Phys. Rev. Lett.* 77, 2913, 1996.
- [Fes93] H. A. Feshbach. *Theoretical Nuclear Physics, Nuclear Reactions*. Wiley, New York, 1993.
- [Fis89] M. P. A. Fisher, P. B. Weichmann, G. Grinstein, and D. S. Fisher. Boson localization and the superfluid-insulator transition. *Phys. Rev. B* 40, 546, 1989.
- [For05] C. Fort, L. Fallani, V. Guarrera, J. E. Lye, M. Modugno, D. S. Wiersma, and M. Inguscio. Effect of optical disorder and single defects on the expansion of a Bose-Einstein condensate in a one-dimensional waveguide. *Phys. Rev. Lett.* 95, 170410, 2005.
- [Gar00] L. J. Garay, J. R. Anglin, J. I. Cirac, and P. Zoller. Sonic analog of gravitational black holes in Bose-Einstein condensates. *Phys. Lett. Lett.* 85, 4643, 2000.
- [Gav05] U. Gavish and Y. Castin. Matter-wave localization in disordered cold atom lattices. *Phys. Rev. Lett.* 95, 020401, 2005.
- [Ger05] F. Gerbier, A. Widera, S. Fölling, O. Mandel, T. Gericke, and I. Bloch. Phase coherence of an atomic Mott insulator. *Phys. Rev. Lett.* 95, 050404, 2005.

- [Gim05] H. Gimperlein, S. Wessel, J. Schmiedmayer, and L. Santos. Ultracold atoms in optical lattices with random on-site interactions. *Phys. Rev. Lett.* 95, 170401, 2005.
- [Gir60] M. Girardeau. Relationship between systems of impenetrable bosons and fermions in one dimension. *J. Math. Phys.* 1, 516, 1960.
- [Gór02] K. Góral, L. Santos, and M. Lewenstein. Quantum phases of dipolar bosons in optical lattices. *Phys. Rev. Lett.* 88, 170406, 2002.
- [Gór04] K. Góral, T. Köhler, S. A. Gardiner, E. Tiesinga, and P. Julienne. Adiabatic association of ultracold molecules via magnetic-field tunable interactions. *J. Phys. B* 37, 3457, 2004.
- [GR09] J. J. García-Ripoll, S. Dürr, N. Syassen, D. M. Bauer, M. Lettner, G. Rempe, and J. I. Cirac. Dissipation-induced hard-core boson gas in an optical lattice. *New J. Phys.* 11, 013053, 2009.
- [Gre02] M. Greiner, O. Mandel, T. Esslinger, T. W. Hänsch, and I. Bloch. Quantum phase transition from a superfluid to a Mott insulator in a gas of ultracold atoms. *Nature* 415, 39, 2002.
- [Gre03] M. Greiner. *Ultracold Quantum Gases in Three-Dimensional Optical Lattice Potentials*. Ph.D. thesis, Ludwig-Maximilians-Universität, München, 2003.
- [Gri00] R. Grimm, M. Weidemüller, and Y. B. Ovchinnikov. Optical dipole traps for neutral atoms. In B. Bederson and H. Walther, eds., *Advances in Atomic, Molecular and Optical Physics*, volume 42, pages 95–170. Academic Press, San Diego, 2000.
- [Gus08] M. Gustavsson, E. Haller, M. J. Mark, J. G. Danzl, G. Rojas-Kopeinig, and H.-C. Nägerl. Control of interaction-induced dephasing of Bloch oscillations. *Phys. Rev. Lett* 100, 080404, 2008.
- [Ham09] C. D. Hamley, E. M. Bookjans, G. Behin-Aein, P. Ahmadi, and M. S. Chapman. Photoassociation spectroscopy of a spin-1 Bose-Einstein condensate. *Phys. Rev. A* 79, 023401, 2009.
- [Han06] E. Hansis. *Ultracold Molecules in an Optical Lattice*. Diplomarbeit, Max-Planck-Institut für Quantenoptik, Garching, and Technische Universität München, 2006.
- [HD02] J. Hecker-Denschlag, J. E. Simsarian, H. Häffner, C. McKenzie, A. Browaeys, D. Cho, K. Helmerson, S. L. Rolston, and W. D. Phillips. A Bose-Einstein condensate in an optical lattice. *J. Phys. B* 35, 3095, 2002.

- [Her03] J. Herbig, T. Kraemer, M. Mark, T. Weber, C. Chin, H.-C. Nägerl, and R. Grimm. Preparation of a pure molecular quantum gas. *Science* 301, 1510, 2003.
- [Hod05] E. Hodby, S. T. Thompson, C. A. Regal, M. Greiner, A. C. Wilson, D. S. Jin, E. A. Cornell, and C. E. Wieman. Production efficiency of ultracold Feshbach molecules in bosonic and fermionic systems. *Phys. Rev. Lett.* 94, 120402, 2005.
- [Hor07] B. Horstmann, J. I. Cirac, and T. Roscilde. Dynamics of localization phenomena for hard-core bosons on optical lattices. *Phys. Rev. A* 76, 043625, 2007.
- [Ino98] S. Inouye, M. R. Andrews, J. Stenger, H.-J. Miesner, D. M. Stamper-Kurn, and W. Ketterle. Observation of Feshbach resonances in a Bose-Einstein condensate. *Nature* 392, 151, 1998.
- [Isk09] M. Iskin and J. K. Freericks. Strong-coupling perturbation theory for the extended Bose-Hubbard model. *Phys. Rev. A* 79, 053634, 2009.
- [Jak98] D. Jaksch, C. Bruder, J. I. Cirac, C. W. Gardiner, and P. Zoller. Cold bosonic atoms in optical lattices. *Phys. Rev. Lett.* 81, 3108, 1998.
- [Jak02] D. Jaksch, V. Venturi, J. I. Cirac, C. J. Williams, and P. Zoller. Creation of a molecular condensate by dynamically melting a Mott insulator. *Phys. Rev. Lett.* 89, 040402, 2002.
- [Joa75] C. J. Joachain. *Quantum Collision Theory*. North-Holland, Amsterdam, 1975.
- [Joc03a] S. Jochim, M. Bartenstein, A. Altmeyer, G. Hendl, C. Chin, J. Hecker-Denschlag, and R. Grimm. Pure gas of optically trapped molecules created from fermionic atoms. *Phys. Rev. Lett.* 91, 240402, 2003.
- [Joc03b] S. Jochim, M. Bartenstein, A. Altmeyer, G. Hendl, S. Riedl, C. Chin, J. Hecker-Denschlag, and R. Grimm. Bose-Einstein condensation of molecules. *Science* 302, 2101, 2003.
- [Jon06] K. M. Jones, E. Tiesinga, P. D. Lett, and P. S. Julienne. Ultracold photoassociation spectroscopy: long-range molecules and atomic scattering. *Rev. Mod. Phys.* 78, 483, 2006.
- [Jun08] M. Junker, D. Dries, C. Welford, J. Hitchcock, Y. P. Chen, and R. G. Hulet. Photoassociation of a Bose-Einstein condensate near a Feshbach resonance. *Phys. Rev. Lett.* 101, 060406, 2008.
- [Kau09] A. M. Kaufman, R. P. Anderson, T. M. Hanna, E. Tiesinga, P. S. Julienne, and D. S. Hall. Radiofrequency dressing of multiple Feshbach resonances. *arXiv:0906.5587v1* 2009.

- [Kei09] T. Keilmann, I. Cirac, and T. Roscilde. Dynamical creation of a supersolid in asymmetric mixtures of bosons. *Phys. Rev. Lett.* 102, 255304, 2009.
- [Kem04] M. Kemmann, I. Mistrik, S. Nussmann, H. Helm, C. J. Williams, and P. S. Julienne. Near-threshold photoassociation of $^{87}\text{Rb}_2$. *Phys. Rev. A* 69, 022715, 2004.
- [Kin04] T. Kinoshita, T. Wenger, and D. S. Weiss. Observation of a one-dimensional Tonks-Girardeau gas. *Science* 305, 1125, 2004.
- [Kit03] A. Y. Kitaev. Fault-tolerant quantum computation by anyons. *Ann. Phys.* 303, 2, 2003.
- [Köh06] T. Köhler, K. Góral, and P. S. Julienne. Production of cold molecules via magnetically tunable Feshbach resonances. *Rev. Mod. Phys.* 78, 1311, 2006.
- [Kok] S. J. J. M. F. Kokkelmans. Personal communication.
- [Kra06] T. Kraemer, M. Mark, P. Waldburger, J. G. Danzl, C. Chin, B. Engeser, A. D. Lange, K. Pilch, A. Jaakkola, H.-C. Nägerl, and R. Grimm. Evidence for Efimov quantum states in an ultracold gas of caesium atoms. *Nature* 440, 315, 2006.
- [Kuh05] R. C. Kuhn, C. Miniatura, D. Delande, O. Sigwarth, and C. A. Müller. Localization of matter waves in two-dimensional disordered optical potentials. *Phys. Rev. Lett.* 95, 250403, 2005.
- [Lah07] T. Lahaye, T. Koch, B. Fröhlich, M. Fattori, J. Metz, A. Griesmaier, S. Giovanazzi, and T. Pfau. Strong dipolar effects in a quantum ferrofluid. *Nature* 448, 672, 2007.
- [Lah08] Y. Lahini, A. Avidan, F. Pozzi, M. Sorel, R. Morandotti, D. N. Christodoulides, and Y. Silberberg. Anderson localization and nonlinearity in one-dimensional disordered photonic lattices. *Phys. Rev. Lett.* 100, 013906, 2008.
- [Lah09] O. Lahav, A. Itah, A. Blumkin, C. Gordon, and J. Steinhauer. A sonic black hole in a density-inverted Bose-Einstein condensate. *arXiv:0906.1337v1* 2009.
- [Lee05] C. Lee and E. A. Ostrovskaya. Quantum computation with diatomic bits in optical lattices. *Phys. Rev. A* 72, 062321, 2005.
- [Lew07] M. Lewenstein, A. Sanpera, V. Ahufinger, B. Damski, A. Sen, and U. Sen. Ultracold atomic gases in optical lattices: mimicking condensed matter physics and beyond. *Adv. Phys.* 56, 243, 2007.
- [Lie63] E. H. Lieb and W. Liniger. Exact analysis of an interacting Bose gas. I. the general solution and the ground state. *Phys. Rev.* 130, 1605, 1963.

- [Lug07] P. Lugan, D. Clément, P. Bouyer, A. Aspect, M. Lewenstein, and L. Sanchez-Palencia. Ultracold Bose gases in 1D disorder: From Lifshits glass to Bose-Einstein condensate. *Phys. Rev. Lett.* 98, 170403, 2007.
- [Lye05] J. E. Lye, L. Fallani, M. Modugno, D. S. Wiersma, C. Fort, and M. Inguscio. Bose-Einstein condensate in a random potential. *Phys. Rev. Lett.* 95, 070401, 2005.
- [Lye07] J. E. Lye, L. Fallani, C. Fort, V. Guarrera, M. Modugno, D. S. Wiersma, and M. Inguscio. Effect of interactions on the localization of a Bose-Einstein condensate in a quasiperiodic lattice. *Phys. Rev. A* 75, 061603(R), 2007.
- [Mac08] M. Mackie, M. Fenty, D. Savage, and J. Kesselman. Cross-molecular coupling in combined photoassociation and Feshbach resonances. *Phys. Rev. Lett.* 101, 040401, 2008.
- [Mar98] M. Marinescu and L. You. Controlling atom-atom interaction at ultralow temperatures by dc electric fields. *Phys. Rev. Lett.* 81, 4596, 1998.
- [Mar02] A. Marte, T. Volz, J. Schuster, S. Dürr, G. Rempe, E. G. M. van Kempen, and B. J. Verhaar. Feshbach resonances in rubidium 87: Precision measurement and analysis. *Phys. Rev. Lett.* 89, 283202, 2002.
- [Mar03] A. Marte. *Feshbach-Resonanzen bei Stößen ultrakalter Rubidiumatome*. Ph.D. thesis, Max-Planck-Institut für Quantenoptik, Garching, and Technische Universität München, 2003.
- [Mar05] M. Mark, T. Kraemer, J. Herbig, C. Chin, H.-C. Nägerl, and R. Grimm. Efficient creation of molecules from a cesium Bose-Einstein condensate. *Europhys. Lett.* 69, 706, 2005.
- [Mas06] P. Massignan and Y. Castin. Three-dimensional strong localization of matter waves by scattering from atoms in a lattice with a confinement-induced resonance. *Phys. Rev. A* 74, 013616, 2006.
- [Met99] H. J. Metcalf and P. van der Straten. *Laser Cooling and Trapping*. Springer, Heidelberg, 1999.
- [Mic06] A. Micheli, G. K. Brennen, and P. Zoller. A toolbox for lattice-spin models with polar molecules. *Nature Phys.* 2, 341, 2006.
- [Mie96] F. H. Mies, C. J. Williams, P. S. Julienne, and M. Krauss. Estimating bounds on collisional relaxation rates of spin-polarized ^{87}Rb atoms at ultracold temperatures. *J. Res. NIST* 101, 521, 1996.
- [Mie00] F. H. Mies, E. Tiesinga, and P. S. Julienne. Manipulation of Feshbach resonances in ultracold atomic collisions using time-dependent magnetic fields. *Phys. Rev. A* 61, 022721, 2000.

- [Mil02] K. W. Miller, S. Dürr, and C. E. Wieman. rf-induced Sisyphus cooling in an optical dipole trap. *Phys. Rev. A* 66, 023406, 2002.
- [Mis77] B. Misra and E. C. G. Sudarshan. The Zeno's paradox in quantum theory. *J. Math. Phys.* 18, 756, 1977.
- [Moe95] A. J. Moerdijk, B. J. Verhaar, and A. Axelsson. Resonances in ultracold collisions of ${}^6\text{Li}$, ${}^7\text{Li}$, and ${}^{23}\text{Na}$. *Phys. Rev. A* 51, 4852, 1995.
- [Moe96] A. J. Moerdijk, B. J. Verhaar, and T. M. Nagtegaal. Collisions of dressed ground-state atoms. *Phys. Rev. A* 53, 4343, 1996.
- [Moh08] P. J. Mohr, B. N. Taylor, and D. B. Newell. CODATA recommended values of the fundamental physical constants: 2006. *Rev. Mod. Phys.* 80, 633, 2008.
- [Mor05] H. Moritz, T. Stöferle, K. Günter, M. Köhl, and T. Esslinger. Confinement induced molecules in a 1D Fermi gas. *Phys. Rev. Lett.* 94, 210401, 2005.
- [Muk04] T. Mukaiyama, J. R. Abo-Shaeer, K. Xu, J. K. Chin, and W. Ketterle. Dissociation and decay of ultracold Feshbach molecules. *Phys. Rev. Lett.* 92, 180402, 2004.
- [Näg08] H.-C. Nägerl. Personal communication, 2008.
- [Ni08] K.-K. Ni, S. Ospelkaus, M. H. G. de Miranda, A. Pe'er, B. Neyenhuis, J. J. Zirbel, S. Kotochigova, P. S. Julienne, D. S. Jin, and J. Ye. A high phase-space-density gas of polar molecules. *Science* 322, 231, 2008.
- [Osp06] C. Ospelkaus, S. Ospelkaus, L. Humbert, P. Ernst, K. Sengstock, and K. Bongs. Ultracold heteronuclear molecules in a 3D optical lattice. *Phys. Rev. Lett.* 97, 120402, 2006.
- [Pap06] S. B. Papp and C. E. Wieman. Observation of heteronuclear Feshbach molecules from a ${}^{85}\text{Rb}$ - ${}^{87}\text{Rb}$ gas. *Phys. Rev. Lett.* 97, 180404, 2006.
- [Par04] B. Paredes, A. Widera, V. Murg, O. Mandel, S. Fölling, I. Cirac, G. V. Shlyapnikov, T. W. Hänsch, and I. Bloch. Tonks-Girardeau gas of ultracold atoms in an optical lattice. *Nature* 429, 277, 2004.
- [Par05] B. Paredes, F. Verstraete, and J. I. Cirac. Exploiting quantum parallelism to simulate quantum random many-body systems. *Phys. Rev. Lett.* 95, 140501, 2005.
- [Pet02] C. J. Pethick and H. Smith. *Bose-Einstein Condensation in Dilute Gases*. Cambridge University Press, Cambridge, 2002.
- [Pet04] D. S. Petrov, C. Salomon, and G. V. Shlyapnikov. Weakly bound dimers of fermionic atoms. *Phys. Rev. Lett.* 93, 090404, 2004.

- [Pit03] L. Pitaevskii and S. Stringari. *Bose-Einstein Condensation*. Clarendon Press, Oxford, 2003.
- [Pol09] S. E. Pollack, D. Dries, M. Junker, Y. P. Chen, T. A. Corcovilos, and R. G. Hulet. Extreme tunability of interactions in a ^7Li Bose-Einstein condensate. *Phys. Rev. Lett.* 102, 090402, 2009.
- [Ram56] N. F. Ramsey. *Molecular Beams*. Oxford University Press, Oxford, 1956.
- [Reg03] C. A. Regal, C. Ticknor, J. L. Bohn, and D. S. Jin. Creation of ultracold molecules from a Fermi gas of atoms. *Nature* 424, 47, 2003.
- [Reg04a] C. A. Regal, M. Greiner, and D. S. Jin. Lifetime of molecule-atom mixtures near a Feshbach resonance in ^{40}K . *Phys. Rev. Lett.* 92, 083201, 2004.
- [Reg04b] C. A. Regal, M. Greiner, and D. S. Jin. Observation of resonance condensation of fermionic atom pairs. *Phys. Rev. Lett.* 92, 040403, 2004.
- [Roa08] G. Roati, C. D'Errico, L. Fallani, M. Fattori, C. Fort, M. Zaccanti, G. Modugno, M. Modugno, and M. Inguscio. Anderson localization of a non-interacting Bose-Einstein condensate. *Nature* 453, 895, 2008.
- [Rom04] T. Rom, T. Best, O. Mandel, A. Widera, M. Greiner, T. W. Hänsch, and I. Bloch. State selective production of molecules in optical lattices. *Phys. Rev. Lett.* 93, 073002, 2004.
- [Ros06a] T. Roscilde. Talk given at the APS March Meeting 2006, Baltimore, MD, March 13-17th, 2006.
- [Ros06b] T. Roscilde. Personal communication, 2006.
- [Ros07] T. Roscilde and J. I. Cirac. Quantum emulsion: A glassy phase of bosonic mixtures in optical lattices. *Phys. Rev. Lett.* 98, 190402, 2007.
- [Rot59] M. Rotenberg, R. Bivins, N. Metropolis, and J. K. Wooten. *The 3j and 6j Symbols*. Technology Press, Cambridge, 1959.
- [Rot03] R. Roth and K. Burnett. Phase diagram of bosonic atoms in two-color superlattices. *Phys. Rev. A* 68, 023604, 2003.
- [RV05] M. I. Rodas-Verde, H. Michinel, and V. M. Pérez-García. Controllable soliton emission from a Bose-Einstein condensate. *Phys. Rev. Lett.* 95, 153903, 2005.
- [Sac99] S. Sachdev. *Quantum Phase Transitions*. Cambridge University Press, Cambridge, 1999.
- [Sag05] J. M. Sage, S. Sainis, T. Bergeman, and D. DeMille. Optical production of ultracold polar molecules. *Phys. Rev. Lett.* 94, 203001, 2005.

- [San04] A. Sanpera, A. Kantian, L. Sanchez-Palencia, J. Zakrzewski, and M. Lewenstein. Atomic Fermi-Bose mixtures in inhomogeneous and random lattices: From Fermi glass to quantum spin glass and quantum percolation. *Phys. Rev. Lett.* 93, 040401, 2004.
- [Sav97] T. A. Savard, K. M. O'Hara, and J. E. Thomas. Laser-noise-induced heating in far-off resonance optical traps. *Phys. Rev. A* 56, R1095, 1997.
- [Sca91] R. T. Scalettar, G. G. Batrouni, and G. T. Zimanyi. Localization in interacting, disordered, Bose systems. *Phys. Rev. Lett.* 66, 3144, 1991.
- [Sch98] A. E. Schwabl. *Quantenmechanik*. Springer Verlag, 1998.
- [Sch99] F. Scheffold, R. Lenke, R. Tweert, and G. Maret. Localization or classical diffusion of light? *Nature* 398, 206, 1999.
- [Sch02] J. Schuster. *Stoßlawinen in einem Bose-Einstein-Kondensat*. Ph.D. thesis, Max-Planck-Institut für Quantenoptik, Garching, and Universität Konstanz, 2002.
- [Sch05] T. Schulte, S. Drenkelforth, J. Kruse, W. Ertmer, J. Arlt, K. Sacha, J. Zakrzewski, and M. Lewenstein. Routes towards Anderson-like localization of Bose-Einstein condensates in disordered optical lattices. *Phys. Rev. Lett.* 95, 170411, 2005.
- [Sch06] T. Schulte, S. Drenkelforth, J. Kruse, R. Tiemeyer, K. Sacha, J. Zakrzewski, M. Lewenstein, W. Ertmer, and J. J. Arlt. Analysis of localization phenomena in weakly interacting disordered lattice gases. *New J. Phys.* 8, 230, 2006.
- [Sch07] T. Schwartz, G. Bartal, S. Fishman, and M. Segev. Transport and Anderson localization in disordered two-dimensional photonic lattices. *Nature* 446, 52, 2007.
- [Sen07] P. Sengupta, A. Raghavan, and S. Haas. Disorder-enhanced phase coherence in trapped bosons on optical lattices. *New J. Phys.* 9, 103, 2007.
- [Sie86] A. E. Siegman. *Lasers*. University Science Books, Sausalito, 1986.
- [Smi07] G. Smirne, R. M. Godun, D. Cassettari, V. Boyer, C. J. Foot, T. Volz, N. Syassen, S. Dürr, G. Rempe, M. D. Lee, K. Góral, and T. Köhler. Collisional relaxation of Feshbach molecules and three-body recombination in ^{87}Rb Bose-Einstein condensates. *Phys. Rev. A* 75, 020702, 2007.
- [SP07] L. Sanchez-Palencia, D. Clément, P. Lugan, P. Bouyer, G. V. Shlyapnikov, and A. Aspect. Anderson localization of expanding Bose-Einstein condensates in random potentials. *Phys. Rev. Lett.* 98, 210401, 2007.

- [Ste08] D. A. Steck. Paralyzed by disorder. *Nature* 453, 866, 2008.
- [Sto88] H. T. C. Stoof, J. M. V. A. Koelman, and B. J. Verhaar. Spin-exchange and dipole relaxation rates in atomic hydrogen: Rigorous and simplified calculations. *Phys. Rev. B* 38, 4688, 1988.
- [Sto99] H. L. Stormer, D. C. Tsui, and A. C. Gossard. The fractional quantum Hall effect. *Rev. Mod. Phys.* 71, S298, 1999.
- [Stö04] T. Stöferle, H. Moritz, C. Schori, M. Köhl, and T. Esslinger. Transition from a strongly interacting 1D superfluid to a Mott insulator. *Phys. Rev. Lett.* 92, 130403, 2004.
- [Stö06] M. Störzer, P. Gross, C. M. Aegerter, and G. Maret. Observation of the critical regime near Anderson localization of light. *Phys. Rev. Lett.* 96, 063904, 2006.
- [Str03] K. E. Strecker, G. B. Partridge, and R. G. Hulet. Conversion of an atomic Fermi gas to a long-lived molecular Bose gas. *Phys. Rev. Lett.* 91, 080406, 2003.
- [Stw76] W. C. Stwalley. Stability of spin-aligned hydrogen at low temperatures and high magnetic fields: New field-dependent scattering resonances and predissociations. *Phys. Rev. Lett.* 37, 1628, 1976.
- [Sya06] N. Syassen, T. Volz, S. Teichmann, S. Dürr, and G. Rempe. Collisional decay of ^{87}Rb Feshbach molecules at 1005.8 G. *Phys. Rev. A* 74, 062706, 2006.
- [Sya07] N. Syassen, D. M. Bauer, M. Lettner, D. Dietze, T. Volz, S. Dürr, and G. Rempe. Atom-molecule Rabi oscillations in a Mott insulator. *Phys. Rev. Lett.* 99, 033201, 2007.
- [Sya08a] N. Syassen. *Interacting Feshbach Molecules*. Ph.d. thesis, Max-Planck-Institut für Quantenoptik, Garching, and Technische Universität München, 2008.
- [Sya08b] N. Syassen, D. M. Bauer, M. Lettner, T. Volz, D. Dietze, J. J. García-Ripoll, J. I. Cirac, G. Rempe, and S. Dürr. Strong dissipation inhibits losses and induces correlations in cold molecular gases. *Science* 320, 1329, 2008.
- [Tay72] J. R. Taylor. *Scattering Theory*. Wiley, New York, 1972.
- [Tha05] G. Thalhammer, M. Theis, K. Winkler, R. Grimm, and J. Hecker-Denschlag. Inducing an optical Feshbach resonance via stimulated Raman coupling. *Phys. Rev. A* 71, 033403, 2005.
- [Tha06] G. Thalhammer, K. Winkler, F. Lang, S. Schmid, R. Grimm, and J. Hecker-Denschlag. Long-lived Feshbach molecules in a three-dimensional optical lattice. *Phys. Rev. Lett.* 96, 050402, 2006.

- [The04] M. Theis, G. Thalhammer, K. Winkler, M. Hellwig, G. Ruff, R. Grimm, and J. Hecker-Denschlag. Tuning the scattering length with an optically induced Feshbach resonance. *Phys. Rev. Lett.* 93, 123001, 2004.
- [Tho05a] S. T. Thompson, E. Hodby, and C. E. Wieman. Spontaneous dissociation of ^{85}Rb Feshbach molecules. *Phys. Rev. Lett.* 94, 020401, 2005.
- [Tho05b] S. T. Thompson, E. Hodby, and C. E. Wieman. Ultracold molecule production via a resonant oscillating magnetic field. *Phys. Rev. Lett.* 95, 190404, 2005.
- [Tie92] E. Tiesinga, A. J. Moerdijk, B. J. Verhaar, and H. T. C. Stoof. Conditions for Bose-Einstein condensation in magnetically trapped atomic cesium. *Phys. Rev. A* 46, R1167, 1992.
- [Tie93] E. Tiesinga, B. J. Verhaar, and H. T. C. Stoof. Threshold and resonance phenomena in ultracold ground-state collisions. *Phys. Rev. A* 47, 4114, 1993.
- [Tig99] B. V. Tiggelen. *Wave Diffusion in Complex Media 1998*. Kluwer, Dordrecht, 1999.
- [Tim99] E. Timmermans, P. Tommasini, M. Hussein, and A. Kerman. Feshbach resonances in atomic Bose-Einstein condensates. *Phys. Rep.* 315, 199, 1999.
- [Ton36] L. Tonks. The complete equation of state of one, two and three-dimensional gases of hard elastic spheres. *Phys. Rev.* 50, 955, 1936.
- [Tsa08] C.-C. Tsai and D. Heinzen. Personal communication, 2008.
- [vA98] F. A. van Abeelen, D. J. Heinzen, and B. J. Verhaar. Photoassociation as a probe of Feshbach resonances in cold-atom scattering. *Phys. Rev. A* 57, R4102, 1998.
- [vA99a] F. A. van Abeelen. *Interaction processes in cold gases of alkali atoms*. Ph.D. thesis, Technical University Eindhoven, 1999.
- [vA99b] F. A. van Abeelen and B. J. Verhaar. Time-dependent Feshbach resonance scattering and anomalous decay of a Na Bose-Einstein condensate. *Phys. Rev. Lett.* 83, 1550, 1999.
- [Ver94] B. J. Verhaar. Collisions of ultracold atoms: Theory and examples. *Laser Phys.* 4, 1050, 1994.
- [vK02] E. G. M. van Kempen, S. J. J. M. F. Kokkelmans, D. J. Heinzen, and B. J. Verhaar. Interisotope determination of ultracold rubidium interactions from three high-precision experiments. *Phys. Rev. Lett.* 88, 93201, 2002.
- [Vol03] T. Volz, S. Dürr, S. Ernst, A. Marte, and G. Rempe. Characterization of elastic scattering near a Feshbach resonance in ^{87}Rb . *Phys. Rev. A* 68, 010702, 2003.

- [Vol05] T. Volz, S. Dürr, N. Syassen, G. Rempe, E. van Kempen, and S. Kokkelmans. Feshbach spectroscopy of a shape resonance. *Phys. Rev. A* 72, 010704, 2005.
- [Vol06] T. Volz, N. Syassen, D. M. Bauer, E. Hansis, S. Dürr, and G. Rempe. Preparation of a quantum state with one molecule at each site of an optical lattice. *Nature Phys.* 2, 692, 2006.
- [Vol07] T. Volz. *Ultracold Rubidium Molecules*. Ph.D. thesis, Max-Planck-Institut für Quantenoptik, Garching, and Technische Universität München, 2007.
- [Wea90] R. L. Weaver. Anderson localization of ultrasound. *Wave Motion* 12, 129, 1990.
- [Wen04] X.-G. Wen. *Quantum Field Theory of Many-Body Systems*. Oxford University Press, Oxford, 2004.
- [Whi68] C. W. White, W. M. Hughes, G. S. Hayne, and H. G. Robinson. Determination of g -factor ratios for free ^{85}Rb and ^{87}Rb atoms. *Phys. Rev.* 174, 23, 1968.
- [Whi09] M. White, M. Pasienski, D. McKay, S. Q. Zhou, D. Ceperley, and B. DeMarco. Strongly interacting bosons in a disordered optical lattice. *Phys. Rev. Lett.* 102, 055301, 2009.
- [Wie97] D. S. Wiersma, P. Bartolini, A. Lagendijk, and R. Righini. Localization of light in a disordered medium. *Nature* 390, 671, 1997.
- [Wil82] F. Wilczek. Magnetic flux, angular momentum, and statistics. *Phys. Rev. Lett.* 48, 1144, 1982.
- [Xu03] K. Xu, T. Mukaiyama, J. R. Abo-Shaeer, J. K. Chin, D. E. Miller, and W. Ketterle. Formation of quantum-degenerate sodium molecules. *Phys. Rev. Lett.* 91, 210402, 2003.
- [Zap09] I. Zapata and F. Sols. Andreev reflection in bosonic condensates. *Phys. Rev. Lett.* 102, 180405, 2009.
- [Zha09] P. Zhang, P. Naidon, and M. Ueda. Independent control of scattering lengths in multicomponent quantum gases. *arXiv:0901.0694v3* 2009.
- [Zwi03] M. W. Zwierlein, C. A. Stan, C. H. Schunck, S. M. F. Raupach, S. Gupta, Z. Hadzibabic, and W. Ketterle. Observation of Bose-Einstein condensation of molecules. *Phys. Rev. Lett.* 91, 250401, 2003.
- [Zwi04] M. W. Zwierlein, C. A. Stan, C. H. Schunck, S. M. F. Raupach, A. J. Kerman, and W. Ketterle. Condensation of pairs of fermionic atoms near a Feshbach resonance. *Phys. Rev. Lett.* 92, 120403, 2004.
- [Zwi05] M. W. Zwierlein, J. R. Abo-Shaeer, A. Schirotzek, C. H. Schunck, and W. Ketterle. Vortices and superfluidity in a strongly interacting Fermi gas. *Nature* 435, 1047, 2005.

Danksagung

Zum Schluss gilt es, all denjenigen meinen Dank auszusprechen, ohne die ein Gelingen dieser Arbeit nicht möglich gewesen wäre.

An erster Stelle möchte ich hierbei meinen Doktorvater Prof. Gerhard Rempe nennen, der mir die Möglichkeit gab, in einer einzigartigen Umgebung die faszinierende Welt ultrakalter Quantengase zu erforschen. In ihm fand ich stets einen interessierten Gesprächspartner für fruchtbare Diskussionen. Besonders möchte ich mich auch für das Vertrauen bedanken, welches er mir entgegenbrachte.

Ebenso großer Dank gilt Stephan Dürr, dem senior scientist an unserem BEC-Experiment. Er verfügt über ein unglaubliches Repertoire an Fachwissen und stand immer zur Beantwortung von Fragen zur Verfügung. Er hat die Gabe, komplexe physikalische Zusammenhänge auf sehr pädagogische Art und mit anschaulichen Bildern zu erklären. Auch beeindruckte er durch sein atemberaubendes Tempo bei der Entwicklung theoretischer Modelle, welche oftmals mit den experimentellen Daten unserer Messungen im Labor „wie gelogen“ zusammenpaßten. Besonderer Dank gilt ihm zudem für das kritische Korrekturlesen der vorliegenden Arbeit und die hilfreichen Verbesserungsvorschläge.

Nicht weniger herzlich möchte ich mich bei meinen Doktorandenkollegen am BEC-Experiment Thomas Volz, Niels Syassen, Matthias Lettner und Chris Vo bedanken, mit denen die Zusammenarbeit stets produktiv, kurzweilig und fröhlich war. Thomas Volz, mein ehemaliger HiWi-Mentor, hat oft mit pfiffigen Ideen zum Betreten neuer physikalischer Gefilde beigetragen. Seine positive Art und seine Leidenschaft für schwedische Popgruppen der 1970er Jahre lockerten die eine oder andere heiße Meßphase im Labor auf. Niels beeindruckte stets mit seinen Programmierfähigkeiten, mit denen er schnell Software-Neuerungen in unsere Experimentsteuerung implementierte. Eine vormittägliche Bergtour mit anschließender, erfolgreicher Meßsession am selben Tag zeigt, wie effektiv und effizient man mit ihm arbeiten kann. Ganz besonderer Dank gilt auch Matthias, den ich durch einen glücklichen Zufall als meinen Nachfolger für unser Experiment und als einen sehr guten Freund gewinnen durfte. Die Zusammenarbeit mit ihm war derart positiv, dass selbst Vakuumprobleme, Klima(anlagen)katastrophen und Ausfälle technischer Gerätschaften jeglicher Art nicht in Frustration ausarteten. Mit Chris hat das Team einen überaus würdigen Neuzugang erhalten, der mit seinem Einsatz sicherlich zu weiteren interessanten Arbeiten beitragen wird. Sein auf einen Frequenzkamm stabilisierter „Karlson“ katapultierte einige unserer Messungen in Sphären hochpräziser Laserspektroskopie.

Herzlichen Dank auch an unsere Diplomanden Eberhard Hansis und Daniel Dietze. Eberhards Programm „Hermes“ ist bis heute fester Bestandteil und Grundstein unserer Experimentsteuerung und mit „Pan“ kann jedes Absorptionsbild schnell und benutzerfreundlich analysiert werden. Auch Daniel ist ein Schöngeist der Programmierkunst und generalisierte unsere Bildverarbeitungssoftware für eine Vielzahl unterschiedlicher Kamerasysteme. Seine Optimierung des Abbildungssystem ermöglicht einen „fringe“-freien Genuss eiskalter Atomwölkchen.

Ich bin stolz, Teil eines so hochkarätigen Teams gewesen zu sein und hoffe sehr, dass die enge Freundschaft zu all meinen BEC-Kollegen auch über diese Arbeit hinaus weiterbestehen wird!

Desweiteren möchte ich mich bei allen anderen Mitgliedern der Quantum Dynamics Gruppe für die freundschaftliche Atmosphäre und den intensiven Austausch von Wissen und Labormaterial jeglicher Art bedanken. Michael Motsch und Molekül-Urgestein Thomas Rieger gaben gute Tipps bei unseren „Vakuumaaktionen“. Holger Specht und dem QGate-Team, sowie Jörg Bochmann und dem Pistolero-Experiment sei gedankt für das Borgen von Laserlicht während der letzten Messungen dieser Arbeit.

Zahlreiche Interpretationen experimenteller Daten erarbeitete das BEC-Team in Zusammenarbeit mit theoretischen Physikern. Hier seien Tommaso Roscilde, Birger Horstmann, Juan-Jose García-Ripoll und Ignacio Cirac genannt. Tommaso und Birger versorgten uns mit theoretischen Vorhersagen und erhellenden Erklärungen zur „Lokalisierung“, während Juan-Jose zur Interpretation unserer „Zeno“-Daten beitrug. Ignacio überraschte oft mit geistreichen Ideen zur experimentellen Umsetzung im Labor.

Dank gilt auch der Hänsch-Gruppe, insbesondere Birgitta Bernhardt und Katharina Predehl, für die noble Möglichkeit zur Mitbenutzung des nobelen Frequenzkamms.

Viele größere und kleinere Realisierungen technischer Art profitierten von der Unterstützung unserer Techniker Helmuth Stehbeck, Franz Denk, Tom Wiesmeier und Sepp Bayerl. Auch unserer Sekretärin Odette Gori sei an dieser Stelle für ihre organisatorische Hilfe gedankt.

Bedanken möchte ich mich desweiteren bei unseren Werkstudenten Stephan Albert, Simon Baur, Florian Huber und Christoph Skrobol für deren Unterstützung im Labor.

Meinen ehemaligen Studiengefährten Marc Janoschek und Christoph Hinke danke ich für all die Jahre gemeinsamer Erlebnisse physikalischer und nicht-physikalischer Art. Aus gemeinsamen Diskussionen über Physik konnte ich immer wieder ganz neue Erkenntnisse gewinnen. Ich bin froh, zwei solch talentierte Physiker kennengelernt und sie als gute Freunde gewonnen zu haben.

Ich danke all meinen Freunden, bei denen ich durch Laborarbeit entleerte Energie-Akkus wieder aufladen konnte und die mich stets zur erfolgreichen Verwirklichung meiner wissenschaftlichen Arbeit angefeuert haben.

Einen ganz besonderen Dank möchte ich meinen Eltern für ihre finanzielle und moralische Unterstützung während meiner gesamten bisherigen Laufbahn aussprechen.

Zu guter letzt möchte ich Anna Christian danken, die viel Rücksicht in der Schlussphase meiner Promotion auf mich genommen und für den schönstmöglichen Ausgleich zu dieser Arbeit gesorgt hat.